The Dissertation Committee for Talha Ali Arshad Certifies that this is the approved version of the following dissertation:

Nanofabrication via Directed Assembly: A Computational Study of Dynamics, Design & Limits

Committee:

Roger T. Bonnecaze, Supervisor

Christopher J. Ellison

Venkat Ganesan

S.V. Sreenivasan

Carlton G. Willson

Nanofabrication via Directed Assembly:
A Computational Study of Dynamics, Design & Limits

by

Talha Ali Arshad, BA; ME

Dissertation

Presented to the Faculty of the Graduate School of

The University of Texas at Austin

in Partial Fulfillment

of the Requirements

for the Degree of

Doctor of Philosophy

The University of Texas at Austin

August 2016

In the name of God, the Most Beneficent, the Most Merciful

… Say: Are those who know equal to those who do not know? …

(The Qur'an 39:9)

"He who follows a path in the quest of knowledge, Allah will make his path easy, leading him to Paradise.[1-3] … The superiority of the scholar over the worshipper is like that of the full moon over the stars." [2,3]

Prophet Muhammad Peace Be Upon Him

(as reported by [1]Muslim, [2]Abu Dawud & [3]Tirmidhi)

Acknowledgements

I owe a debt of gratitude to many without the help of whom this work would not have been possible.

Roger has been a consummate mentor: a sounding board for ideas as well as a source of guidance. He ensured that research was my only concern. I learnt a great deal working with him and enjoyed doing so.

Prof. Ellison was a patient and resourceful collaborator. Prof. Willson allowed generous use of his lab and his students' expertise. Brainstorming sessions with Prof. Sreenivasan and Dr. Shrawan Singhal generated many ideas. Andrew Dick, Ryan Deschner and Kris Gleason were very helpful in the lab. Chae Bin Kim and Joshua Katzenstein provided excellent experimental fodder for my modeling ninja.

Whether it be debating age-old questions of philosophy and politics or discussing research, group mates past and present made the experience what it was. Akhilesh, Andrew, Ben, Lavanya, Mark, Meghali, Michael, Mohammed, Parag, Shruti, Soumik, Stephanie: thank you all.

I would be remiss not to acknowledge the assistance of department staff in navigating computer glitches and university bureaucracy.

Finally, I'd like to thank my family. I owe everything I am to my parents and am blessed with the best siblings one could hope for.

All truth and good emanates from God. Errors and omissions are mine.

Nanofabrication via Directed Assembly:
A Computational Study of Dynamics, Design & Limits

Talha Ali Arshad, PhD

The University of Texas at Austin, 2016

Supervisor: Roger T. Bonnecaze

Three early-stage techniques, for the fabrication of metallic nanostructures, creation of controlled topography in polymer films and precise deposition of nanowires are studied. Mathematical models and computational simulations clarify how interplay of multiple physical processes drives dynamics, provide a rational approach to selecting process parameters targeting specific structures efficiently and identify limits of throughput and resolution for each technique.

A topographically patterned membrane resting on a film of nanoparticles suspended in a solvent promotes non-uniform evaporation, driving convection which accumulates particles in regions where the template is thin. Left behind is a deposit of particles the dimensions of which can be controlled through template thickness and topography as well as film thickness and concentration. Particle distribution is shown to be a competition between convection and diffusion represented by the Peclet number. Analytical models yield predictive expressions for bounds within which deposit dimensions and drying time lie. Ambient evaporation is shown to drive convection strong enough to accumulate particles 10 nm in diameter. Features up to 1 μm high with 10 nm residual layers can be deposited in < 3 minutes, making this a promising approach for continuous, single-step deposition of metallic nanostructures on flexible substrates.

Selective exposure of a polystyrene film to UV radiation has been shown to result in non-uniform surface energy which drives convection on thermal annealing, forming topography. Film dynamics are shown to be a product of interplay between Marangoni convection, capillary dissipation and diffusion. At short times, secondary peaks form at double the pattern density of the mask, while at long times pattern periodicity follows the mask. Increased temperature, larger surface tension differentials and thick films result in faster dynamics and larger features.

Electric fields in conjunction with fluid flow can be used to position semi-conducting nanowires or nanotubes at precise locations on a substrate. Nanowires are captured successfully if they arrive within a region next to the substrate where dielectrophoresis dominates hydrodynamics. Successful assembly is predicated upon a favorable balance of hydrodynamics, dielectrophoresis and diffusion, represented by two dimensionless groups. Nanowires down to 20 nm in length can be assembled successfully.

Table of Contents

List of Tables

List of Figures

Chapter 1: Introduction

Nanotechnology has long been seen[1] to be potentially transformative in addressing many pressing technological challenges in applications ranging from energy to healthcare. Nanostructures of various kinds have been leveraged to demonstrate label-free biosensing with unprecedented sensitivity,[2, 3] gate-all-around transistors,[4] transparent and flexible electronics,[5] de-coupling of thickness and absorbance in photovoltaics,[6] partial invisibility surfaces[7] and self-cleaning coatings[8] to name a few. However, commercialization of many such devices is precluded by a lack of manufacturing processes that can fabricate the requisite nanostructures within constraints of precision, repeatability, throughput and economy.[9, 10] The building blocks (polymer, nanoparticles, carbon nanotubes and nanowires), resolution (10 nm – 100 μm) as well as other geometric constraints (residual layer thickness, feature aspect ratio), structural integrity (tolerance to grain boundaries) and acceptable process conditions (mild temperatures for flexible substrates, scarce contaminants for plasmonic devices) that viable processes must conform to range as widely[11] as applications that benefit from nanostructures. The research outlined herein is aimed at helping address this void between discovery and commercialization.

Fabrication has two distinct paradigms:[9, 12, 13] the top-down approach, wherein bulk material is fashioned into devices, affords precise shape control but is limited in the smallest structures it can fabricate. Conversely, the bottom-up approach encourages disparate particles and molecules to assemble into the desired structures; it is more naturally suited to ever-reducing dimensions but tends to result in imprecise shapes and the ordering process is often prohibitively slow for high-volume manufacturing. We

focus on hybrid methods[10] in which bottom-up ordering of nanoparticles, nanowires or a polymer film is guided by a substrate, mask or template pre-patterned top-down.

Three techniques, working with and targeting different building blocks and applications, are studied: 1) assembly of nanoparticles into structures driven by solvent evaporation, aimed at plasmonic devices 2) creating controlled topography in polymer films by exploiting photochemistry as a way to mediate surface energy, for various applications including LEDs 3) deposition of semiconducting nanowires and carbon nanotubes onto precise locations on a substrate via a combination of an alternating electric field and fluid flow, for photovoltaics and next-generation transistors. The three are akin in a number of important ways: they leverage directed self-assembly, fall within micro/nano- fluidics and are designed to be amenable to continuous, roll-to-roll processing and flexible substrates.

For each of these early-stage techniques, we aim to develop an understanding of how the various physical processes at play drive dynamics and mediate pattern formation. We will then leverage this knowledge to address the following questions: can we predict the structures resulting from a given set of experimental parameters, and conversely, deduce the necessary parameters to target a specific structure efficiently? What determines the limits of the technique in terms of resolution and throughput and how can these be improved?

Computational approaches, both continuum- (finite element and finite difference) and particle-scale (Brownian dynamics) as appropriate, along with mathematical analysis are used to achieve these goals. Predictions from these methods are benchmarked against experimental observations from collaborators or from published literature.

Chapters 2, 3-4 and 5 are dedicated to the three methods in the order listed above. Each chapter is composed of four major sections: (i) an introduction to the motivation

behind studying the technique and a brief review of relevant research (ii) a description of the model systems studied, equations describing its dynamics and the computational and analytical methods employed (iii) a presentation and discussion of results (iv) conclusions summarizing key takeaways. Nomenclature is unique to each project and a list is included at the end of each chapter. Chapter 5 summarizes both the key results of the research, considers its impact as well as shortcomings and identifies future directions.

Chapter 2: Templated Evaporative Lithography for High Throughput Fabrication of Nanopatterned Films †

INTRODUCTION

The ability to fabricate 2-D arrays of nanostructures and nanostructured particulate films finds growing application in a wide variety of areas including plasmonic devices[15, 16], high-density data storage,[17, 18] photonic crystals,[19, 20] metallized ceramic layers,[21] microchip reactors,[22] biosensors[23, 24] as well as masks in various forms of nanosphere lithography.[25, 26] Typically, substrates with topographical[27, 28] or chemical[29] patterns and/or external fields[30, 31] have been employed to guide particles, polymers, cells and even DNA into a desired configuration. Such processes are often specific to a certain building block, limited to a few monolayers and necessitate multiple processing steps. Many traditional techniques are unsuited to metallic nanostructures.

Evaporation-induced convection and dewetting-mediated pattern formation in suspension droplets[32-36] and films[37-43] has been the subject of several studies, and the prospect of using such an approach to deposit patterned particulate and polymeric films is garnering increasing attention[44-59] due to the significant advantages it engenders.[26, 60, 61] It is low-cost, materials general and applicable to both mono- and multilayered assemblies.

Harris *et al*[58] performed experiments in which a suspension of particles was allowed to evaporate under a mask with periodic holes. Their results demonstrated that convection induced by heterogeneous evaporation results in particle migration towards regions of relatively fast evaporation, depositing either isolated features or a continuous film with raised features under the mask holes. Two attributes render such an approach unsuitable to commercial nanofabrication: prohibitively long drying times and

† The research outlined in this chapter has been published previously. Analysis and simulations were performed by TAA with suggestions and guidance from RTB.[14]

imprecisely defined deposits. Pattern deposition took around two hours, and arbitrarily shaped mounds constituted the features.

In an attempt to address these issues, we consider a film of suspended nanoparticles on a substrate with its top surface in contact with a solvent-permeable membrane of periodically varying thickness (Figure 2.1). The membrane's topographic pattern imposes heterogeneity in evaporation rate, resulting in flow of the suspension from relatively slow to fast evaporation regions. The membrane-template rests on the suspension, descending at a speed corresponding to the average evaporation rate as the liquid evaporates. Particle distribution within the film evolves as they convect with the liquid and diffuse within it. This continues until any part of the nanoparticulate film dries (i.e. the local particle volume fraction corresponds to random close packing), at which point the membrane ceases to descend but is left in place until the entire suspension has dried. Left behind is a deposit of particles with regions of varying height whose dimensions are determined by the pattern of the membrane mask and the properties of the nanoparticulate film. Deposits composed of metal nanoparticles can then be sintered to create a stable nanostructured film on the substrate.

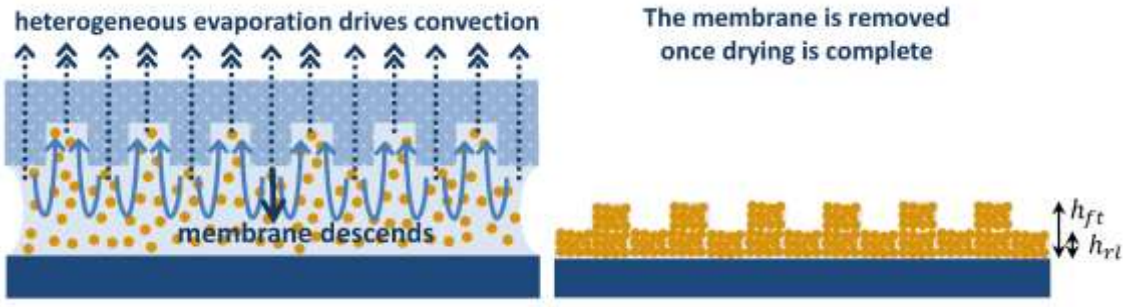

Figure 2.1 Schematic of templated evaporative lithography. Evaporation occurs more rapidly through the thinner regions of the solvent-permeable membrane, creating a convective flow which accumulates particles in those regions. The membrane descends at the average evaporation rate until it entraps close-packed or a monolayer of particles against the substrate. A deposit with residual layer and feature heights h_{rl} and h_{ft}

respectively is left behind once the entire suspension has dried.

Employing a solvent permeable template in this way is expected to reduce the time required for pattern deposition by allowing both a sweep gas to be employed to maximize the rate of evaporation. Via template topography, this arrangement also imparts greater precision to the deposit than free surface evaporation and allows more flexibility in deposit shape than template-free techniques;[44-46] for the topography shown in Figure 2.1, for example, rectangular stripes would be formed instead of mounds, and different template patterns can be used to define various 2D arrays.

The template can be positioned over the substrate down to a sub-20 nm resolution via the Moire alignment techniques used in imprint lithography.[62, 63] While a variety of methods exist for patterning membranes with features tens to hundreds of nanometers in size,[64-67] the task becomes increasingly challenging when both sub-micron thickness and large areas are desired. The former is important to ensure fast evaporation rates and the latter beneficial for large-area patterning in a single step. Thangawng and coworkers fabricated patterned PDMS membranes 500 nm thick and 700 μm in diameter.[68, 69]

The minimum thickness and maximum area of the membrane that can be achieved while maintaining the requisite mechanical stability for evaporative patterning are important questions left to future efforts. Instead, we focus on understanding the dynamics of the process to address fundamental issues that underpin its viability for high-volume manufacturing. Specifically, we investigate the following questions: Can such an arrangement reduce drying time to a commercially acceptable level? What is the lower limit on drying time if effective particle segregation is to be maintained? How do parameters such as the membrane thickness and topography as well as the initial height and concentration of the suspension film affect deposit size and drying time? How does

the fastest possible drying time vary with the desired feature size, and what is the optimal combination of parameters to achieve it?

In the following sections we first estimate the evaporation rate, present the equations describing particle dynamics as well as how they're solved numerically and carry out analysis to derive bounds on deposit dimensions as a function of experimental parameters. We then present solutions depicting suspension dynamics for representative cases, investigate how deposit dimensions and drying time vary with the independent variables, compare with the free surface evaporation experiments of Harris *et al.*[58] and identify performance limits in terms of shortest achievable drying time and minimum residual layer height for various feature sizes.

FORMULATION & ANALYSIS

Estimating the Evaporation Rate

The time for pattern deposition, critical to the viability of any technique as a practical industrial process, is governed in this case by the pervaporation rate of the liquid through the template. Neglecting evaporative cooling, the evaporation rate can be estimated from data for gas permeation in membranes (the liquid being equivalent to a gas at a partial pressure equal to the vapor pressure of the liquid):

$$J = P \times \frac{\Delta p}{d} \tag{4.1}$$

Here J is the evaporative flux, P the permeability of the membrane (usually expressed in Barriers ≡ 10^{-10} cm^3(STP).cm/(cm^2.s.cmHg)), Δp the partial pressure driving force and d the membrane thickness. Considering a toluene solvent at 20°C covered by a PDMS membrane with 33% silica:[70]

$$P = 9130\,\text{Barriers} = \frac{4.03}{10^{13}}\frac{m}{s}\frac{m}{cmHg}. \qquad (4.2)$$

The unit conversion is done so that (2.1) yields an evaporation rate in m/s (i.e. the rate of reduction of film thickness). When a sweep gas is used (so that partial pressure of solvent at the unpatterned face of the membrane is zero), this gives:

$$E = \frac{8.85\times10^{-13}}{d}\,\text{m/s} \qquad (4.3)$$

i.e. a 10 nm thick membrane results in an evaporation rate of 88.5 μm/s. This is comparable to pervaporation, wherein rates in excess of 100 μm/s have been reported.[71-73] Harris *et al*[58] reported free-surface drying rates of ≈ 0.014 μm/s for water. Hence the membrane, by its imposition of a steep chemical potential gradient, has a dramatic effect on drying time, dealing with an important barrier to industrial application of this bottom-up technique.

Equations Describing Particle Dynamics

The analysis is carried out in the context of a template with a step pattern as shown in Figure 2.1, and symmetry in the problem is exploited to restrict the domain of interest to one half period (Figure 2.2). Subscripts *s* and *f* refer to slow and fast evaporation regions, respectively, and Φ_0 to the initial particle volume fraction in the suspension. The evaporation rates are given by

$$E_f = \frac{8.85\times10^{-13}}{d_f}\,\text{m/s},\; E_s = \frac{8.85\times10^{-13}}{d_f + d_\Delta}\,\text{m/s} \qquad (2.4)$$

and the average evaporation rate

$$E_{av} = \frac{E_f L_f + E_s L_s}{L_f + L_s}, \tag{2.5}$$

which is also the speed of descent of the membrane.

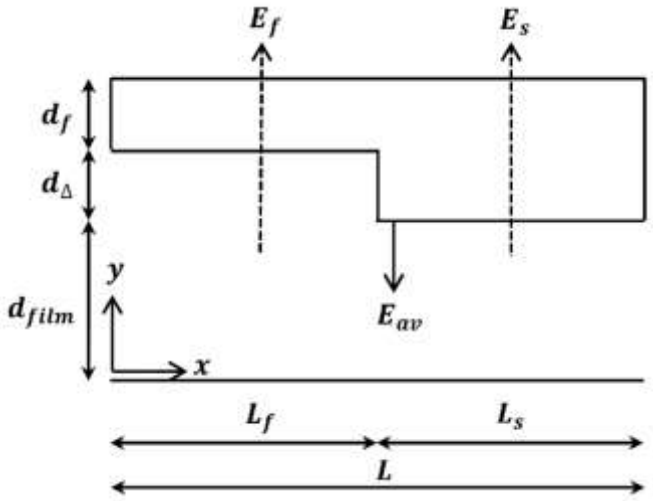

Figure 2.2 One-half wavelength of the periodically varying template and film of suspended nanoparticles.

Edge effects are ignored and the membrane is taken to be rigid. Scaling vertical distances by $d_\Delta + d_{film}$, horizontal distances by L, vertical velocities v by the average evaporation rate E_{av}, horizontal velocities u by $E_{av}L/(d_\Delta + d_{film})$ (from continuity) and time t by $(d_\Delta + d_{film})/E_{av}$, the dimensionless convection-diffusion equation for particle volume fraction Φ is given by

$$Pe\left(\frac{\partial \varphi}{\partial t} + u\frac{\partial \varphi}{\partial x} + v\frac{\partial \varphi}{\partial y}\right) = \frac{\partial}{\partial x}\left[D\frac{\partial \varphi}{\partial x}\right] + \frac{1}{A^2}\frac{\partial}{\partial y}\left[D\frac{\partial \varphi}{\partial y}\right] \tag{2.6}$$

where $Pe \equiv E_{av}L^2/D_0(d_\Delta + d_{film})$ is a Peclet number with D_0 and D being isolated sphere and suspension diffusivity, respectively. The Peclet number dictates the importance of

convection relative to diffusion in determining particle segregation between regions of fast and slow evaporation. $A \equiv (d_\Delta + d_{film})/L$ is an aspect ratio.

Fluid flow is described by momentum and material conservation, while diffusivity and viscosity are coupled to volume fraction through constitutive relationships. These, along with the appropriate boundary conditions, are described in the Appendix.

Fluid flow is described by momentum and material conservation. Ignoring gravitational effects and taking the fluid to be Newtonian, these are:

$$\mathrm{Re}\left(\frac{\partial u}{\partial t} + u\frac{\partial u}{\partial x} + v\frac{\partial u}{\partial y}\right) = -\frac{\partial p}{\partial x} + A\frac{\partial}{\partial x}\left[2\mu\frac{\partial u}{\partial x}\right] + \frac{1}{A}\frac{\partial}{\partial y}\left[\mu\frac{\partial u}{\partial y}\right] + A\frac{\partial}{\partial y}\left[\mu\frac{\partial v}{\partial x}\right] \qquad (2.7)$$

$$\mathrm{Re}\left(\frac{\partial v}{\partial t} + u\frac{\partial v}{\partial x} + v\frac{\partial v}{\partial y}\right) = -\frac{1}{A^2}\frac{\partial p}{\partial y} + \frac{1}{A}\frac{\partial}{\partial x}\left[\mu\frac{\partial u}{\partial y}\right] + A\frac{\partial}{\partial x}\left[\mu\frac{\partial v}{\partial x}\right] + \frac{1}{A}\frac{\partial}{\partial y}\left[2\mu\frac{\partial v}{\partial y}\right] \qquad (2.8)$$

$$\frac{\partial u}{\partial x} + \frac{\partial v}{\partial y} = 0 \qquad (2.9)$$

with the variables being in dimensionless form. Here pressure p, which includes the osmotic pressure, is scaled by $\mu_0 E_{av} L/(d_\Delta + d_{film})^2$ and the Reynolds number Re is defined as $\rho E_{av} L/\mu_0$.

Diffusivity and viscosity are coupled to volume fraction through constitutive relationships. Diffusivity D is given by the Stokes-Einstein equation:[74]

$$D(\varphi) = K(\varphi)\frac{d}{d\varphi}\left[\varphi Z(\varphi)\right] \qquad (2.10)$$

where K is the particle sedimentation coefficient and Z the compressibility factor, which account for hydrodynamic and thermodynamic interactions between particles

respectively. These, along with the dimensionless viscosity of the dispersion μ and the isolated sphere diffusivity D_0, are taken to be:[74]

$$K(\varphi) = (1-\varphi)^{6.55} \tag{2.11}$$

$$Z(\varphi) = \frac{1.85}{0.64-\varphi} \tag{2.12}$$

$$\mu = \left(1-\frac{\varphi}{0.64}\right)^{-2} \tag{2.13}$$

$$D_0 = \frac{k_B T}{3\pi\mu_0 a} \tag{2.14}$$

with particle diameter a, liquid viscosity μ_0, temperature T and Boltzmann constant k_B.

Evaluating the Numerical Solution

Boundary conditions for equation (2.6) are no penetration at all boundaries, which reduces to

$$\frac{1}{A^2 Pe} D\frac{\partial\varphi}{\partial y} - v\varphi = \varphi \tag{2.15}$$

at the horizontal faces of the membrane and

$$\mathbf{n}.\nabla\varphi = 0 \tag{2.16}$$

at all other boundaries, with **n** being a unit normal at the relevant boundary. For equations (2.7 – 2.9), symmetry boundary conditions prevail at the fluid boundaries of the domain. No slip is assumed at the vertical face of the membrane (as well as at the

substrate), while at its horizontal faces, the y-velocities are $E_s/E_{av} - 1$ and $E_f/E_{av} - 1$ in the slow and fast evaporation regions respectively. A Dirichlet point constraint for pressure was imposed at the top right corner of the slow evaporation region (Figure 2.2). Since flow is driven by the velocity boundary conditions at the template due to evaporation, it is valid to solve for net pressure without breaking it into its osmotic and fluid components.

The aforementioned system of equations was solved using COMSOL Multiphysics 3.5a. Membrane descent was modeled with the Automatic Lagrangian-Eulerian (ALE) mode with re-meshing enabled. A PARDISO direct solver was used in conjunction with BDF time stepping while all other settings were the COMSOL default values. Meshes with less than 10,000 quadratic Lagrange elements, with a boundary layer at the membrane when needed, were found to be sufficient for convergence.

Deriving Bounds on Deposit Dimensions Analytically

Diffusion-dominant and convection-dominant limits ($Pe \to 0$ and $Pe \to \infty$ respectively) constitute bounds within which the true particle concentration profile lies. The particle volume fractions averaged over the fast and slow evaporation regions ($\Phi_f(t)$, $\Phi_s(t)$) within these limits follow simply from material balances. These then yield limiting values for the feature and residual layer heights as well as drying time (t_d), the quantities of primary interest in the context of such a patterning process. This analysis is outlined below and the solutions summarized in Table 2.1.

Diffusive Limit (Pe→0)

In the infinite diffusion limit particle concentration is spatially uniform:

$$\varphi(t) = \left[\frac{\frac{d_\Delta}{d_{film}} + \left(1 + \frac{L_s}{L_f}\right)}{\frac{d_\Delta}{d_{film}} + \left(1 + \frac{L_s}{L_f}\right)\left(1 - \frac{E_{av}t}{d_{film}}\right)} \right] \varphi_0 \tag{2.17}$$

As evaporation proceeds, the membrane continues to descend until it comes into contact with either uniformly random close-packed particles or undried monolayers in the slow evaporation regions. In a given system, the former happens if $\varphi\left(t = \left(d_{film} - a\right)/E_{av}\right) \geq 0.64$ and the latter otherwise. We refer to the time at which the membrane ceases to descend as t_m and the total time it takes for the entire suspension to dry as the drying time t_d.

For systems in which uniform random close packing (RCP) is the operating regime, the drying time ($t_d = t_m$) follows simply by setting $\Phi(t)=0.64$ in (2.17). Deposit heights are then given by $h_{rl}=d_{film}-E_{av}t_m$ and $h_{ft}=h_{rl}+d_\Delta$. For a monolayer residual layer on the other hand, the drying time is the time it takes for the membrane to reach a point where it is one particle diameter away from the substrate plus the additional time for the fast evaporation region to dry, while the feature height is given by $h_{ft}=(d_\Delta+a)\Phi(t_m)/0.64$.

Convective Limit (Pe→∞)

Next consider a situation such that there is no diffusion of particles parallel to the substrate. In the slow evaporation region, the volume of liquid:

$$l_s = L_s\left(d_{film} - E_{av}t\right)\left(1 - \varphi_s\right), \tag{2.18}$$

$$\Rightarrow \frac{dl_s}{dt} = -L_s\left(d_{film} - E_{av}t\right)\frac{d\varphi_s}{dt} - L_s E_{av}\left(1-\varphi_s\right). \tag{2.19}$$

Incompressibility dictates that the rate of convection from the slow to the fast evaporation regions is $(E_{av} - E_s)L_s$. The rate of change of liquid volume in the slow evaporation region is therefore given by

$$\frac{dl_s}{dt} = -L_s\left[E_s + \left(1-\varphi_s\right)\left(E_{av} - E_s\right)\right] \tag{2.20}$$

Comparing equations (2.19) and (2.20) gives

$$\varphi_s(t) = \frac{\varphi_0}{\left(1-\frac{E_{av}t}{d_{film}}\right)^{E_s/E_{av}}} \tag{2.21}$$

The volume fraction of particles averaged over the fast evaporation region then follows from conservation of particles:

$$\varphi_f(t) = \left[\frac{\frac{d_\Delta}{d_{film}} + \left(1+\frac{L_s}{L_f}\right) - \frac{L_s}{L_f}\left(1-\frac{E_{av}t}{d_{film}}\right)^{1-E_s/E_{av}}}{\frac{d_\Delta}{d_{film}} + 1 - \frac{E_{av}t}{d_{film}}}\right]\varphi_0 \tag{2.22}$$

Equations (2.21) and (2.22) are valid as long as the membrane continues to descend. It ceases to descend when it comes into contact with random close packed particles in either the slow or the fast evaporation regions, or with undried monolayers in the slow evaporation regions. The operative regime within these three possibilities can be

inferred by using (2.21, 2.22) to determine whether either the slow or the fast evaporation regions attain random close packing before the membrane reaches a distance of one particle diameter from the substrate.

For systems in which the fast evaporation regions are the first to dry, the time at which the membrane stops descending (t_m) is given by setting $\Phi_f(t)=0.64$ in equation (2.22) and solving the resulting polynomial numerically. Deposit heights are then given by $h_{ft} = d_\Delta + d_{film} - E_{av}t_m$ and $h_{rl} = (d_{film} - E_{av}t_m)\Phi_s(t_m)/0.64$. When the slow evaporation regions dry first, t_m is simply obtainable by setting $\Phi_s(t_m) = 0.64$ in (2.21), while $h_{ft} = (d_\Delta + d_{film} - E_{av}t_m)\Phi_f(t_m)/0.64$ and $h_{rl} = d_{film} - E_{av}t_m$. Finally, when the monolayer h_{rl} regime is operative, the drying time is the time it takes for the membrane to reach a point where it is one particle diameter away from the substrate plus the additional time it takes for the fast evaporation regions to dry, and $h_{ft} = (d_\Delta + a)\Phi_f(t_m)/0.64$.

The results of the analysis are summarized in the Table 2.1, which should be used in conjunction with equations (2.17), (2.21) and (2.22) for $\Phi(t)$, $\Phi_s(t)$ and $\Phi_f(t)$ respectively to arrive at limiting values for the deposit heights and drying time. These serve as a heuristic to guide experiments targeting specific feature and residual layer dimensions and drying times.

Table 2.1: Analytically-derived bounds on deposit heights and drying time

	DIFFUSIVE LIMIT (*Pe*→0)	**CONVECTIVE LIMIT (*Pe*→∞)**
Regime Operative When:	**Monolayer h_{rl}** $\varphi\left(t=\dfrac{d_{film}-a}{E_{av}}\right)<0.64$	**Monolayer h_{rl}** $\varphi_f(t_m)<0.64 \quad and \quad \varphi_s(t_m)<0.64$
t_m	$(d_{film}-a)/E_{av}$	$(d_{film}-a)/E_{av}$
h_{ft}	$[\varphi(t_m)/0.64](d_\Delta+a)$	$[\varphi_f(t_m)/0.64](d_\Delta+a)$
h_{rl}	a	a
t_d	$t_m+\dfrac{1}{E_f}\left(1-\dfrac{\varphi(t_m)}{0.64}\right)(d_\Delta+a)$	$t_m+\dfrac{1}{E_f}\left(1-\dfrac{\varphi_f(t_m)}{0.64}\right)(d_\Delta+a)$
Regime Operative When:	**Uniform RCP** $\varphi\left(t=\dfrac{d_{film}-a}{E_{av}}\right)\geq 0.64$	**RCP in Fast Evap. Region** $\varphi_f(t\mid\varphi_s=0.64)>0.64 \quad and$ $t\mid(\varphi_f=0.64)<(d_{film}-a)/E_{av}$
t_m	t_d	given by polynomial eq. below*
h_{ft}	$h_{rl}+d_\Delta$	$d_\Delta+d_{film}-E_{av}t_m$
h_{rl}	$d_{film}\left(\dfrac{\varphi_0}{0.64}\right)-\dfrac{d_\Delta}{1+L_s/L_f}\left(1-\dfrac{\varphi_0}{0.64}\right)$	$\dfrac{\varphi_s(t_m)}{0.64}(d_{film}-E_{av}t_m)$
t_d	$\dfrac{1}{E_{av}}\left(d_{film}+\dfrac{d_\Delta}{1+L_s/L_f}\right)\left(1-\dfrac{\varphi_0}{0.64}\right)$	$t_m+\dfrac{1}{E_s}\left(1-\dfrac{\varphi_s(t_m)}{0.64}\right)(d_{film}-E_{av}t_m)$
Regime Operative When:		**RCP in Slow Evap. Region** $\varphi_f(t\mid\varphi_s=0.64)<0.64 \quad and$ $t\mid(\varphi_f=0.64)<(d_{film}-a)/E_{av}$
t_m		$\dfrac{d_{film}}{E_{av}}\left[1-\left(\dfrac{\varphi_0}{0.64}\right)^{E_{av}/E_s}\right]$
h_{ft}		$\dfrac{\varphi_f(t_m)}{0.64}\left[d_\Delta+d_{film}\left(\dfrac{\varphi_0}{0.64}\right)^{E_{av}/E_s}\right]$
h_{rl}		$d_{film}\left(\dfrac{\varphi_0}{0.64}\right)^{E_{av}/E_s}$
t_d		$t_m+\dfrac{1}{E_f}\left(1-\dfrac{\varphi_f(t_m)}{0.64}\right)\left[d_\Delta+d_{film}\left(\dfrac{\varphi_0}{0.64}\right)^{E_{av}/E_s}\right]$

* $\dfrac{L_s}{L_f}\left(1-\dfrac{E_{av}t_m}{d_{film}}\right)^{1-E_s/E_{av}}\left(\dfrac{\varphi_0}{0.64}\right)-\left(1+\dfrac{L_s}{L_f}\right)\dfrac{\varphi_0}{0.64}+\left(1-\dfrac{\varphi_0}{0.64}\right)\dfrac{d_\Delta}{d_{film}}-\dfrac{E_{av}t_m}{d_{film}}+1=0$

Independent Variables

Four independent variables allow us to affect the dimensions of the deposit and the drying time: two membrane thicknesses along with the initial thickness and concentration of the suspension film. Accessible ranges for these were taken to be 10 nm $\leq d_f \leq$ 1 mm, $0 \leq d_\Delta \leq 2d_f$, 100 nm $\leq d_{film} \leq$ 1 mm, $0.001 \leq \Phi_0 \leq 0.2$. Particle diameter a was set at 10 nm and ambient temperature (20°C) was assumed.

Table 2.2: Independent variables

Variable	Range
d_f	10 nm – 1 mm
d_Δ	0 – 2 d_f
d_{film}	100 nm – 1 mm
Φ_0	0.001 – 0.2

RESULTS & DISCUSSION

Dynamics for Representative Cases

Figure 2.3 shows simulation results for two different feature widths, giving different Peclet numbers. Heterogeneous evaporation induces flow from slow to fast evaporation regions, depicted by the streamlines. For 100 nm wide features, *Pe* is low; diffusion dominates and the suspension dries to uniform RCP throughout. For 1 μm wide features on the other hand, *Pe* is high ($Pe \propto L^2$); convection dominates, and instead of the entire suspension drying uniformly, the fast evaporation region attains RCP while the slow evaporation region is still fluid. The insets show the final size of the dried deposit; this is the same as shown in the numerical solution for $Pe = 0.27$, whereas at $Pe = 27$, the final deposit is realized once the *entire* suspension has dried. In the latter case, the deposit size is calculated assuming that once the fast evaporation region dries, membrane descent ceases and there is no further transfer of particles from the slow to the fast evaporation region.

It is noteworthy that the simulated deposit dimensions and drying times in these two cases correspond to the diffusive and convective limits respectively. These limiting cases are independent of the absolute feature width (they depend only on the relative width L_f/L_s). Narrow features tend towards the diffusive limit, whereas broad ones tend towards the convective.

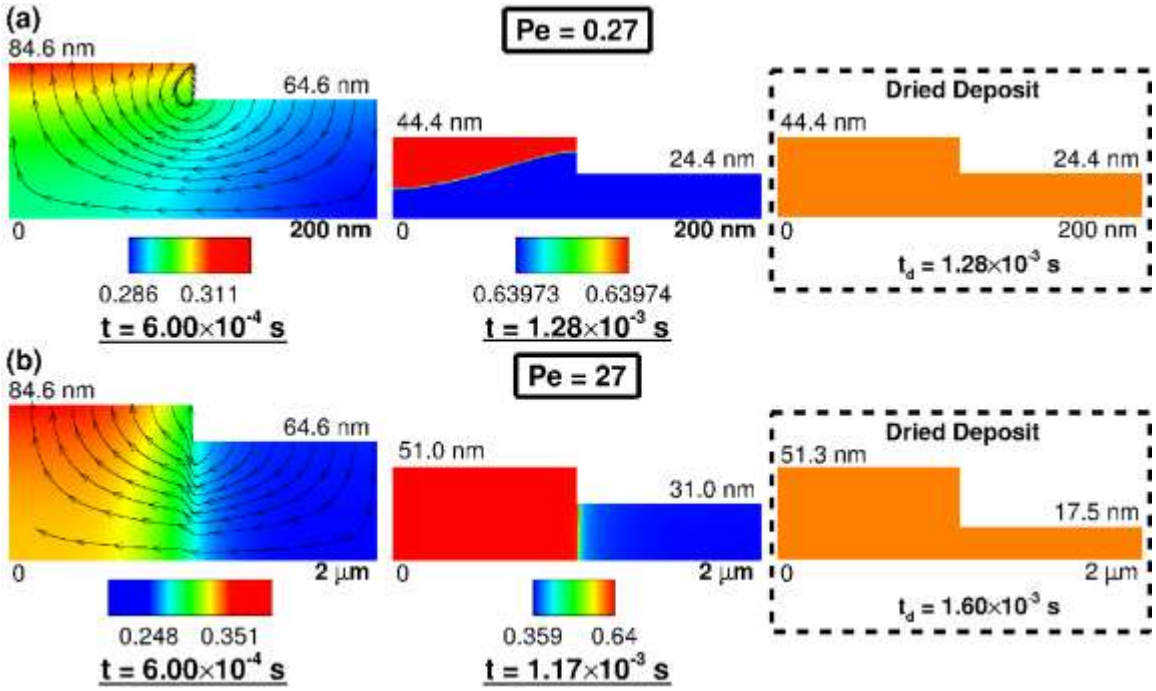

Figure 2.3 Evolution of particulate volume fraction contours and velocity streamlines for (a) 100 nm and (b) 1 μm wide features. The insets on the right show the final dimensions of the dried deposit in each case. The horizontal scale in (b) has been compressed. In both (a) and (b), $d_f = 10$ nm, $d_\Delta = 2d_f$, $d_{film} = 100$ nm, $\Phi_0 = 0.20$ and 10 nm particle diameter.

Effects of Independent Parameters

We now investigate the role played by each of the independent variables in determining the dimensions of the deposit and the drying time required to achieve it. The primary dependent process variables are the differential feature height (h_{ft}-h_{rl}), residual layer thickness (h_{rl}) and the drying time (t_d). Figure 2.4 shows how these quantities vary

with membrane thickness (d_f) and initial suspension film height (d_{film}) within the diffusive and convective limits, with $d_\Delta = 2d_f$. Note that increasing d_f has two opposing effects: it reduces *Pe*, thus hampering particle segregation by pushing the system towards the diffusive limit, but allows larger d_Δ, thus increasing the volume of the fast evaporation region and resultantly the height of the feature within the diffusive limit.

It is evident in Figure 2.4 that thick membranes result in more pronounced features as well as thinner residual layers at the cost of longer drying times. As d_f increases, so does the volume of the fast evaporation region (since $d_\Delta = 2d_f$), producing higher features. Thick suspension films produce higher features with longer drying times as well, but also thicker residual layers. This is expected, since at a constant initial volume fraction of particles, thick suspension films have more particles as well as more fluid that needs to evaporate.

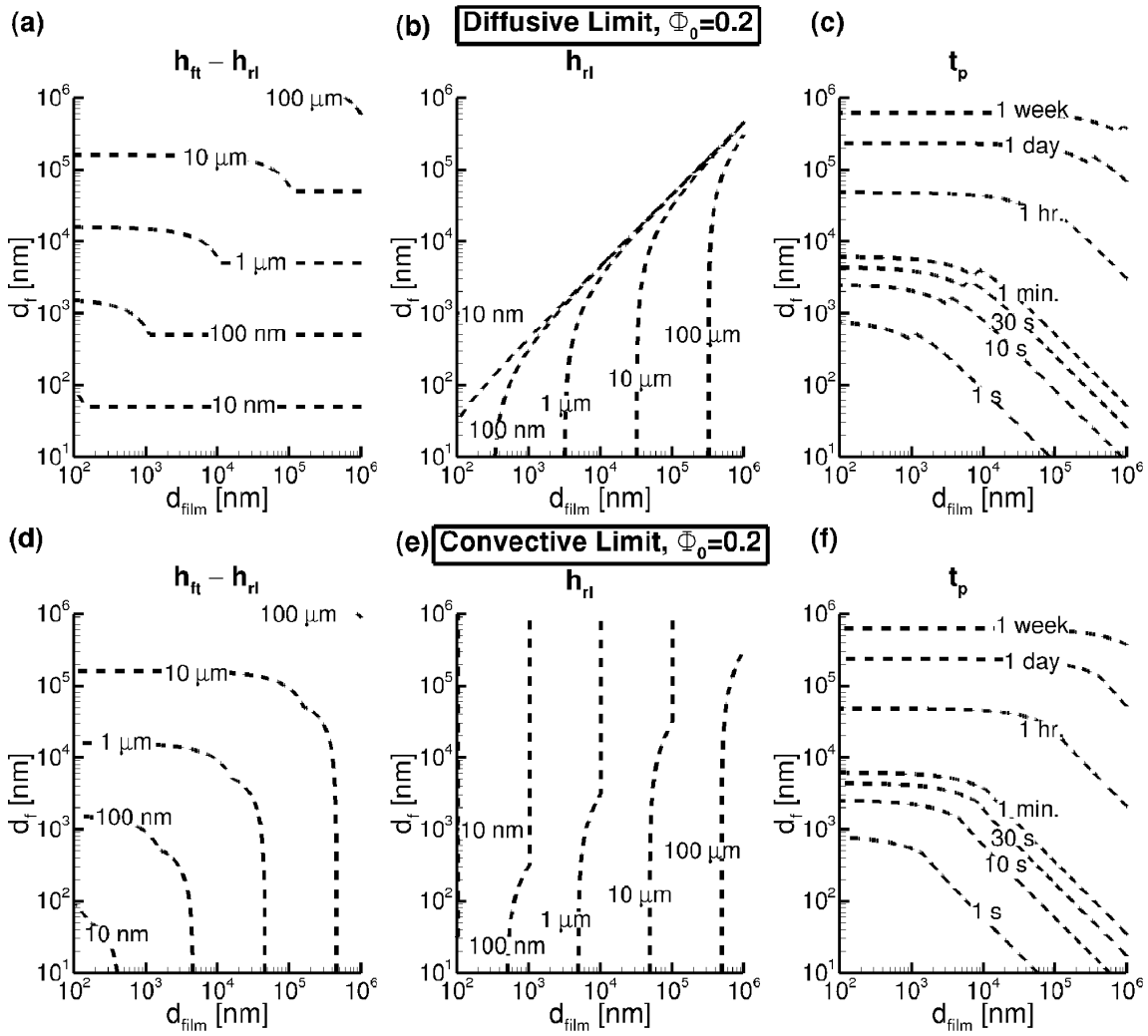

Figure 2.4 (a),(d) Differential feature height (b),(e) residual layer height and (c),(f) drying time as a function of film height and template thickness in the (a)-(c) diffusive and (d)-(f) convective limits, with $d_\Delta = 2d_f$, $\Phi_0 = 0.2$, $L_f/L_s = 1$ and 10 nm diameter particles.

Discontinuities in contour lines represent transition to a different operating regime, with two different regimes being operative in different regions of the parameter space. In the diffusive limit, undried monolayers impede membrane descent at high d_f and/or low d_{film} (top left of the plots in Figure 2.4(a-c)) due to the large difference in volume between the two regions. The residual layer height (Figure 2.4(b)) is therefore

one particle diameter, and the drying time (Figure 2.4(c)) is relatively insensitive to film height since the total volume of the suspension is determined mainly by d_f through d_Δ. At low d_f and/or high d_{film} (bottom right of the plots in Figure 2.4(a-c)), on the other hand, uniform RCP occurs when the membrane is more than one particle diameter away from the substrate. In this domain, the residual layer and feature heights increase equally with d_{film}, leaving the differential height (Figure 2.4(a)) unchanged. The drying time (Figure 4(c)) becomes a function of both d_f and d_{film}.

In the convective limit, the slow evaporation region dries first at high d_f and/or low d_{film} (top left of the plots in Figure 2.4(d-f)) due to its smaller volume. The height of the residual layer in this part of the parameter space is unaffected by d_f since the membrane-substrate distance at which the slow evaporation region attains RCP is insensitive to d_f,. The differential feature height and drying time do however depend on d_f. At low d_f and/or high d_{film} (bottom right of the plots in Figure 2.4(d-f)), the fast evaporation region dries first, and drying time as well as deposit heights vary with both d_f and $d_{film.}$

Thus, thick films drying under thick templates result in the most pronounced features but also long drying times. The diffusive and convective limits predict similar values for these quantities, except for the feature height for thick films dried under thin templates and the residual layer height for thin films dried under thick templates. Interestingly, in the latter case, the diffusive limit predicts a thinner residual layer than the convective. This is because in these cases particle concentration in the slow evaporation region within the convective limit increases at a faster rate than the fast evaporation region due to its much smaller volume. There exists a small region of the parameter space wherein residual layer height is very sensitive to suspension film and template thicknesses (Figure 2.4(b)), possibly leading to experimental uncertainty.

Differential feature heights of hundreds of nanometers can be achieved with a drying time of less than 30 s.

Figure 2.5 depicts results at a lower initial volume fraction of particles. The general trends in deposit dimensions with varying film height and template thickness remain largely unchanged but are shifted to smaller deposit sizes due to the presence of fewer particles. The operative regimes for dilute suspensions are the same as for relatively concentrated ones except that at high d_f and/or low d_{film} within the convective limit (top left of the plots in Figure 2.5(d-f)) undried monolayers instead of RCP in the slow evaporation region impede membrane descent. As a result, at a low initial concentration of particles (Figure 2.5(b,e)), there exists a large parameter space wherein a monolayered residual layer is predicted by both limiting cases. Such a region is barely extant at higher particle concentrations (Figure 2.4(b,e)). Low concentrations are therefore preferable if thin residual layers are of importance. This is relevant when isolated features are desired instead of contiguous films, in which case a film with a monolayered residual layer could be deposited and the residual layer possibly sonicated away prior to sintering.[75]

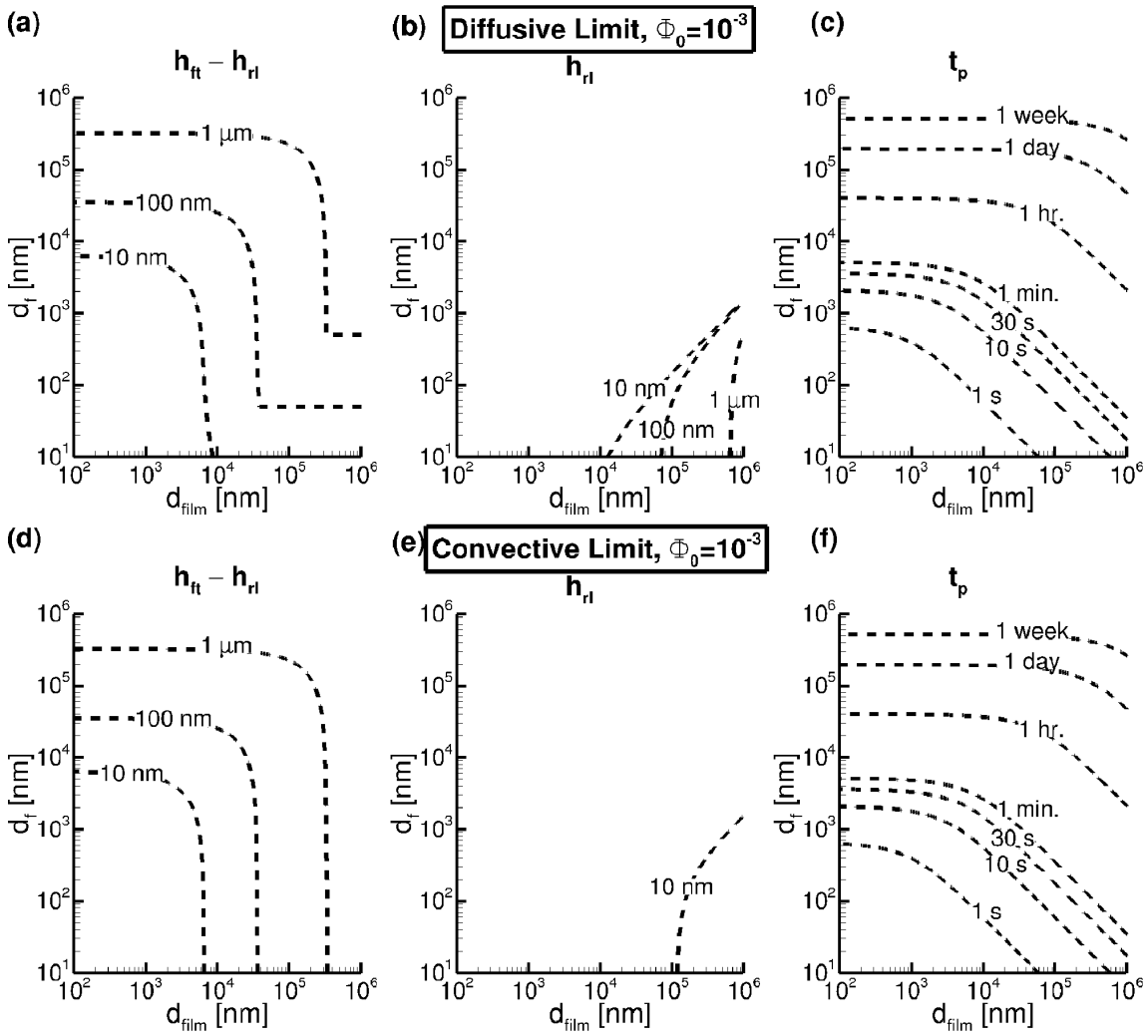

Figure 2.5 (a),(d) Differential feature height (b),(e) residual layer height and (c),(f) drying time as a function of film height and template thickness in the (a)-(c) diffusive and (d)-(f) convective limits, with $d_\Delta = 2d_f$, $\Phi_0 = 10^{-3}$, $L_f/L_s = 1$ and 10 nm diameter particles.

Two further controls on the process are temperature and particle size. Evaporation rate has been shown to increase exponentially with temperature,[76-78] while the rate of diffusion only increases linearly (see equation 2.14). As a result, the Peclet number is expected to increase with temperature, making more pronounced features patternable with faster drying times. Particle size sets the minimum residual layer height, and *Pe* is

proportional to it (through diffusivity). Therefore, the largest feasible particles for a mechanically stable deposit of the desired size are best used to maximize *Pe* for efficient particle segregation.

Comparison with Free-Surface Evaporative Lithography

Next we investigate how templated evaporative lithography compares with free surface evaporation[58] in depositing features of various widths. Figure 2.6 shows the differential feature heights resulting from a *micro*particle suspension within the two techniques, with the x-axis depicting how much the fast and slow evaporation rates differ. Only the convective limit is shown for templated evaporation since the Peclet number ranges from $4\times10^5 - 4\times10^8$ for this system. These curves do not extend to higher evaporation rate differences due to limits on membrane fabrication ($d_\Delta \leq 2d_f$). The drying times for the deposits shown are approximately 10 seconds for templated evaporative lithography and 2 hours for free surface evaporation. Therefore, templated evaporative lithography is able to produce features of half the size as free surface evaporation within a drying time which is two orders of magnitude smaller.

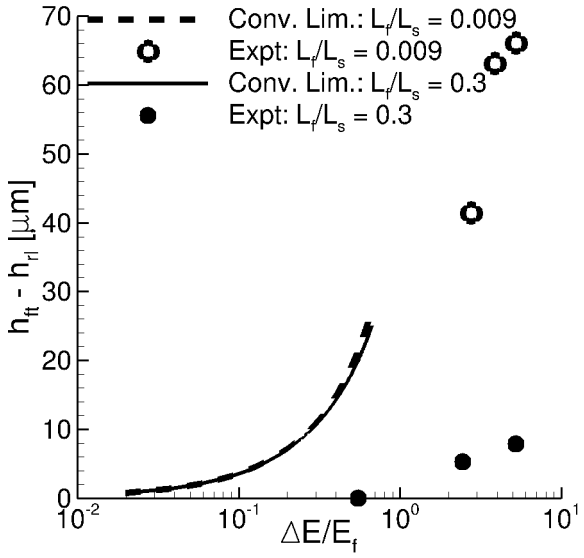

Figure 2.6 Differential feature height as a function of the dimensionless difference between the fast and slow evaporation rates at two different relative feature widths with a *micro*particle suspension. Shown is the relevant limit for templated evaporative lithography (lines; $d_f = 100$ nm and $d_\Delta = 0$ - $2d_f$) and experimental results reported[58] for free surface evaporation (points) with $d_{film} = 100$ μm, $\Phi_0 = 0.30$ and 1.18 μm diameter particles. The drying time is approximately 10 seconds for templated lithography and 2 hours for free surface evaporation.

In free surface evaporation, the difference between the two evaporation rates (and hence the attainable differential feature height) is a function of the width of features relative to the distance between them, with narrower features (L_f/L_s=0.009) being several times higher than broader ones (L_f/L_s=0.3). Moreover, the two evaporation rates, and hence also the feature and residual layer height, are coupled and cannot be controlled individually. In templated lithography, on the other hand, feature height can be seen in Figure 6 to be insensitive to relative feature width. Also, both evaporation rates can be controlled individually via membrane thicknesses (d_f and d_Δ), providing independent control over feature and residual layer height. When nanoscaled deposits are desired, the constraint which free surface evaporation imposes in terms of a maximum relative feature

width above which features are not formed is likely to be considerably more severe (and possibly even prohibitive) due to stronger diffusion.

Performance Limits

One further aspect of interest is the best performance, taken here to be defined by short drying times and thin residual layers, achievable within such a system and how it is influenced by desired feature size. In order to investigate this we approximate the differential height and drying time for any given system to be the average of their values within the diffusive and convective limits,‡ and optimize the independent variables to achieve the minimum drying time or residual layer height. Figure 2.7(a) shows the minimum attainable drying time and associated residual layer height for a range of differential feature heights. Both can be seen to increase linearly, and the minimum time is approximately 1 s per 10 μm of differential feature height:

$$\min. t_d \,[\mathrm{s}] \approx 1.3 \times 10^{-4} \times \left(h_{ft} - h_{rl} \right) [\mathrm{nm}] \tag{2.23}$$

$$h_{rl} \left(\min. t_d \right) \approx 2.4 \times \left(h_{ft} - h_{rl} \right) - 13 \tag{2.24}$$

These drying times represent the ideal limit, since they are dependent on 10 nm thick templates which are difficult to realize. Even with a more usual membrane thickness of 1 μm, however, the minimum time would be ten seconds per micron of feature height above the residual layer, which is acceptable for high throughput processing.

‡ As seen earlier, for certain systems differential feature heights predicted by the diffusive and convective limits differ by orders of magnitude, and so this serves only as a coarse estimate. However, this is mitigated by the fact that none of the estimated optimal systems lie within that region of the parameter space.

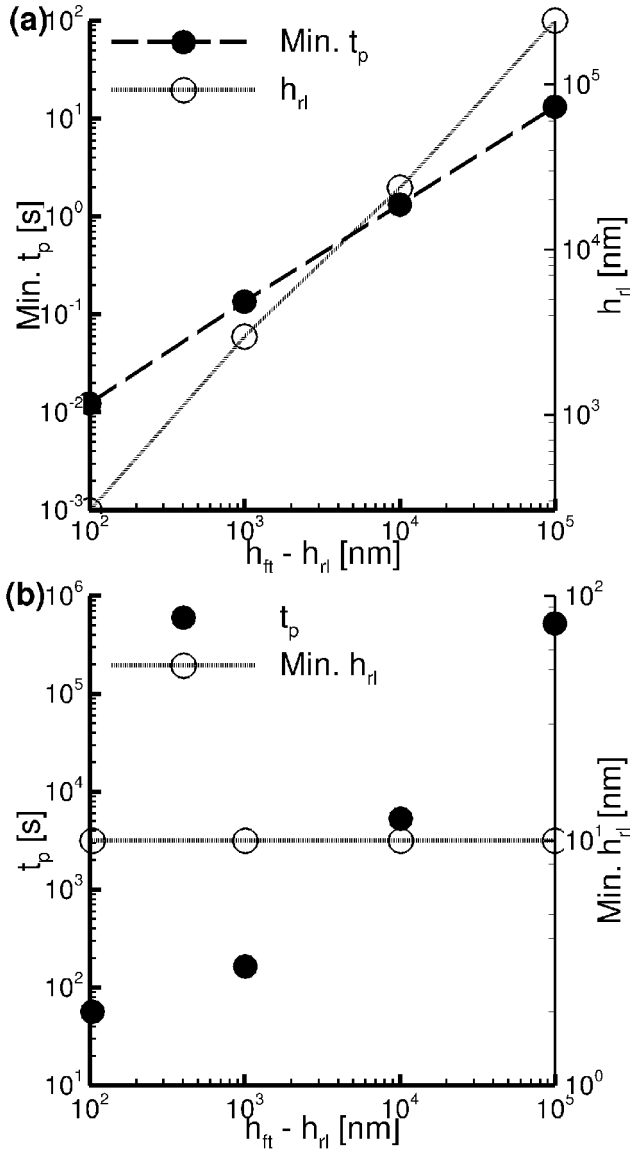

Figure 2.7 Minimum attainable drying time and resulting residual layer height (a) and minimum attainable residual layer height and resulting drying time (b) as a function of differential feature height, for deposits with $L_f/L_s = 1$ and 10 nm diameter particles (at $h_{ft} - h_{rl} = 10^2$, 10^3, 10^4, 10^5 nm, the values of the independent variables are: $d_f = 10$ nm, $d_\Delta = 12,12,20,18$ nm, $d_{film} = 1$, 11, 92, 940 μm, $\Phi_0 = 0.2$ in (a), while in (b), $d_f = 10$, 10, 50, 500 μm, $d_\Delta = 3.9$, 14, 100, 1000 μm, $d_{film} = 1$ μm, $\Phi_0 = 1.31\times10^{-2}$, 4.12×10^{-2}, 6.33×10^{-2}, 6.33×10^{-2}).

Another performance criterion is residual layer height, the lower limit on which is one particle diameter (as mentioned previously, this is especially relevant when isolated features are desired). Figure 2.7(b) depicts the minimum drying time for a range of feature heights with monolayered residual layers. It can be seen that the drying time increases at an accelerating rate with the desired feature height, and that it exceeds the minimum drying time (without the monolayer residual layer constraint) by as much as approximately four orders of magnitude in seconds. Isolated features up to a micron high, however, can be deposited within around 200 seconds. Interestingly, given enough time, even millimeter sized features are patternable with 10 nm diameter monolayered residual layers.

CONCLUSIONS

Spatially heterogeneous evaporation caused by a templated membrane drives an accumulation of particles in regions with fast evaporation, resulting in a deposit with raised features. Importantly, evaporation is rapid enough for continuous processing to be feasible, and nanosized deposits are achievable. Films with 10 nm−100 μm sized features can be patterned with a drying time of 1 - 100 seconds per 10 μm of differential feature height, depending upon the thickness of the membrane template. Experiments targeting specific deposits can be guided by analytically derived bounds on deposit dimensions and drying time (and optionally also by simulation). The analysis here shows that templated evaporative lithography presents potential improvement over free surface evaporation by making nanosized deposits attainable, reducing the drying time by two orders of magnitude, depositing sharply defined patterns and allowing independent control over each of their dimensions. Both the throughput and maximum area for deposition will be limited by the minimum thickness and maximum size of mechanically stable membranes.

Within these constraints, templated evaporative lithography constitutes a promising route for the low-cost deposition of three-dimensional metallic nanostructures of varying shapes over large areas in high-throughput processing.

NOMENCLATURE

Latin

a	particle diameter
d_f	template thickness in the fast evaporation region
d_{film}	initial thickness of the suspension film
d_Δ	difference between the two template thicknesses
h_{ft}	height of the resulting feature above the substrate
h_{rl}	height of the residual layer
k_B	Boltzmann constant
l_s	volume of solvent in the slow evaporation region
p	pressure (including both osmotic and fluid components)
t	time
t_d	the time it takes for the entire suspension to dry
t_m	the time it takes for the membrane to entrap either close-packed or a monolayer of particles against the substrate
A	aspect ratio
D	diffusivity of the suspension
D_0	diffusivity of an isolated particle
E	evaporation rate
E_{av}	average evaporation rate
E_f	evaporation rate in the fast evaporation regions
E_s	evaporation rate in the slow evaporation regions
J	evaporative flux
K	particle sedimentation coefficient
L	half-wavelength of template pattern
L_f	half-width of the fast evaporation region
L_s	half-width of the slow evaporation regions
P	permeability of the membrane
Z	particle compressibility factor

Greek

μ	viscosity of the suspension
μ_0	viscosity of the solvent
φ	volume fraction of particles
φ_f	volume fraction of particles in the fast evaporation region
φ_s	volume fraction of particles in the slow evaporation region

φ_0	initial volume fraction of particles in the suspension

Chapter 3: Precision Marangoni-Driven Patterning[§]

INTRODUCTION

Topographically patterned coatings and substrates can enhance surface properties and enable a wide variety of important applications. Polymer films possessing topographies that mimic the lotus leaf can act as super-hydrophobic and self-cleaning surfaces[80] while the highly anisotropic adhesion properties of gecko feet can be replicated by reproducing the structures on them.[81] Topographically patterned polymer surfaces are effective ways to resist biofouling[82] and direct cellular alignment.[83] Further, substrates and coatings with smoothly-varying thickness profiles have been employed to improve the efficiency of solar cells[84] and light-emitting diodes[85] by ~50% by passively manipulating light reflections within these devices. These applications would benefit from a process that can create well-defined topographic patterns on rigid and flexible substrates with various materials.

Gradients in surface energy are known to generate convection in liquid films,[86] manifesting themselves in numerous ways including the 'tears of wine' effect,[87] striation defects in spin-coating[88] and surface tension driven propulsion of floating objects.[89, 90] Surface tension is a material property and tends to decrease with increasing temperature; therefore both non-uniform concentration and temperature result in surface tension gradients.

Previous work[91] demonstrated that polymer photochemistry can be exploited to generate surface energy patterns. When such a film is heated above its glass transition temperature, these gradients drive convection resulting in the formation of topography. A schematic for topographical patterning of polymers in this way is shown in Figure 3.1.

[§] The research outlined in this chapter has been published previously.[79] Analysis and simulations were performed by TAA with suggestions and guidance from RTB; experiments were performed by CBK, NAP, JMK and DWJ with suggestions and guidance from CJE.

UV irradiation of a polystyrene (PS) film through a photo-mask selectively dehydrogenates the PS backbone and increases the local surface energy in the UV exposed regions compared to the unexposed regions. This was predicted by a group contribution method and confirmed by a decrease in water contact angle. As a result, the polymer flows from low surface tension regions (unexposed to light) to high surface tension regions (exposed to light) upon subsequent thermal annealing above the glass transition temperature (i.e., in the liquid state) due to the Marangoni effect. This flow creates smooth, three dimensional topography reflective of the original light exposure pattern.

While earlier experimental work demonstrates the viability of this approach to creating controllable topography, the processes driving film dynamics remain poorly understood. The effect of material selection and experimental parameters on film dynamics is unclear, as is how these may be selected to target specific structures efficiently. Here, we develop a model for the dynamics of the film leading to a predictive capability for the topography resulting from a given experiment.

In the sections below, we first outline equations describing film dynamics, the numerical technique used to solve them, scaling analysis identifying key dimensionless groups and an analytical solution based on linearization. We then compare simulation results for the evolution of topography with experimental observations of it, investigate the role played by various experimental parameters in determining the size of the resulting features as well as the timescale over which they form and consider how insight furnished by the model can help maximize the resolution accessible via this method. Details of experimental procedures can be found elsewhere.[79]

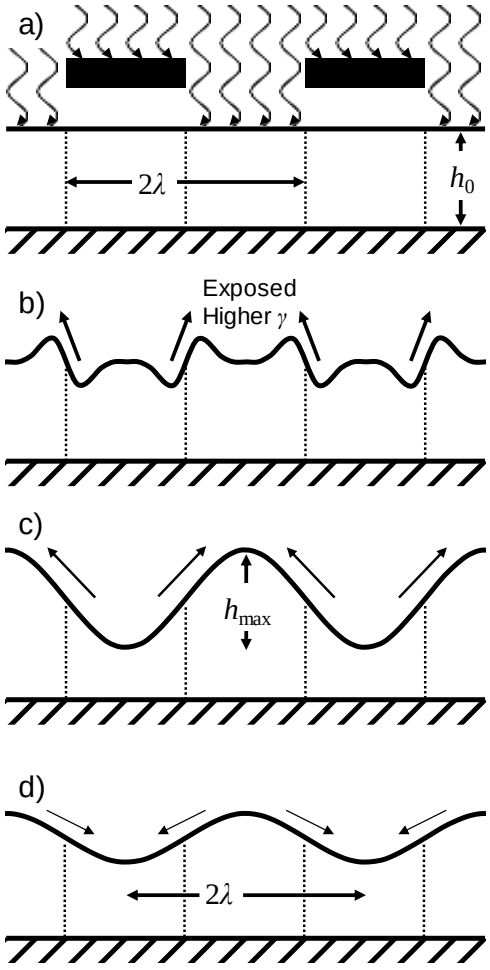

Figure 3.1 Patterning schematic. (a) UV illumination through a line-and-space photo-mask possessing a half-periodicity, λ, while the polymer film is in the solid state with an initial film thickness h_0. (b) The topographical profile after a short period of thermal annealing above the glass transition temperature of the polymer shows its melt-state flow is initiated near the boundary between UV exposed and unexposed regions. (c) Further annealing develops the topographical profile into a complete sinusoidal shape with the same periodicity as the mask reaching the maximum peak-to-valley height, h_{max}, then, (d) the topography dissipates after extended thermal annealing.

FORMULATION & ANALYSIS

Model

The dynamics of the film are driven by interplay of Marangoni (i.e. surface tension-generated) and capillary forces. The photochemically-induced surface tension gradient drives flow from relatively low to high surface tension regions. This is counteracted by capillary forces, which act to minimize surface area by maintaining a flat film. These dynamics are described by the thin film equation:

$$\frac{\partial h}{\partial t} + \frac{\partial}{\partial x}\left[\left(\frac{1}{2\mu}\right)h^2\frac{\partial \gamma}{\partial x} + \left(\frac{1}{3\mu}\right)h^3\frac{\partial}{\partial x}\left\{\gamma\frac{\partial^2 h}{\partial x^2}\right\}\right] = 0 \qquad (3.1)$$

where h is the thickness of the film at any given location, γ is local surface tension, μ viscosity, and x and t are the lateral distance and time, respectively.[92, 93] The first and second terms inside the square brackets account for Marangoni and capillary flux respectively. Van der Waals and gravitational forces are neglected since they only become relevant at length scales much smaller or larger than those of interest here. Since only thin films were used (the thickest being 148 nm), temperature gradients perpendicular to the substrate are taken to be negligible. The thin film equation is also predicated on the assumptions that (i) the lateral length-scale (represented by the mask linewidth λ) is much larger than the vertical one (the initial film thickness h_0) and (ii) $Re \times h_0/\lambda$, where Re is the Reynolds number, is small. For systems of interest here, the latter is easily met ($Re \sim 10^{-16}$), but the former imposes a lower limit on the characteristic width of the mask pattern. The equation is written in one spatial dimension since a mask with a line space pattern is employed which implies that the film is uniform parallel to the mask lines.

The local surface tension at any point is related to the concentration of the photochemically-generated species. As a first-order approximation, the surface tension of the blend is taken to vary linearly with concentration:

$$\gamma = \gamma_0 + (\Delta\gamma)c \tag{3.2}$$

where c is the mole fraction of the photochemical product, γ_0 is the surface tension of the original polymer and $\Delta\gamma$ is the difference in surface tensions between the original polymer and the polymer resulting from the photo-initiated reaction. $\Delta\gamma$ is defined to be positive when the photo-exposed polymer exceeds the base polymer in surface tension. Concentration is expressed in fractional (dimensionless) terms. The evolution of this concentration is described by:

$$\frac{\partial c}{\partial t} - \mathcal{D}\frac{\partial^2 c}{\partial x^2} + \frac{\partial}{\partial x}\left[\left(\frac{1}{\mu}\right)h\frac{\partial \gamma}{\partial x} + \left(\frac{1}{2\mu}\right)h^2\frac{\partial}{\partial x}\left\{\gamma\frac{\partial^2 h}{\partial x^2}\right\}\right]c = 0 \tag{3.3}$$

where $\mathcal{D}$ is the diffusivity. This is simply the convection-diffusion equation with fluid velocity being a sum of its Marangoni and capillary components (the first and second terms within the square brackets, respectively).[92, 93] Since the mask pattern is periodic, symmetry boundary conditions are applied at x = -λ and +λ, where the x = 0 is at the centerlines of the chrome lines on the mask under which the film is unexposed to light:

$$\frac{\partial h}{\partial x} = 0 \tag{3.4}$$

$$\frac{\partial p}{\partial x} = \frac{\partial}{\partial x}\left(-\gamma\frac{\partial^2 h}{\partial x^2}\right) = 0 \tag{3.5}$$

$$\frac{\partial c}{\partial x} = 0 \tag{3.6}$$

Initial Concentration Profile

Informed by fluorescence microscopy observations of fluorophore-labeled polystyrene films, a smoothed step function was used as the initial concentration profile. For on-half period of the mask pattern with peak conversion c_0, this is given by:

$$\frac{c}{c_0}\left(x/\lambda, t = 0\right) = 6\left(x/\lambda\right)^5 - 15\left(x/\lambda\right)^4 + 10\left(x/\lambda\right)^3 \tag{3.7}$$

The fluorescence intensity profile[79] as well as the initial concentration profile employed in simulations is shown in Figure 3.2. Since the labeled PS content was set below the threshold for self-quenching, this intensity is linearly proportional to the concentration of fluorophore.

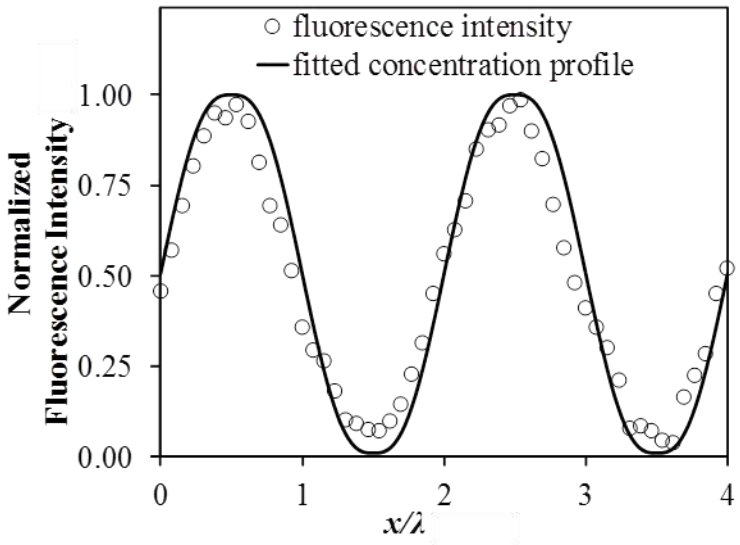

Figure 3.2 Normalized fluorescence intensity profile obtained experimentally from fluorescence microscopy using labeled PS after typical exposure protocol for patterning was performed. Solid line represents the initial concentration profile used in the model prediction.

Numerical Method

Equations (3.1, 3.3) with the aforementioned initial and boundary conditions were solved using a second-order finite difference method. A second-order scheme, with upwinding for the first the derivative of concentration in (3.3) for stabilization, along with explicit time-stepping are employed. 80 node points over a half periodicity of the mask pattern were found to be sufficient for convergence.

Scaling & Linearized Solution

The size of features resulting from a given experiment and the length of time over which the form are determined by the relative strength of Marangoni forcing and capillary dissipation, which itself depends upon a number of factors: geometry (pattern periodicity and film thickness), material properties (surface tension, diffusivity and viscosity) and experimental parameters (photochemical conversion and thermal annealing

temperature). To gain insight into these interrelationships, we non-dimensionalize the governing equations, employing the scales $x \sim \lambda$ (mask half-periodicity), $h \sim h_0$ (initial film thickness), $c \sim c_0$ (peak fractional conversion), $\gamma \sim \gamma_0$ (surface tension of the neat PS) and $t \sim \mu\lambda^2/h_0\gamma_0$. Rescaling equations (3.1 and 3.3) to make them dimensionless but retaining the same symbols for clarity gives the following:

$$\frac{\partial h}{\partial t} + \frac{\partial}{\partial x}\left[\left(\frac{1}{3A}\right)h^3\frac{\partial}{\partial x}\left\{\gamma\frac{\partial^2 h}{\partial x^2}\right\} + \left(\frac{1}{2}\right)h^2\frac{\partial \gamma}{\partial x}\right] = 0 \tag{3.8}$$

$$\frac{\partial c}{\partial t} = \left(\frac{1}{Pe}\right)\frac{\partial^2 c}{\partial x^2} - \frac{\partial}{\partial x}\left[c\left\{\left(\frac{1}{2A}\right)h^2\frac{\partial}{\partial x}\left\{\gamma\frac{\partial^2 h}{\partial x^2}\right\} + h\frac{\partial \gamma}{\partial x}\right\}\right] \tag{3.9}$$

where $A \equiv \lambda^2/{h_0}^2$ is the square of a geometric aspect ratio, and the Peclet number $Pe \equiv h_0\gamma_0/\mu D = (\lambda^2/D)/(\mu\lambda^2/h_0\gamma_0)$ is a ratio of the diffusive timescale to the convective timescale. The third relevant dimensionless group is $c_0\Delta\gamma$ which describes the initial surface tension difference between exposed and unexposed regions.

In order to develop analytic solutions leading to a predictive capability for feature size and time scale for feature formation for any given system, the governing equations are linearized. For small perturbations from their initial values, the film height and concentration profile are assumed to be have the forms

$$h = 1 + \eta(x,t) = 1 + \hat{\eta}(t)\frac{\cos(\pi x)}{2} \tag{3.10}$$

$$c = \frac{1}{2} + \xi(x,t) = \frac{1}{2} + \hat{\xi}(t)\frac{\cos(\pi x)}{2} \tag{3.11}$$

Here the initial concentration profile is taken to be sinusoidal: $c_{t=0} = 0.5(1 + \cos(\pi x))$. $\eta(x,t)$ and $\xi(x,t)$ represent the deviation in film thickness and concentration, respectively, from their steady state values, 1 and ½. $\hat{\eta}$ and $\hat{\xi}$ are the purely

time-dependent amplitudes of $\eta(x,t)$ and $\xi(x,t)$. Substituting these into the governing equations and neglecting higher order terms, the linearized equations are then

$$\frac{\partial \hat{\eta}}{\partial t} + \left[\left(\frac{1 + \Delta\gamma c_0 c_f}{3A}\right)\pi^4\right]\hat{\eta} - \left[\left(\frac{\Delta\gamma c_0}{2}\right)\pi^2\right]\hat{\xi} = 0 \tag{3.12}$$

$$\frac{\partial \hat{\xi}}{\partial t} + \left[\left(\frac{\left(1 + \Delta\gamma c_0 c_f\right)c_f}{2A}\right)\pi^4\right]\hat{\eta} - \left[\left(\Delta\gamma c_0 c_f - \frac{1}{Pe}\right)\pi^2\right]\hat{\xi} = 0 \tag{3.13}$$

with the initial conditions $\hat{\eta}(t=0) = 0$ and $\hat{\xi}(t=0) = 1$. These are solved to yield:

$$\hat{\eta} = \frac{\pi^2 \frac{\Delta\gamma c_0}{2}}{\psi_1 - \psi_2}(e^{\psi_1 t} - e^{\psi_2 t}) \tag{3.14}$$

$$\hat{\xi} = \left(\frac{\frac{\pi^4}{3A}(1 + \frac{\Delta\gamma c_0}{2}) + \psi_1}{\psi_1 - \psi_2}\right)e^{\psi_1 t} - \left(\frac{\frac{\pi^4}{3A}(1 + \frac{\Delta\gamma c_0}{2}) + \psi_2}{\psi_1 - \psi_2}\right)e^{\psi_2 t} \tag{3.15}$$

where

$$\psi_1, \psi_2 = \frac{\alpha \pm \sqrt{\alpha^2 - \beta}}{2} \tag{3.16}$$

with

$$\alpha = \left(1 - \frac{\pi^2}{3A}\right)\pi^2 \frac{\Delta\gamma c_0}{2} - \pi^2\left(\frac{1}{Pe} + \frac{\pi^2}{3A}\right) \tag{3.17}$$

$$\beta = \frac{\pi^6}{3A}\left(\frac{4}{Pe} - \frac{\Delta\gamma c_0}{2}\right)\left(1 + \frac{\Delta\gamma c_0}{2}\right) \tag{3.18}$$

These describe the evolution of the film thickness and concentration profiles. The imposed surface tension profile results in the formation and growth of features when the film is thermally annealed above its glass transition temperature, which eventually decays due to capillary forces and self-diffusion.[94] The maximum thickness attained and the thermal annealing periods after which it is achieved can be found from:

$$\hat{\eta}_{max} = \frac{\pi^2 \frac{\Delta\gamma c_0}{2}}{\psi_1 - \psi_2}\left\{\exp\left[\frac{\psi_1}{\psi_1 - \psi_2}\ln\left(\frac{\psi_2}{\psi_1}\right)\right] - \exp\left[\frac{\psi_2}{\psi_1 - \psi_2}\ln\left(\frac{\psi_2}{\psi_1}\right)\right]\right\} \quad (3.19)$$

$$t(\hat{\eta}_{max}) = \frac{\ln\left(\frac{\psi_2}{\psi_1}\right)}{\psi_1 - \psi_2} \quad (3.20)$$

Hence we arrive at analytical expressions for both the evolution of the film profile with time as well as the maximum feature size and associated time for any given choice of materials and experimental parameters. Equations 3.17 and 3.18 and the appropriate scaling factors can be used to find the dimensional maximum peak-to-valley height, $h_{max} = \hat{\eta}_{max} h_0$, and the heating time necessary to achieve it, $t_{max} = t(\hat{\eta}_{max}) \times \mu\lambda^2/h_0\gamma_0$. It should be noted that since higher order terms have been ignored, these expressions apply only to situations where the non-dimensional feature size and conversion are small. However, they serve as a useful tool to understand how the numerous independent variables and material properties affect film dynamics and the quantities of primary interest, namely the feature size and time scale.

Physical Property Values

Material property values used as input for model predictions are summarized in Table 3.1 at the temperatures considered. The viscosity, μ, of the PS blend as used was measured at 120^{o}C under steady shear. This viscosity was adjusted to lower values at

higher temperatures using free-volume parameters obtained from literature $\mu(T)$ data.[95] A handbook value[96] was used for γ_0, the surface tension of PS, and was subsequently adjusted for smaller molecular weights and higher temperatures.[97]

Table 3.1: Physical property values used in model predictions

Property	Value				Ref.
	120°C	126°C	136°C	140°C	
μ [Pa·s]	2550	1000	250	150	[79, 95]
γ_0 [dyne/cm]	32.2	31.7	31.1	30.8	[96, 97]
$\gamma_0\Delta\gamma$ [dyne/cm]	2.0	3.0	3.1	3.1	[79]
$\mathcal{D}$ [cm^2/s]	3.63×10^{-11}	2.15×10^{-10}	4.49×10^{-10}	5.91×10^{-10}	[79 98]

The difference in surface tension between PS and poly(phenyl acetylene) (PPA), $\gamma_0\Delta\gamma$, was extracted from the experimentally observed feature height evolution at short times. The linearized solution gives, for the peak to valley height in dimensionless form:

$$\hat{\eta} = \frac{\pi^2 \frac{\Delta\gamma c_0}{2}}{\psi_1 - \psi_2}(e^{\psi_1 t} - e^{\psi_2 t}) \tag{3.19}$$

Substituting in the Taylor series expansion for the exponential function and retaining terms only up to first order yields the evolution of peak-to-valley height at short times:

$$\hat{\eta} \approx \left(\pi^2 \frac{\Delta\gamma c_0}{2}\right) t \quad \forall \quad t \ll 1 \tag{3.20}$$

Comparing this to short-time experimental results, the difference in surface tension between the exposed and unexposed polymer ($\Delta\gamma$) can be extracted from the slope of the line.

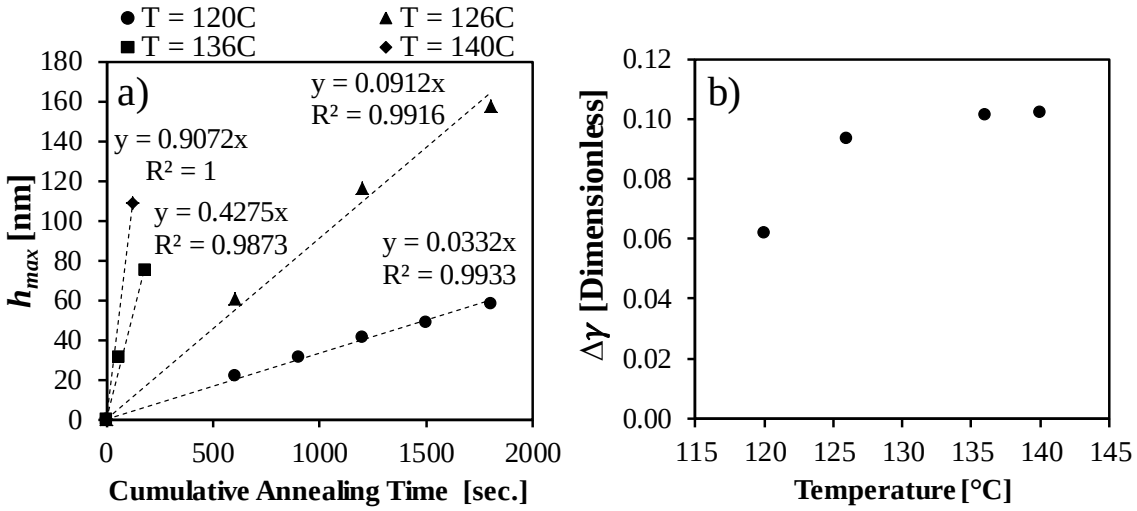

Figure 3.3 (a) Experimental results at short times (b) Non-dimensional surface tension difference values extracted from experimental data at four different temperatures.

While literature values for the surface energy of PPA are not available for comparison, it was previously estimated using a group contribution method that, the difference in surface tension between PS and PPA at 25°C, is 6.8 dyne/cm.[91] Furthermore, note that an equimolar copolymer of ethylene and propylene possesses a surface tension 1 dyne/cm lower than its partially dehydrogenated form, poly(isoprene), at 20°C.[96] The values of $\gamma_0\Delta\gamma$ in Table 3.1 are reasonable because they agree in magnitude, and lie between, these examples. At the photochemical conversion typically used for patterning (c_0 = 6.4 mol%[91]) the surface energy difference between exposed and unexposed regions ($c_0\gamma_0\Delta\gamma$) is at most 0.2 dyne/cm. $c_0\gamma_0\Delta\gamma$ does not appear to have a strong temperature dependence within the relatively narrow temperature range explored in this work.

The effective polymer blend diffusivity $\mathcal{D}$ was extracted from the feature height decay at 120°C observed at long experimental times. At long times, peak-to-valley height reduces to

$$\hat{\eta} \approx \frac{\pi^2 \frac{\Delta\gamma c_0}{2}}{|\psi_1 - \psi_2|} e^{\psi_{max} t} \quad \forall \quad t \gg 1 \tag{3.21}$$

where $\psi_{max} \equiv \max(\psi_1, \psi_2)$. This can be re-written as

$$ln(\hat{\eta}) \approx ln\left(\frac{\pi^2 \frac{\Delta\gamma c_0}{2}}{|\psi_1 - \psi_2|}\right) + (\psi_{max})t \tag{3.22}$$

Since the eigenvalues ψ_1 and ψ_2 are a function of diffusivity, it can be extracted by comparing this expression with experimental observations for peak-to-valley height at long times. As noted earlier, the linearized solution is valid for cases where the features are small compared to the thickness of the unperturbed film. This is always true at short times, but applies at long times only for low temperatures or small initial conversions. For this reason diffusivity was extracted using experimental results at 120°C and extrapolated to higher temperatures using correlations from literature (after shifting them to agree with the value at 120°C).

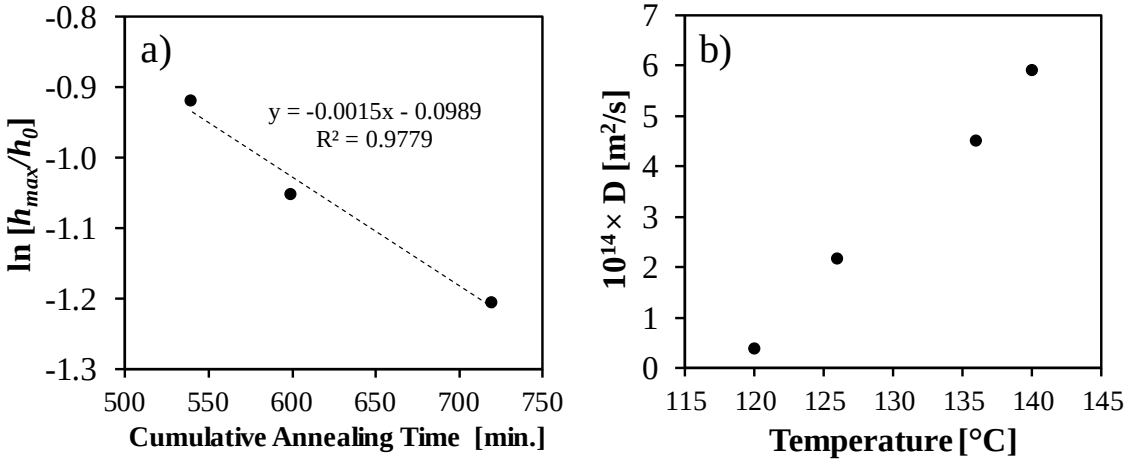

Figure 3.4 (a) Experimental results at 120°C for long times (b) Diffusivity values extracted from experimental data at 120°C and extrapolated to higher temperatures in accordance with correlations from literature.[99]

This value of $\mathcal{D}$ was adjusted to higher temperatures using an Arrhenius fit to bulk self-diffusion coefficient values measured by Fleischer[99] for PS with molecular weight M_W = 2.1 kg/mol and M_W = 4.0 kg/mol at temperatures between 160°C and 220°C to obtain the values in Table 3.1. Note that Ediger and coworkers[100] described $\mathcal{D}$ (T > 84°C) for a PS blend possessing Mw = 1.8 kg/mol and T_g = 59°C using a Williams-Landel-Ferry equation

$$\log_{10}\mathcal{D} = -14.48 + \frac{10.37\left(T - T_g - 16.6\ °\text{C}\right)}{56.11\ °\text{C} + \left(T - T_g - 16.6\ °\text{C}\right)}. \qquad (3.23)$$

The PS blend used had T_g = 61°C and M_W = 3.98 kg/mol, the latter of which is a factor 2.2 higher than that determined by Ediger and coworkers. A direct comparison can be made between their values of $\mathcal{D}$ and the ones in Table 3.1 by using T_g = 61°C in Equation 3.23 and dividing the $\mathcal{D}$ values it predicts by 2.2.[101] Since their values differ from mine by less than 50% at all 4 temperatures used in this work, the values of $\mathcal{D}$ used in model predictions are reasonable. These demonstrations imply, therefore, the

combined theoretical and experimental methodology would be a potential characterization method for very subtle surface energy changes and/or diffusion coefficients of complex polymer blends in confined thin films, using only inexpensive bench equipment and materials.

RESULTS & DISCUSSION

Evolution of Topographical Features After Heating Above T_g

Figure 3.5 includes both experimental results and model predictions for the film thickness profile after short and long thermal annealing periods. Each different stage of topography development as illustrated in Figure 3.1 is revealed by experiments and theory. It is evident that the (non-linear) model reproduces both the formation of secondary minima observed at short periods of thermal annealing and that of the complete sinusoidal features at the extended annealing periods.

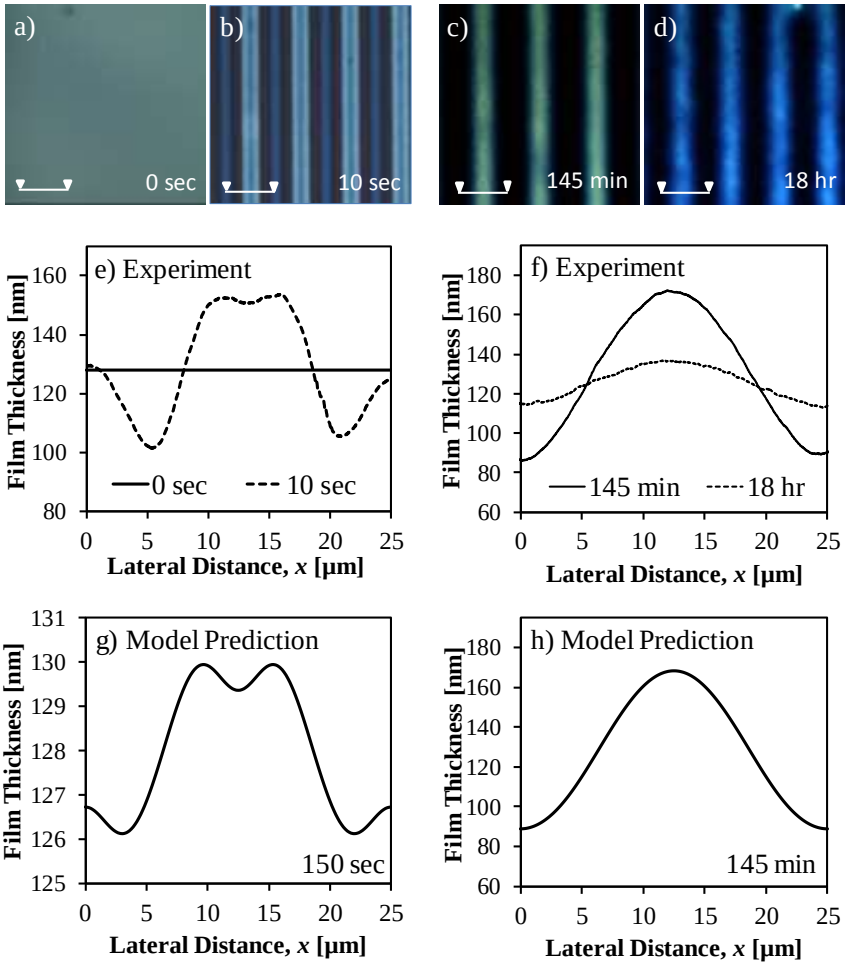

Figure 3.5 Representative 100 μm wide optical micrographs of one 128 nm thick PS film supported on a Si wafer after short (a,b) and long periods (c,d) of thermal annealing at120°C. Prior to the heating, the PS film was exposed to UV light through a 25 μm pitch photo-mask. Different colors observed in the optical micrograph are light interference patterns resulting from the film thickness variations. Experimentally characterized height profiles for one periodicity from the same polymer film are shown in (e) and (f) after short and long periods of heating, respectively. Two different film thickness profiles were also theoretically predicted for a 128 nm thick film and are shown in (g) and (h) respectively.

Both theory and experiment reveal that the appearance of secondary peaks at short thermal annealing times is related to the shape of the initial surface tension profile. Intuitively, one expects polymer transport to occur first at the interface between exposed and unexposed regions before it can reach the regions relatively far from that interface.

This concept is verified by noting that Equation (3.1) shows that the Marangoni flux is proportional to the second derivative of surface tension. At very short times, the film is essentially flat and capillary dissipation is negligible, resulting in maximum accumulation (and depletion) at points where the second derivative of surface tension has its largest magnitude. At intermediate and long times, on the other hand, when capillary forces are also relevant, maxima and minima in film height coincide with the maxima and minima of the concentration profile at the centerlines of mask quartz spaces and chrome lines, respectively. When the points of maximum magnitude of the second derivative of the initial surface tension profile do not coincide with the centerlines of the mask lines and gaps, secondary peaks form at short times. As long as the surface tension profile is present, these peaks always form; however, they may be short-lived in many cases. This finding is practically relevant because it represents a strategy, rooted in the physical nature of fluids, to double the areal density of topographic features from that present in the projected photo-mask pattern.

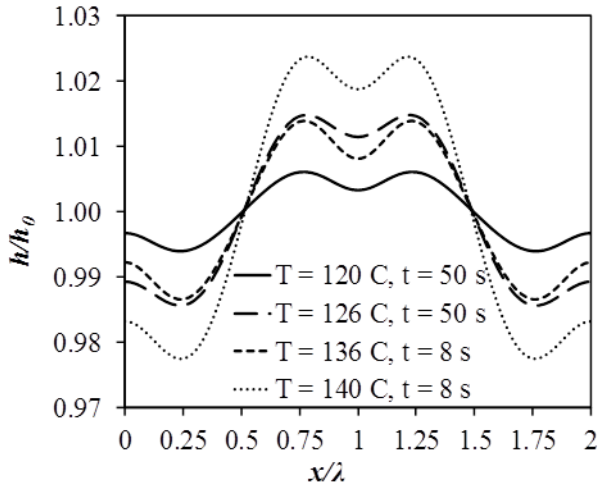

Figure 3.6 Simulated film height profiles at short times clearly depict secondary peaks at four different annealing temperatures. Thicknesses of the film in ascending order of temperature are 145, 148, 130 and 148 nm.

It is also apt to note that the three distinct regimes of film topography evolution once heated above its glass transition temperature are strongly connected to the structure of the theoretical model. At very short times, secondary peaks form at points where the second derivative of the initial surface tension profile has its largest magnitude. At intermediate times, features rise as Marangoni flux dominates over capillary dissipation. The Marangoni driving force decays with time as polymer self-diffusion makes the concentration profile, and as a result the surface tension profile, increasingly uniform. On the other hand, capillary dissipation intensifies as features grow. Eventually capillary forces dominate; features begin to decay and the film tends towards its original flat form.

Quantitative Comparison of Model to Experimental Data

Figure 3.7 depicts both the experimentally-observed and model-predicted evolution of peak-to-valley height $\hat{\eta}h_0$ as a function of cumulative annealing time at four different temperatures. Reasonable agreement between model predictions and experimental results are achieved for three of the four temperatures. The theoretical

model quantitatively predicts both the height of features as well as the timescale associated with their growth and decay. The quality of agreement obtained at the two highest temperatures is especially encouraging since those model predictions were made with only one parameter $c_0\Delta\gamma$ that was gleaned from the data itself. Unfortunately, as evident in Figure 3.8, the highest $\hat{\eta}h_0$ values measured at 126^{o}C are exceptionally large relative to the two neighboring datasets, and the model predictions do not closely match them.

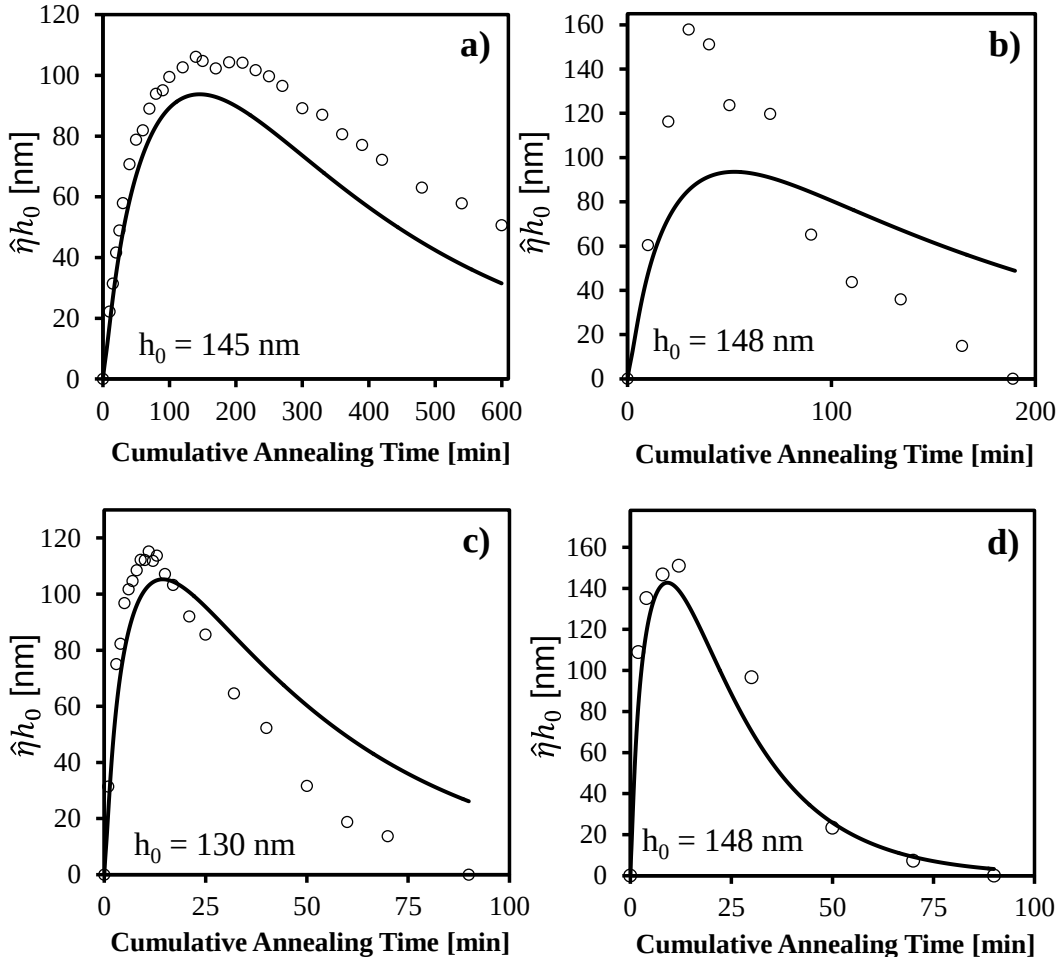

Figure 3.7 Comparison of peak-to-valley height evolution between experimental results (opened circle) and model predictions (solid line) at (a) 120°C, (b) 126°C, (c) 136°C, and (d) 140°C for PS films on glass.

Raising temperature reduces the viscosity of the film and increases its diffusivity. The former promotes the formation of larger features and more rapidly, while the latter hastens the onset of decay. Any change in the patterned surface tension gradient with temperature would also affect the process. Results show that overall, higher temperatures make larger features accessible while reducing the time needed to form them. Again, only the experimental data point for h_{max} collected at 126^{o}C lies outside this general trend. A 20 °C rise in temperature increases feature height by 50% while reducing the heating time

eleven-fold. Higher temperatures, within material constraints, are therefore preferable as long as the films are stable.

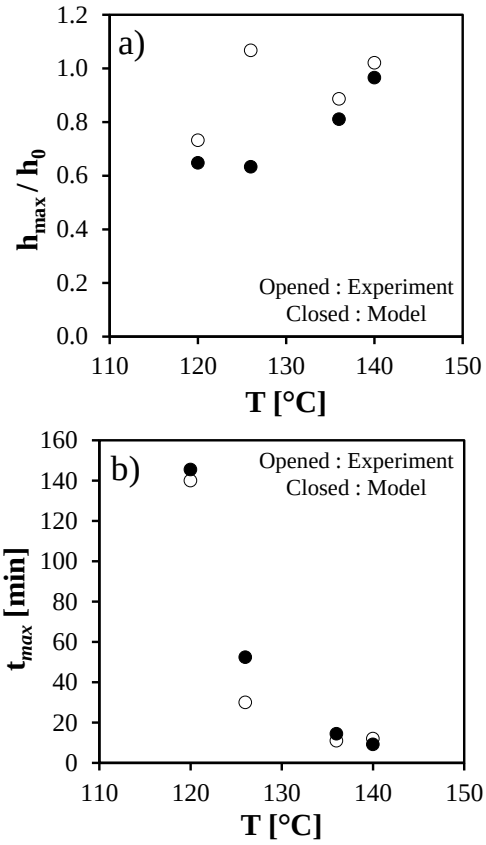

Figure 3.8 (a) Attainable maximum feature size and (b) associated thermal annealing time as a function of temperature.

Model Predictions of Marangoni-Driven Flow at Various Conditions

In the context of a patterning process targeting a specific feature size, it is prudent to engineer a process wherein the maximum height attained by features coincides with the target feature height. This ensures that the desired pattern is achieved in the most efficient way possible and is an important goal to enable rapid processing methods, such as roll-to-roll processing. Therefore, key variables for the application of this technique for various purposes are the maximum feature height attained and the heating time needed to

achieve it. In order to be able to design a process targeting a specific feature size with the desired resolution for a given application in the shortest possible heating time, an understanding of the limits of the process and the effects of each process variable on the two key quantities is necessary.

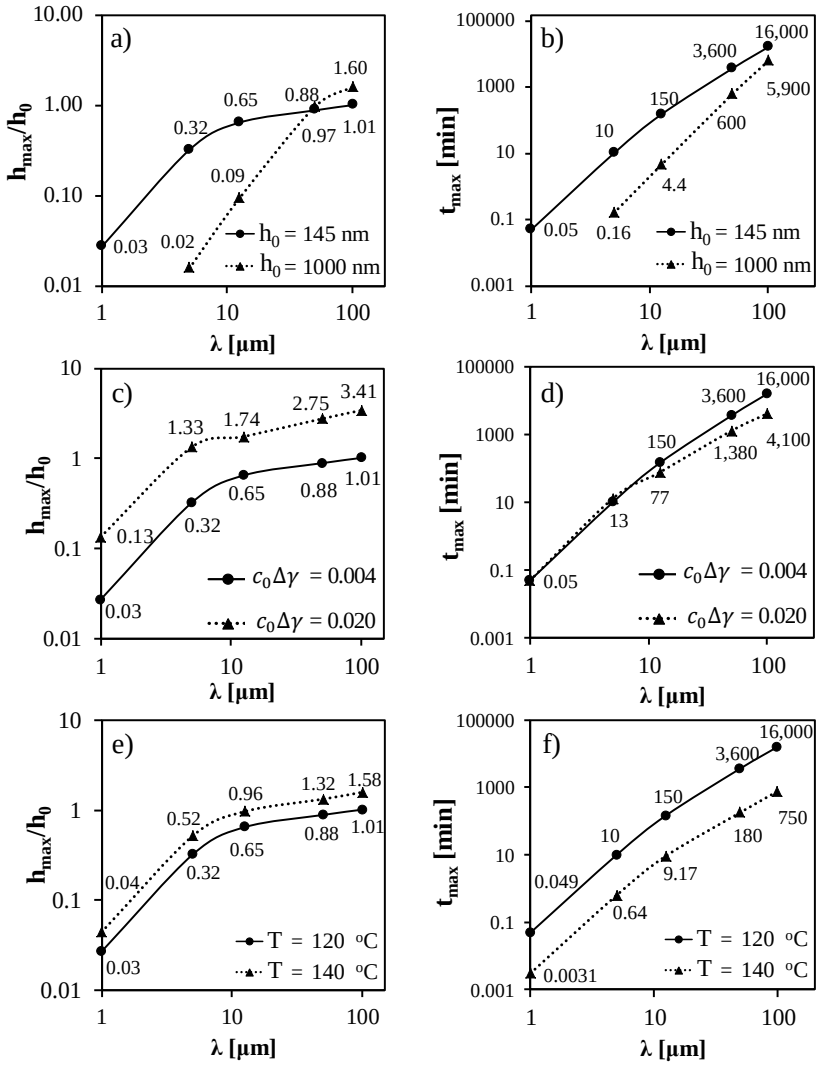

Figure 3.9 Normalized maximum peak-to-valley height h_{max}/h_0, and heating time as a function of resolution (photo-mask half-periodicity) for different film thicknesses (a, b), surface tension differentials (c, d), and heating temperatures (e, f). Data points represent model predictions and lines are guides to the eye. All case studies are otherwise at identical conditions as a base condition with h_0 = 145 nm, $c_0\Delta\gamma$ = 0.004, and/or T = 120°C

Figure 3.9 shows how absolute feature height and thermal processing time vary as a function of the desired pattern periodicity, and how experimental parameters, namely film thickness, the initial surface tension differential and annealing temperature affect this

relationship. An increase in pattern periodicity results in an enhancement in the accessible feature height but delays the achievable throughput time-scale. This is due to the fact that features farther apart can draw material from a larger region of low surface tension polymer. This effect was also seen in the evaporative self-assembly of particles[14, 58] in Chapter 2 where reduced pitch results in smaller features. As seen in Figure 3.9, this feature height penalty worsens with decreasing periodicity whereas promotion in throughput is approximately linear on this log-log plot.

The feature height in normalized terms (i.e. relative to the initial film thickness) is larger for thinner films. However, the absolute height of the features above the residual layer is larger for thicker films. This means that in applications tolerant to thick residual layers, greater variations in film thickness can be achieved by using thicker films. On the other hand, for applications in which the residual layer thickness between the feature minima and substrate surface needs to be minimized, thinner films are preferable. The data in Figure 3.9a predict that for the thinner film h_0 = 145 nm the highest possible aspect ratio of features, $½h_{max}\lambda^{-1}$, is achieved for a mask with a periodicity between 10 and 25 μm. However, for the thicker film h_0 = 1000 nm the maximum achievable aspect ratio can be made with a mask possessing a periodicity between 100 and 200 μm.

The initial surface tension differential is set by conversion which can be controlled through exposure dosage. A larger dosage increases the surface tension differential and results in significantly larger features. The heating time necessary to reach the maximum feature height is not strongly affected by the surface tension difference. Figure 3.9 (c, d) predicts that maximizing the surface tension difference is the most effective way to fabricate films with the greatest variations in film thickness.

As noted above, higher temperature promotes the formation of larger features at faster rates. Figure 3.9 (e, f) shows that while the increase in feature height resulting from

a 20 degree rise in temperature to 140°C is relatively modest (~50%), the necessary thermal processing time shortens by over an order of magnitude.

These results for varying temperature also suggest the role the molecular weight of the polymer plays in determining feature size and heating time. Temperature affects the dynamics of the film through variation in viscosity and diffusivity. According to the Rouse model for unentangled polymer melts, the product of diffusivity and viscosity is directly proportional to temperature and inversely proportional to molecular weight.[101] Reduced molecular weight would therefore exert an effect on feature height and throughput time-scale as a function of pattern periodicity similar to that of increased temperature. The relatively modest rise in feature height with increased temperature is due to the fact that the viscosity of the polymer melt and the diffusivity of the photo-exposed polymers are coupled, as predicted by the Rouse model. With increasing temperature, a sharp decline in viscosity, which should promote the formation of larger features more rapidly, is accompanied by an increase in the polymers' self-diffusion, resulting in a more rapid dissipation of the surface tension gradient. This suggests that a polymer blend comprising of a small amount of a large molecular weight photoactive polymer within a bulk low molecular weight polymer would simultaneously minimize diffusivity and maximize viscosity, resulting in the largest possible features even at high resolutions.

CONCLUSIONS

Here a model was introduced which accurately describes topography formation in thin polymer films which possess surface energy patterns. All of the stages of topography development (see Figure 3.2) are qualitatively predicted by a relatively simple, computationally efficient adaptation of the film equation. Strictly speaking, if a polymer

film possesses a surface energy pattern, even one in which the variations are only 0.2 dyne/cm, Marangoni flow will result when it is heated above its glass transition. Only the size and longevity of the topographical features varies with the properties of the system. This, rather than a critical value of the Marangoni number, defines a criterion for feature formation.

Furthermore, the model is capable of quantitatively predicting the peak-to-valley heights of the smoothly varying thickness profile at different heating times and temperatures, using reasonable physical parameters as input. The model was used to define process trends to guide future development of this patterning methodology. The highest feature aspect ratios, $\frac{1}{2}h_{max}\lambda^{-1}$, can be achieved for thinner films, high surface energy differences between exposed and unexposed regions, a mask periodicity that is optimized for film thickness, and systems which possess both low viscosity and low self-diffusion coefficients. The dissipation of film topography at excessively long heating times was used to extract a diffusion coefficient at 120°C that matched a literature value[100] within 50%. Therefore, this demonstration could motivate the application of this combined theory/experimental methodology as a measurement method for surface energy changes and diffusion coefficients of complex polymer blends in confined thin films, using only inexpensive bench equipment and materials.

NOMENCLATURE

Latin

c	fractional concentration of the photo-generated polymer
c_0	peak fractional concentration of photo-generated polymer a exposure
h	local height of the film above the substrate; dimensional up to equation 4.8 and dimensionless thereafter,
h_{max}	dimensionless maximum film height attained over the course of heating
h_0	initial film thickness
t	time
x	space co-ordinate perpendicular to mask lines and parallel to the substrate

A	squared aspect ratio $A \equiv \lambda^2/{h_0}^2$
$\mathcal{D}$	diffusion coefficient of the photo-generated polymer within the blend
Pe	ratio of the surface tension-induced convective and diffusive timescales
T	temperature

Greek

λ	linewidth of the mask
μ	viscosity of the polymer
$\hat{\eta}$	peak-to-valley height of sinusoidal perturbation in film thickness
$\hat{\eta}_{max}$	maximum size of the perturbation in film thickness over the course of heating
γ	local surface tension of the blend
$\Delta\gamma$	surface tension of the photo-generated polymer minus that of the base film
γ_0	surface tension of the base polymer at the operating temperature
$\hat{\xi}$	size of sinusoidal perturbation in concentration
ψ_1, ψ_2	intermediate variables introduced for clarity, defined in equation 4.18

Chapter 4: Marangoni-Driven Patterning for 3D Shapes

In Chapter 3, Marangoni-driven patterning was studied for line-shaped patterns. The technique is not limited to lines, and in principle, any shape for which a corresponding mask is available can be patterned. Here we extend simulations to 3D shapes.

FORMULATION & ANALYSIS

Model

Relaxing the assumption that the exposure pattern is uniform in one direction, equations (3.8, 3.9) are written in vector form as:

$$\frac{\partial h}{\partial t} + \nabla.\left[\left(\frac{1}{3A}\right)h^3\nabla\{\gamma\nabla^2 h\} + \left(\frac{1}{2}\right)h^2\nabla\gamma\right] = 0 \tag{4.1}$$

$$\frac{\partial c}{\partial t} - \left(\frac{1}{Pe}\right)\nabla^2 c + \nabla\left[c\left\{\left(\frac{1}{2A}\right)h^2\nabla(\gamma\nabla^2 h) + h\nabla\gamma\right\}\right] = 0 \tag{4.2}$$

Since one period of the exposure pattern is simulated, symmetry conditions in film height, pressure and concentration apply at the boundaries:

$$\nabla h.\boldsymbol{n} = 0 \tag{4.3}$$

$$\nabla p.\boldsymbol{n} = \nabla(\gamma\nabla^2 h).\boldsymbol{n} = 0 \tag{4.4}$$

$$\nabla c.\boldsymbol{n} = 0 \tag{4.5}$$

where $\boldsymbol{n}$ is the normal at the boundary.

The linear dependence of concentration on surface tension is retained. Written non-dimensionally:

$$\gamma = 1 + (\Delta\gamma)c \tag{4.6}$$

Numerical Method

This system of equations was solved via the finite-difference method. A second-order scheme, incorporating upwinding for the first derivative of concentration in (4.2) for stabilization, along with explicit time stepping were employed.

RESULTS & DISCUSSION

Figure 4.1 shows the evolution of film topography and concentration for a 150 nm thick film exposed through a mask with triangular gaps of 60 μm side-length, resulting in 6.4% peak conversion, and subsequently heated to 120°C, corresponding to the experiments of Katzenstein *et al.*[102] The initial concentration profile is taken to be a step function, and the material property values in Table 3.1 are retained.

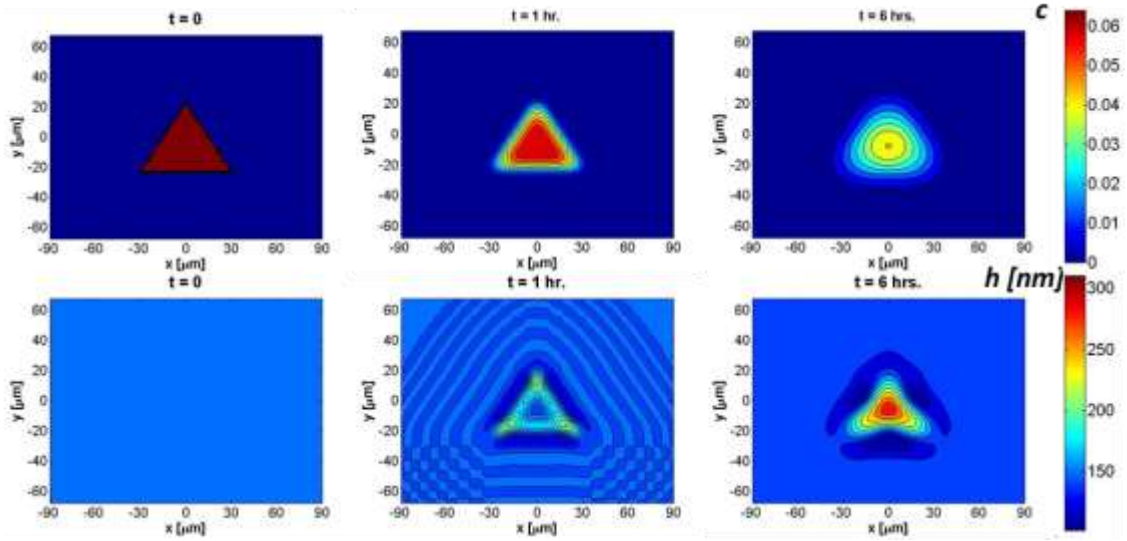

Figure 4.1 Concentration (top) and film height (bottom) profiles at 0 (left), 60 (middle) and 360 (right) minutes of heating.

It can be seen that due to diffusion, the step change in concentration broadens and the sharp corners round out over time. The evolution of film topography is qualitatively similar to the 1D case. At intermediate times, multiple peaks form where the concentration changes most rapidly, in this case at the corners of the exposed region. At long times, on the other hand, a single peak forms at the center of the exposed region. The transient peaks at intermediate times persist for more than an hour, as opposed to a few minutes for the 1D case. Figure 4.2 shows that the predicted topography agrees well with experimental observation.

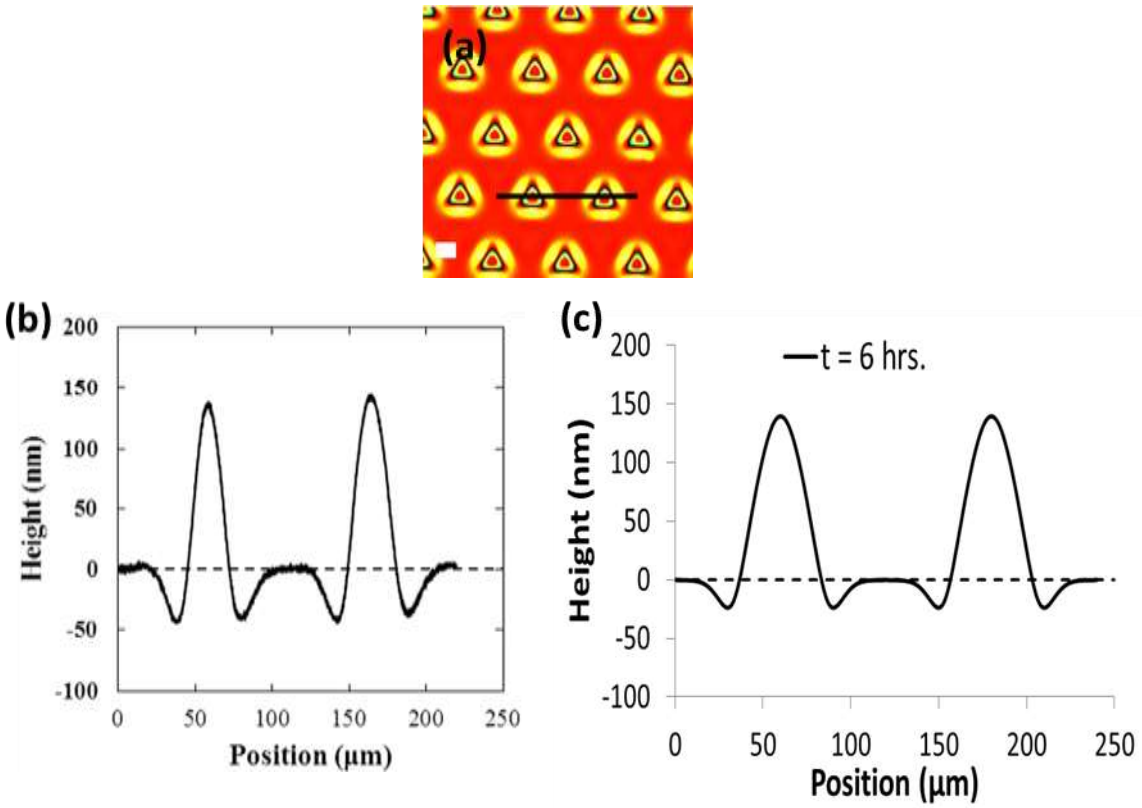

Figure 4.2 (a) Optical micrograph of triangular features. **(b)** Profilometry line scan across the black line shown in (a). **(c)** Equivalent fil profile prediction from simulations at t = 6 hrs.

CONCLUSIONS

Marangoni-driven patterning can be extended to 3D patterns. At intermediate times, multiple peaks form at the transitions between exposed and un-exposed regions, whereas at long times, a single peak forms at the center of the exposed region.

Chapter 5: Flow-Assisted Dielectrophoretic Assembly of Nanowires

INTRODUCTION

Semi-conducting nanowires and carbon nanotubes possess optical, mechanical and electronic properties which are both unique and tunable, and these have been exploited for important improvements in a breadth of applications including flexible electronics,[103] transistor scaling,[104] photonic computing,[105] photovoltaics,[106, 107] lithium-ion batteries,[108] thermoelectrics[109] and biosensing.[110] Many of these applications necessitate an array of nanowires arranged at precise locations on a substrate. While the growth of nanowires with specific properties has been demonstrated widely, their assembly into arrays on rigid and flexible substrates with the requisite density and precision while avoiding degradation in properties remains a challenge[111] in spite of the considerable attention it has received.[112, 113]

One of the most promising approaches for nanowire assembly[114] demonstrated to date is flow-assisted dielectrophoresis,[115, 116] wherein a suspension of nanowires is made to flow across the target substrate with (lithographically) pre-patterned electrode sites. When the suspension flowrate and electric field strength are tuned correctly, this results in the deposition of individual nanowires at each electrode site, aligned with the electric field. This approach combines parallel assembly over large areas with a high degree of precision, has the potential for high resolution, has demonstrated unprecedented yields (98%[116]) of accurately positioned and aligned nanowires and is facile to flexible substrates.

The dynamics of the nanowire are determined by interplay of hydrodynamic drag from the fluid and the dielectrophoretic force from the electric field. The two can be mediated primarily through suspension flowrate and electric field strength, but are also affected by the channel size, electrode configuration and material properties. When

hydrodynamic drag dominates, nanowires are carried past the electrode site without being captured, whereas when dielectrophoresis is dominant, multiple nanowires assemble at each site. A careful calibration of the flowrate and the applied field will therefore result in a precise number of nanowires at each site. In addition to these deterministic forces, nanowires also undergo Brownian diffusion; for higher pattern densities (and hence shorter nanowires), diffusion becomes increasingly strong making deterministic assembly difficult.[117]

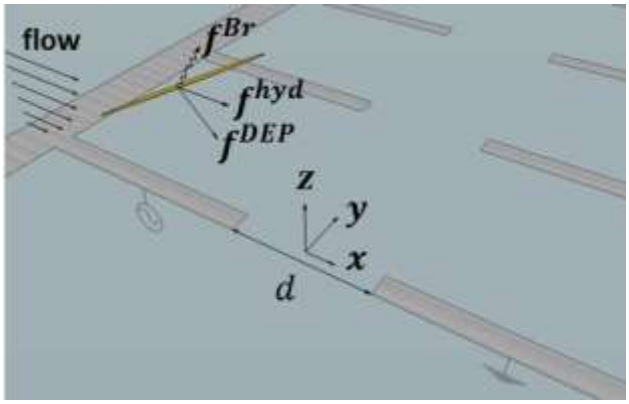

Figure 5.1 Schematic showing flow-assisted dielectrophoretic deposition. A nanowire in pressure-driven flow across a pre-patterned electrode site experiences forces (and torques) from fluid drag, the electric field and collisions with solvent molecules causing Brownian motion.

The promise of flow-assisted dielectrophoretic deposition notwithstanding, several questions critical to assessing its limits as well as understanding the criteria necessary for successful assembly remain unanswered.[114] What is the relationship between electric field-strength and suspension flowrate for the deposition of exactly one nanowire at each site? What effect do material properties, most notably the conductivity of the nanowire, have on the process? How does an increase in the desired pattern density affect the viability of assembly? Does Brownian diffusion place a lower limit on the minimum nanowire size that can be deposited reliably? Is there an efficient way to think

about how the many different experimental parameters determine the dynamics of the nanowire and the probability of successful assembly?

In order to address these questions, we develop simulations of the dynamics of an individual nanowire in pressure-driven flow within a parallel-plate channel and across an electrode site with an alternating electric field. In the sections below, we first outline my model and the geometry we consider. This is followed by a portrayal of the dynamics of nanowires under characteristic flowrates and voltages. We then consider the flowrate-field strength combinations necessary for successful assembly and compare with experimental observations. We note how the model implies scaling that clarifies how the myriad of experimental parameters affect nanowire dynamics. The role played by diffusion in mediating assembly is investigated, followed by the effect of pattern density on the conditions necessary for successful assembly and nanowire conductivity on the minimum nanowire length for which flow-assisted dielectrophoretic assembly is feasible.

FORMULATION & ANALYSIS

For my investigations we consider a nanowire of length l and radius a immersed in pressure-driven flow of volumetric flowrate Q and fluid viscosity μ within a parallel plate channel of height H and width w. The substrate is patterned with electrode sites composed of finger electrodes separated by a gap length d and an AC signal of root-mean square strength V_0 and angular frequency ω. The particle (p) and solvent (s) have electrical permittivities $\varepsilon_{p.s}$ and conductivities $\sigma_{p.s}$. The fluid flows in the x-direction, the z-coordinate is perpendicular to the substrate and the origin of the coordinate system is located at the center of the electrode gap (Figure 5.1).

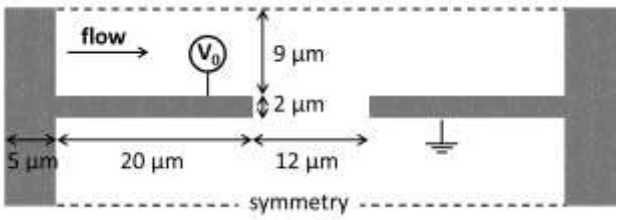

Figure 5.2 The geometry of finger electrodes for nanowire length l = 18 μm long nanowires. When nanowire length is varied, electrode dimensions and gap length are scaled accordingly.

For the base system, we use electrode geometry (Figure 5.2) as well as parameter values (Table 5.1) that coincide with the experiments of Freer and coworkers.[116] When particle length is varied, it's diameter as well as electrode dimensions (including the length of the gap) are scaled accordingly so that they remain fixed multiples of nanowire length.

Table 5.1: Base parameter values

Nanowire Geometry
Length $l = 18$ μm
Radius $a = 120$ nm

Channel Geometry
Height $H = 635$ μm
Width $w = 4.9$ cm

Flow
Volumetric flowrate $Q = 1.2$ ml/min.
Fluid viscosity $\mu = 2 \times 10^{-3}$ Pa. s

Electrode Geometry
Gap length d = 12 μm
Other dimensions as in Figure 5.2

Applied Field
RMS voltage $V_0 = 0.35$ V
Frequency $\omega = 2\pi(500$ Hz)

Particle Electrical Properties
Permittivity $\varepsilon_p = 24\varepsilon_0$
Conductivity $\sigma_p = 2 \times 10^3$ S/m

Fluid Electrical Properties
Permittivity $\varepsilon_s = 12\varepsilon_0$
Conductivity $\sigma_s = 1.9 \times 10^{-6}$ S/m

Simulation Methodology

Consider a dilute suspension of semiconducting nanowires (or carbon nanotubes) in a channel with the substrate patterned with electrode sites. The dynamics of the nanowire are described by[118]

$$\Delta \boldsymbol{r} = \boldsymbol{R}^{trans^{-1}} \cdot \left(\boldsymbol{f}^{DEP} + \boldsymbol{f}^{0,hyd} + \boldsymbol{f}^{Br} \right) \Delta t \tag{5.1}$$

$$\Delta \boldsymbol{\theta} = \boldsymbol{R}^{rot^{-1}} \cdot \left(\boldsymbol{t}^{DEP} + \boldsymbol{t}^{0,hyd} + \boldsymbol{t}^{Br} \right) \Delta t \tag{5.2}$$

Here $\Delta \boldsymbol{r}$ and $\Delta \boldsymbol{\theta}$ represent the positional and orientational displacement of the particle in time Δt. $\boldsymbol{f}$ and $\boldsymbol{t}$ denote force and torque which originate from dielectrophoresis (DEP), hydrodynamics (hyd) and Brownian diffusion (Br); the hydrodynamic force and torque ($\boldsymbol{f}^{0,hyd}$, $\boldsymbol{t}^{0,hyd}$) are for a particle held stationary. $\boldsymbol{R}^{trans}$ and $\boldsymbol{R}^{rot}$ are the translational and rotational hydrodynamic resistance tensors. Vectors and tensors are in bold lowercase and bold uppercase respectively.

Advancing in Time

Since the forces on the particle vary spatially, a mid-point algorithm[119] was employed:

$$\boldsymbol{r}^{*} = \boldsymbol{r} + \frac{1}{2} \boldsymbol{R}^{trans^{-1}} \cdot \left(\boldsymbol{f}^{DEP}(\boldsymbol{r}) + \boldsymbol{f}^{0,hyd}(\boldsymbol{r}) + \boldsymbol{f}^{Br}(\boldsymbol{r}) \right) \Delta t \tag{5.3}$$

$$\Delta \boldsymbol{r} = \boldsymbol{R}^{rot^{-1}} \cdot \left(\boldsymbol{f}^{DEP}(\boldsymbol{r}^{*}) + \boldsymbol{f}^{0,hyd}(\boldsymbol{r}^{*}) + \boldsymbol{f}^{Br}(\boldsymbol{r}^{*}) \right) \Delta t \tag{5.4}$$

The particle coordinate frame is defined to be the laboratory frame (shown in Figure 5.1) rotated such that the x-axis aligns with the major axis of the particle. The matrix $\boldsymbol{A}$ transforms between the lab and particle frames:

$$\hat{\boldsymbol{r}} = \boldsymbol{A}\boldsymbol{r} \tag{5.5}$$

$$\boldsymbol{R}^{trans} = \boldsymbol{A}\boldsymbol{R}^{trans}\boldsymbol{A}^{-1} \tag{5.6}$$

where a hatted symbol denotes a quantity in the particle frame.

$\boldsymbol{A}$ and a corresponding set of Euler parameters (quaternions) q are initialized consistent with the initial orientation of the particle and updated at each step:[120]

$$\Delta q = \frac{1}{2}\begin{bmatrix} q_4 & -q_3 & q_2 \\ q_3 & q_4 & -q_1 \\ -q_2 & q_1 & q_4 \\ -q_1 & -q_2 & q_3 \end{bmatrix}\Delta\boldsymbol{\theta} \tag{5.7}$$

$$\boldsymbol{A} = \begin{bmatrix} 1-2\left(q_2^2+q_3^2\right) & 2\left(q_1q_2+q_3q_4\right) & 2\left(q_1q_3-q_2q_4\right) \\ 2\left(q_2q_1-q_3q_4\right) & 1-2\left(q_3^2+q_1^2\right) & 2\left(q_2q_3-q_1q_4\right) \\ 2\left(q_3q_1+q_2q_4\right) & 2\left(q_3q_2-q_1q_4\right) & 1-2\left(q_1^2+q_2^2\right) \end{bmatrix} \tag{5.8}$$

Dielectrophoretic Force

Needle-like particles are often modeled as prolate ellipsoids[121, 122] and the dielectrophoretic force calculated via the *effective* dipole p:[123]

$$p_i = 2\pi a^2 l\varepsilon_s \,\mathrm{Re}(K_i)e_i \tag{5.9}$$

$$\boldsymbol{f}^{DEP} = (\boldsymbol{p}.\nabla)\boldsymbol{e} \tag{5.10}$$

$$\boldsymbol{t}^{DEP} = \boldsymbol{p}\times\boldsymbol{e} \tag{5.11}$$

The Clausius-Mossotti factor K is a measure of the polarizability of the particle relative to the solvent. For an ellipsoid, it is anisotropic:[124]

$$K_i = \frac{\varepsilon_p^* - \varepsilon_s^*}{3\left[\varepsilon_s^* + (\varepsilon_p^* - \varepsilon_s^*)L_i\right]} \tag{5.12}$$

$\varepsilon_{p,s}^* = \varepsilon_{p.s} - \left(\sigma_{p,s}/\omega\right)i$ are complex permittivies of the particle and the solvent. L is the depolarization factor determined by the geometry of the particle. For highly elongated particles, $L \approx 0, 1/2$ along the long and short axes respectively.

Effective dipole moment (EDM) theory relies on the simplification that the electric field varies over a length-scale much longer than the particle.[125, 126] For dielectrophoretic assembly of nanowires, however, the electrode gap is comparable in length to the nanowire. To account for this, we discretize the nanowire lengthwise into smaller cylinders, calculating the total force and torque as a mean over the length of the wire..

Hydrodynamics

For a slender body of aspect ratio $s = 2a/l$ immersed in a fluid the components of the translational resistance matrix $\boldsymbol{R^{trans}}$ are[127] $4\pi\mu l/\ln(2/s)$ and $8\pi\mu l/\ln(2/s)$ along the long and short axes of the particle respectively, while the component of the rotational resistance matrix $\boldsymbol{R^{rot}}$ about the short-axes is $4\pi\mu l^3/3\ln(l/a)$.

The hydrodynamic force $\boldsymbol{f^{0,hyd}}$ and torque $\boldsymbol{t^{0,hyd}}$ for a particle held stationary in Poiseuille flow follow from a generalization of Faxen's law. A stationary spheroid of radius a and length $2b$ in an ambient Stokes flow u experiences a hydrodynamic force and torque given by[128, 129]

$$\boldsymbol{f} = \boldsymbol{R}^{trans}.\left[\boldsymbol{u_0} + \frac{1}{3!}\left(D^2\boldsymbol{u}\right)_0 + \cdots\right] \tag{5.13}$$

$$\boldsymbol{t} = \boldsymbol{Q}.\left[\left(\boldsymbol{b}\times\boldsymbol{u}\right)_{\boldsymbol{0}} + \frac{3!2!}{5!}\left(D^2\boldsymbol{b}\times\boldsymbol{u}\right)_0 + \cdots\right] \tag{5.14}$$

The subscript 0 denotes that the quantity is evaluated at the center-of-mass of the particle, and

$$D^2 = b^2\frac{\partial^2}{\partial x^2} + a^2\frac{\partial^2}{\partial y^2} + a^2\frac{\partial^2}{\partial \hat{z}^2} \tag{5.15}$$

$$\boldsymbol{b} = \begin{bmatrix} b^2\,\partial/\partial x \\ a^2\partial/\partial y \\ a^2\partial/\partial \hat{z} \end{bmatrix} \tag{5.16}$$

$$\boldsymbol{Q} = \begin{bmatrix} R_{xx}^{rot}/2a^2 & & \\ & R_{yy}^{rot}/a^2+b^2 & \\ & & R_{zz}^{rot}/a^2+b^2 \end{bmatrix} \tag{5.17}$$

For planar pressure-driven flow

$$\boldsymbol{u} = \frac{6Q}{Hw}\begin{bmatrix} \frac{z}{H}\left(1-\frac{z}{H}\right) \\ 0 \\ 0 \end{bmatrix} \tag{5.18}$$

This gives

$$\boldsymbol{f} = \frac{6Q}{Hw}\left(\frac{z}{H}\left(1-\frac{z}{H}\right)-\frac{b^2A_{xz}^2+a^2\left(A_{yz}^2+A_{zz}^2\right)}{3H^2}\right)\begin{bmatrix} R_{xx}^{trans}A_{xx} \\ R_{yy}^{trans}A_{yx} \\ R_{zz}^{trans}A_{zx} \end{bmatrix} \tag{5.19}$$

$$\hat{\boldsymbol{t}} = \frac{6Q}{H^2w}\left(1-\frac{2z}{H}\right)\boldsymbol{R}^{rot}\begin{bmatrix} \left(\frac{b^2}{2a^2}\right)A_{xz} \\ \left(\frac{a^2}{a^2+b^2}\right)A_{yz} \\ \left(\frac{a^2}{a^2+b^2}\right)A_{zz} \end{bmatrix}\times\begin{bmatrix} A_{xx} \\ A_{yx} \\ A_{zx} \end{bmatrix} \tag{5.20}$$

This accounts for the curvature of the flow field but not for the effects of the channel walls. Wall effects have been shown to decrease with increasing particle asphericity.[129]

Brownian Motion

Finally, the Brownian force (and torque) have the following stochastic properties:[130]

$$\left\langle \boldsymbol{f}^{Br}(t)\right\rangle = 0 \tag{5.21}$$

$$\left\langle \boldsymbol{f}^{Br}(0)\,\boldsymbol{f}^{Br}(t)\right\rangle = 2kT\boldsymbol{R}^{trans}\boldsymbol{I}\,\delta(t) \tag{5.22}$$

where δ is the Dirac delta function and $\boldsymbol{I}$ the identity tensor.

Computing the Electric Field

The electric field is given by Laplace's equation for potential[131]

$$\nabla^2 V = 0 \tag{5.23}$$

Insulation/symmetry boundary conditions are applied at the substrate as well as the extremities of the solution domain:

$$\boldsymbol{n}.\nabla V = 0 \tag{5.24}$$

while the potential is specified to be V_0 and 0 at the biased and grounded electrodes respectively. The electric field is solved for via finite-element simulations in COMSOL using quartic Lagrange elements for improved accuracy of derivatives. The solution is exported at the nodes of the finite-element mesh, and during dynamic simulations is interpolated between these values.

Scaling

Scaling the electric field by V_0/d, equation (5.10) implies that the dielectrophoretic force can be scaled by $(2\pi a^2 l)\left(\varepsilon_s \mathrm{Re}K_{long}\right)\left)(V_0^2/d^3\right)$, where $\mathrm{Re}K_{long}$ refers to the real part of the long-axis Clausius-Mossotti factor. We scale the hydrodynamic force by $\dot{\gamma} R_{long} l/2$, which is the drag on a wire oriented in the x-direction and $l/2$ above the substrate. $R_{long} = 4\pi\mu l/ln(2/s)$ is the translational resistance along the major axis, while $\dot{\gamma} = 6Q/H^2 w$ refers to the shear rate at the substrate. The Brownian force is scaled by kT/d. Then, equation (5.1) describing the dynamics of the wire reduces to the following non-dimensional form:

$$\Delta\tilde{\boldsymbol{r}} = \tilde{\boldsymbol{R}}^{\boldsymbol{trans}^{-1}} \cdot \left(\boldsymbol{f}^{\boldsymbol{DEP}} + \left(\frac{\overline{F}^{hyd}}{\overline{F}^{DEP}} \right) \boldsymbol{f}^{\boldsymbol{0,hyd}} + \left(\frac{\overline{F}^{Br}}{\overline{F}^{DEP}} \right) \boldsymbol{f}^{\boldsymbol{Br}} \right) \Delta\tilde{t} \tag{5.25}$$

Here $\bar{F}$ are the aforementioned force scales and $\tilde{}$ indicates a dimensionless quantity. Resistance is scaled by R_{long}, position by l and time by $R_{long} l/\overline{F}^{DEP}$.

We refer to the ratio of the dielectrophoretic and hydrodynamic force scales as the dielectrophoretic number *Di*. The other force ratio can then be written in terms of *Di* and the Peclet number *Pe*, which is traditionally a ratio of hydrodynamic and Brownian forces.

$$Di \equiv \frac{\overline{F}^{DEP}}{\overline{F}^{hyd}} = \left(\frac{\varepsilon_s \operatorname{Re} K_{long}}{4\mu} \right) \left(s^2 \ln \frac{2}{s} \right) \left(\frac{l}{d} \right) \frac{\left(V_0 / d \right)^2}{\dot{\gamma}} \tag{5.26}$$

$$Di \times Pe \equiv \frac{\overline{F}^{DEP}}{\overline{F}^{Br}} = \frac{\pi}{4kT} \left(\varepsilon_s \operatorname{Re} K_{long} \right) s^2 \left(V_0 / d \right)^2 l^3 \tag{5.27}$$

The two dimensionless groups *Di* and *DiPe* are defined such that they have large values when dielectrophoresis is dominant.

RESULTS & DISCUSSION

Hydrodynamic Force Calculation

The hydrodynamic model outlined above (based on Faxen's law) accounts for the curvature of the flow field but neglects interactions with the substrate. Figure 5.3 shows estimates of the lift force (i.e. perpendicular to the substrate) for an ellipsoid 0.6*l* above the wall in semi-infinite shear flow as a function of its orientation. Shown are calculations based on the boundary-element method that include the wall from Gavze & Shapiro[129] as well as estimates using the method employed here for two different particle aspect ratios. Predictions based on Faxen's law are qualitatively similar to when hydrodynamic interactions with the wall are included but underestimate the magnitude of the force. Gavze and Shapiro[129] show that wall effects become increasingly irrelevant for

more extreme particle aspect ratios. The discrepancy between the two calculations is 60% at δ = 0.7 and 30% at δ = 0.1. The nanowires used in Freer *et al*'s experiments and simulated here have δ = 0.013.

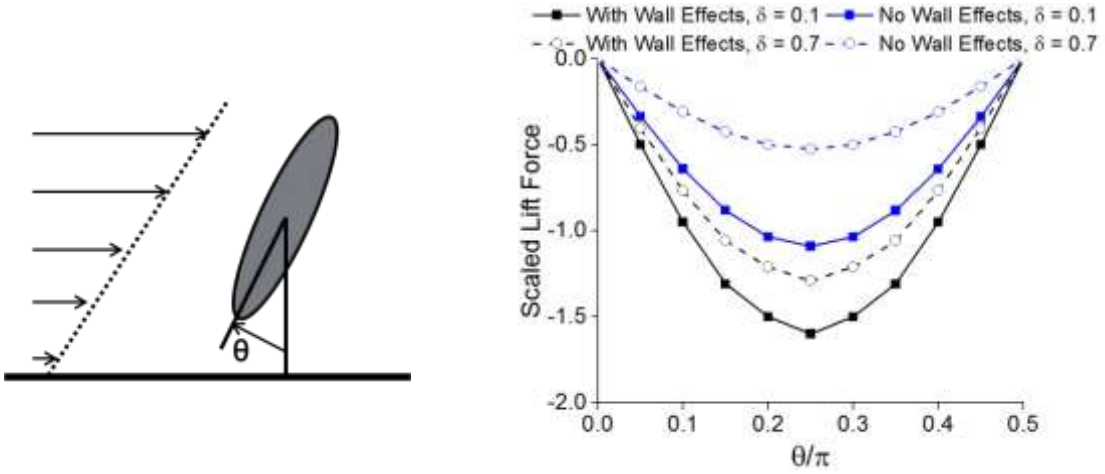

Figure 5.3: Comparison of hydrodynamic lift force calculations based on Faxen's law ignoring wall effects with boundary element simulations including them for two different particle aspect ratios

Dielectrophoretic Force Calculation

The most rigorous calculation of the dielectrophoretic force is by integrating the Maxwell stress tensor (MST) over the surface of the particle. While this approach is unparalleled in accuracy, it makes dynamic simulations computationally expensive since it necessitates that the electric field be solved for at each time step with the particle present. Due to its simplicity, the effective dipole moment (EDM) moment method is most commonly used in the literature to estimate the dielectrophoretic force and torque. However, it assumes that the electric field varies over a length-scale significantly larger than the particle, which does not apply to nanowire assembly with the electrode gap and nanowire being comparable in length. The discretized EDM approach used here is meant to mitigate errors arising from this assumption.

Figure 5.4 shows a comparison of the dielectrophoretic force calculated in this way versus a rigorous calculation based on the Maxwell stress tensor (MST) from literature.[132] As is evident, a discretized EDM approach performs reasonably well in matching MST predictions qualitatively, while the standard EDM approach does not. This serves as a caution against employing the latter for dielectrophoretic assembly of individual particles. The agreement between the discretized EDM and MST approaches improves with increasing distance from the substrate; these results pertain to a 2 μm nanowire with its surface 100 nm from the substrate.

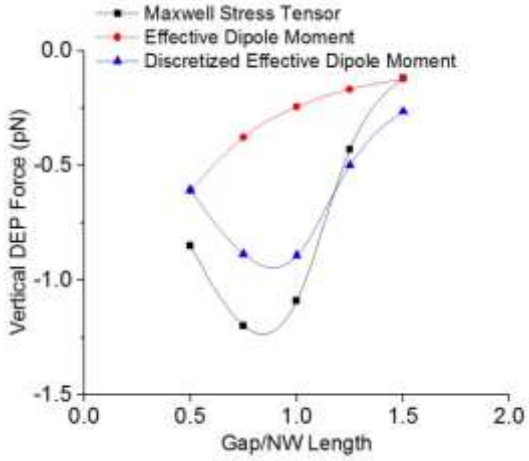

Figure 5.4: Comparison of dielectrophoretic force from a rigorous Maxwell stress tensor calculation[132] with estimates based on the standard and discretized effective dipole-moment method. These are for 2 μm long nanowires 200 nm in diameter with their centers 300 nm above parallel plate electrodes and oriented in the plane of the substrate and perpendicular to electrode edges.

The Electric Field

Figure 5.5 shows the electric field strength and direction for a 12 μm long gap and a 350 mV signal. The electric field is strongest at the electrode tips, and the field vectors show that a particle that tends to align with its major axis along the field will orient along the gap.

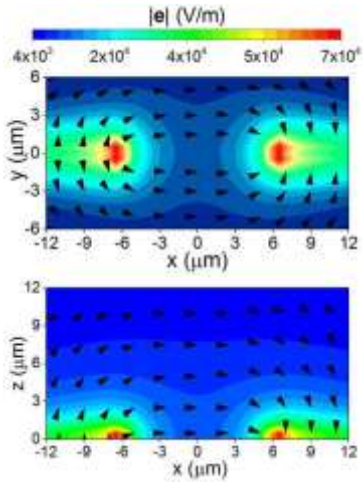

Figure 5.5: The electric field at $z = 0$ (top) and $y = 0$ (bottom) at $V_0 = 0.35$ V for a 12 μm electrode gap. The color indicates the magnitude of the field and the arrows its direction.

Dynamics of a Nanowire During Flow-Assisted Dielectrophoretic Deposition

The dielectrophoretic force on the nanowire is strongest at the electrode site and decays moving away from the substrate. The hydrodynamic drag, on the other hand, increases moving away from the substrate and towards the channel center-line. Therefore, there exists a finite region next to the substrate within which the electric field is strong enough to resist fluid drag and capture the nanowire.

Figure 5.6(a) depicts the trajectory of an 18 μm long nanowire as it comes across a 12 μm long electrode gap. The center of the nanowire is initially 18 μm upstream of the center of the electrode gap and 8 μm above the substrate. It moves with the flow only as far as the center of the gap and is pulled towards the substrate by the electric field, finally coming to rest spanning the gap.

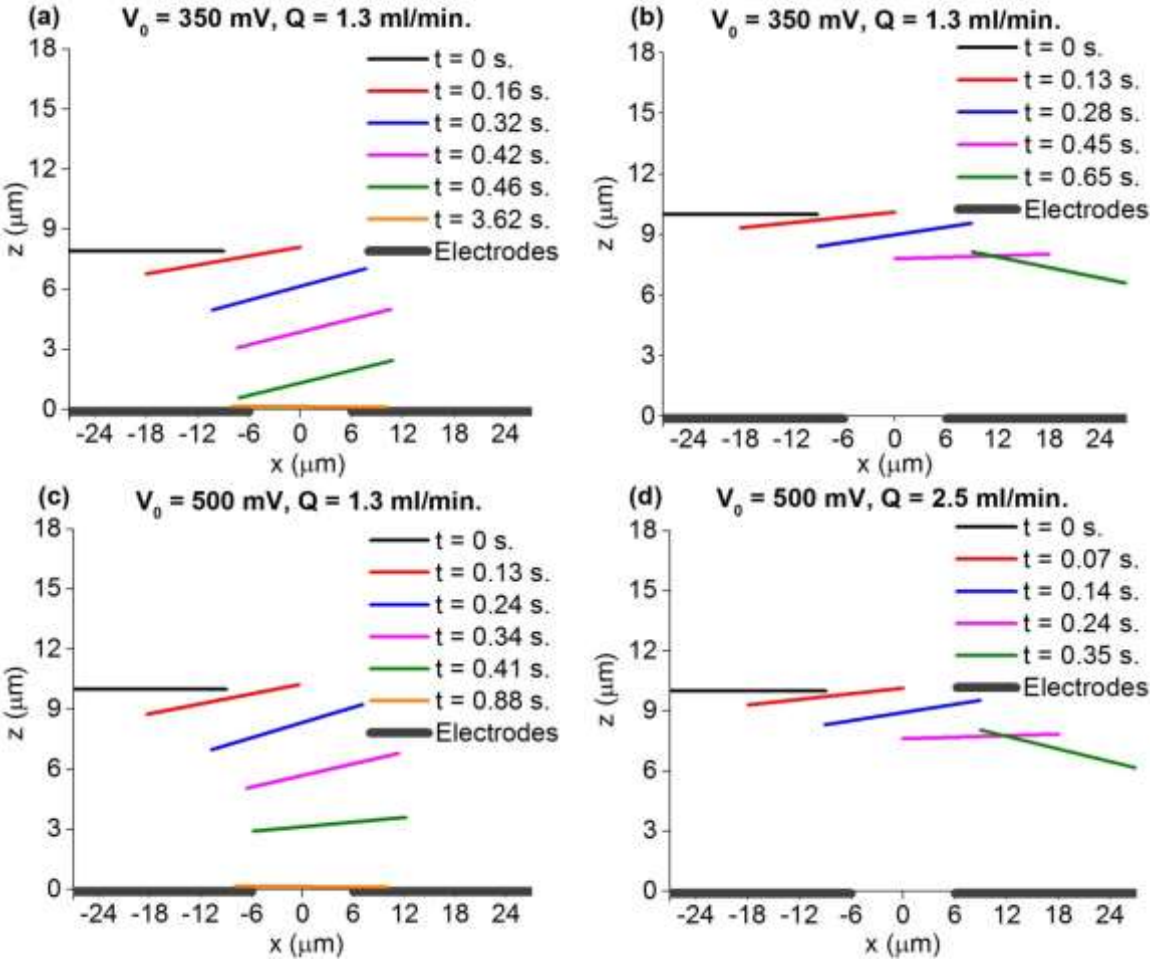

Figure 5.6: (a) Dynamics of an 18 μm long nanowire initially at x = -18 μm and z = 8 μm at 350 mV and 1.3 ml/min. The electric field pulls the nanowire in place and aligns it along the gap **(b)** When initially at z = 10 μm, the nanowire is carried away by the fluid without being captured. (**c**) Increasing the voltage to 500 mV results in capture even when initially at z = 10 μm. (**d**) Increasing the flowrate to 2.5 ml/min results in escape even at 500 V.

Figure 5.6(b) shows the trajectory of an identical nanowire that starts 10 μm above the substrate. At this distance, the electric field is too weak to counteract the fluid drag, and the nanowire is seen to flow across and past the gap without being captured even as it descends due to the electric field.

Electric field strength and suspension flowrate are convenient ways to mediate these dynamics. Figure 5.6(c) illustrates how the dynamics of the nanowire in Figure 5.6(b) alter when the electric field strength is increased to 500 mV. Instead of escaping, the nanowire is captured. Now increasing the suspension flowrate to 2.5 ml/min. results in the nanowire escaping even at 500 mV as shown in Figure 5.6(d).

Capture Criteria: Field Strength vs. Flowrate

It is clear that in order to be captured, a nanowire must arrive within a capture zone, the region next to the substrate within which the dielectrophoretic force dominates fluid drag.[115] The width of this region, which we refer to as the capture width, is determined by the relative strength of dielectrophoresis and hydrodynamics within a given experimental setup.

Figure 5.7(a) shows the capture width, defined as the maximum initial height (z_0) of a nanowire at $x_0 = -l$ for a $\geq$ 5% probability of being captured (100 particles were seeded at $x_0 = -l$ and various z_0). As seen earlier, higher voltages and lower flowrates result in an increased capture width, implying a greater likelihood of capture. For the moderate flowrates and voltages shown, capture widths range between approximately one-third and two-thirds nanowire length.

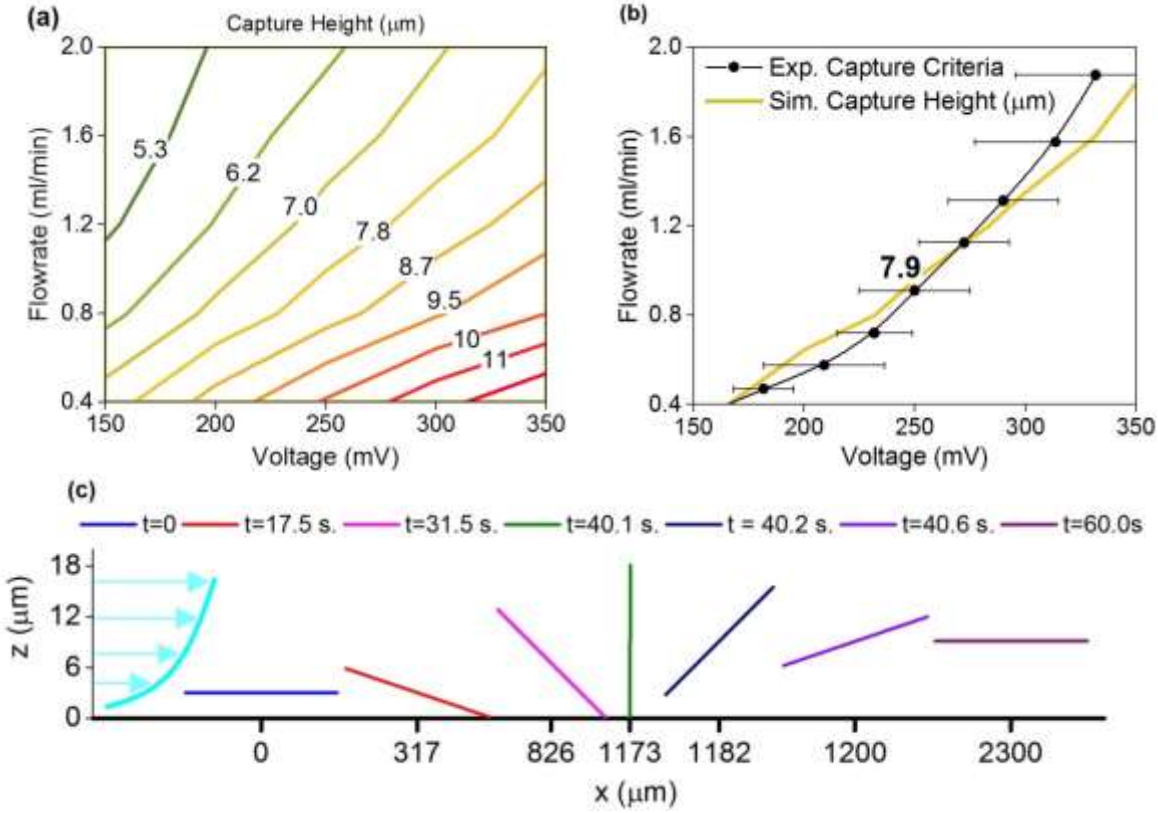

Figure 5.7: (a) The maximum distance from the substrate within which a nanowire at x = -18 μm needs to be to have a 5% probability of capture as a function of the applied voltage and volumetric flowrate (**b**) Comparison of the criteria for capture observed experimentally[116] with capture distance (**c**) Pole-vaulting motion of a nanowire initially at z = 3 μm (no electric field). The x-axis is not to scale and the particle x-positions are labeled.

Due to steric and hydrodynamic effects as well as their anisotropy, ellipsoidal particles in pressure-driven flow are known distribute themselves non-uniformly across the channel height.[133] Figure 5.7(c) shows the 'pole-vaulting' motion[134] of an 18 μm long nanowire that is initially 3 μm above the substrate. Shear flow adjacent to the wall causes it to tumble (i.e. undergo full rotations), and as it does so, steric effects push it away from the wall. Therefore, there results at steady state a depletion layer next to the channel walls largely void of particles.

In flow-assisted dielectrophoretic assembly, whether or not nanowires are captured depends upon the relative magnitude of the capture and depletion layer widths. If the depletion width exceeds the capture width, no nanowires arrive in the region where dielectrophoresis dominates and thus none are captured. On the other hand when the capture width is greater than the depletion width, nanowires are assembled successfully.

Figure 5.7(b) shows the capture curve observed by Freer and coworkers in their experiments;[116] for flowrate-voltage combinations lying below the curve, nanowires were deposited at the electrode sites, whereas above the curve, no wires were deposited. Note that their capture curve corresponds to a capture width of 7.9 μm. For flows with a comparable balance of hydrodynamics and diffusion (represented by the Peclet number), the depletion layer width has been shown to be slightly less than one-half particle length.[135] Therefore, a critical capture width of 7.9 μm for these 18 μm long nanowires agrees well with the understanding that the relative sizes of the capture and depletion widths determines whether nanowires are captured.

Scaling

The dynamics of the nanowire and hence the likelihood of successful assembly depend upon a myriad of factors: material properties (viscosity of the fluid and the electrical conductivity and permittivity of the fluid and nanowire), nanowire and gap lengths, the geometry of the electrodes and the channel and experimental parameters (flowrate, voltage and frequency).

It is clear from equation (5.25) that for a given electrode geometry, the dynamics of the nanowire are determined by *Di* and *DiPe*. Therefore, scaling reduces the number of parameters from the many mentioned earlier to two. They represent the strength of dielectrophoresis relative to hydrodynamics and diffusion respectively, with larger values

representing stronger dielectrophoresis. Large values of *Di* indicate that dielectrophoresis is dominant over hydrodynamic drag, whereas large values of *DiPe* imply that dielectrophoresis is dominant over diffusion.

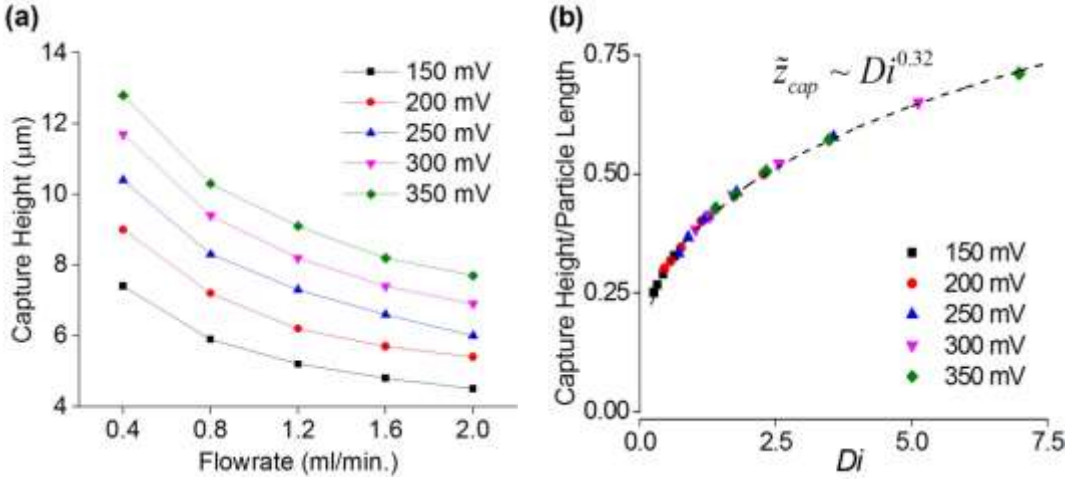

Figure 5.8: (a) Capture height plotted against flowrate for 5 different voltage values. **(b)** When plotted against the dielectrophoretic number, the simulated capture heights at varying flowrate and voltage collapse onto a single curve.

Figure 5.8(a) shows the capture width for 18 μm long wires as a function of flowrate at 5 different applied voltages. When plotted against *Di* in Figure 5.8(b), non-dimensional capture distance $\tilde{z}_{cap}$ at the various voltages collapses onto a single curve, indicating that the dielectrophoretic number is indeed the relevant dimensionless group.

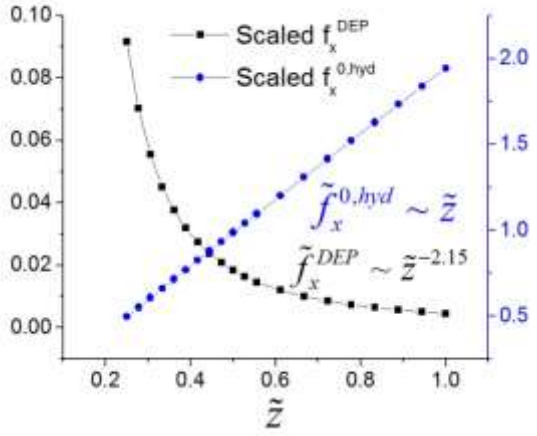

Figure 5.9: Non-dimensional dielectrophoretic and hydrodynamic forces for a nanowire oriented in the x direction as a function of distance from the substrate. The dielectrophoretic force is for a nanowire with its center directly above the electrode tip (x = 6 μm).

Figure 5.8(b) also shows that capture width is proportional to $Di^{0.32}$. This dependence is a result of how the dielectrophoretic force weakens moving away from the substrate, shown in Figure 5.9, due to the decaying electric field. The hydrodynamic force, on the other hand, varies linearly close to the substrate. The capture height is the distance from the substrate at which these forces are equal:

$$\overline{F}^{DEP}\tilde{z}_{cap}^{-2.15} = \overline{F}^{hyd}\tilde{z}_{cap} \tag{5.28}$$

$$\Rightarrow \tilde{z}_{cap} \propto Di^{0.32} \tag{5.29}$$

This simple scaling argument reproduces the relationship between capture distance and dielectrophoretic number observed in simulations.

The Role Played by Diffusion

Next we investigate the role played by diffusion, the importance of which for a given system is represented by $DiPe$. Since diffusion strengthens with reducing size, it is likely to play an important role in determining how increasing pattern density affects the viability of assembly.

We've seen that nanowire dynamics are defined by the parameters Di and $DiPe$: Di represents the ability of the dielectrophoretic force to overcome hydrodynamic drag, with large values of Di favoring assembly; $DiPe$ is a measure of the importance of diffusion relative to dielectrophoresis, with larger values implying weaker diffusion. We have also seen in Figure 5.7(b) that successful capture corresponds to a capture distance of $0.44l$. Figure 5.10 shows, as a function of $DiPe$, the value of Di for which 5%[**] of 100 particles released at $\tilde{z} = 0.44$ are captured. Figure 5.10 is the dimensionless analogue of the capture curve in Figure 5.7(b), with successful capture expected in the parameter space above the curve. Whereas Figure 5.7(b) shows the conditions necessary for successful assembly for a given set of material properties, channel geometry and nanowire size, Figure 5.10 includes variations in these through the dimensionless groups.

[**] For a lower (higher) capture probability, the Di needed for capture will be lower (higher) but qualitatively similar

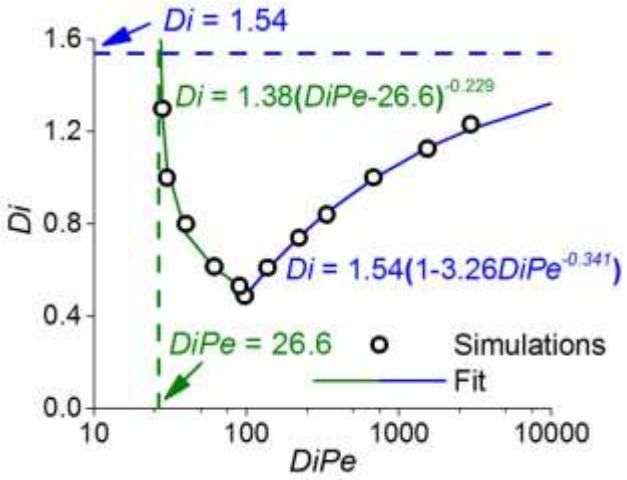

Figure 5.10: Dimensionless capture curve showing, as a function of *DiPe*, the dielectrophoretic number *Di* for which the capture distance is 0.44*l* (as shown in Figure 5.7(b), this capture distance corresponds to successful assembly in experiments). Successful capture is expected in the parameter space above the curve.

We see in Figure 5.10 that the capture curve asymptotes at large *DiPe*, indicating that beyond a certain value, the dynamics of the particle and hence the probability of assembly become insensitive to *DiPe*. At intermediate values of *DiPe*, assembly is aided by decreasing values of *DiPe* as capture is predicted for a larger region of the parameter space. However, for *DiPe* < 98, the *Di* needed for assembly increases rapidly.

Increasing values of *DiPe* indicate weakening diffusion. Therefore, for large *DiPe* Brownian motion is negligible and the dimensionless capture curve in Figure 5.10 asymptotes as particle dynamics are driven by hydrodynamics and dielectrophoresis only. The asymptotic value of *Di*=1.54 needed for capture at high *DiPe* when diffusion is negligible can also be recovered by substituting $\tilde{z}_{cap} = 0.44$ in the relationship depicted in Figure 5.8(b).

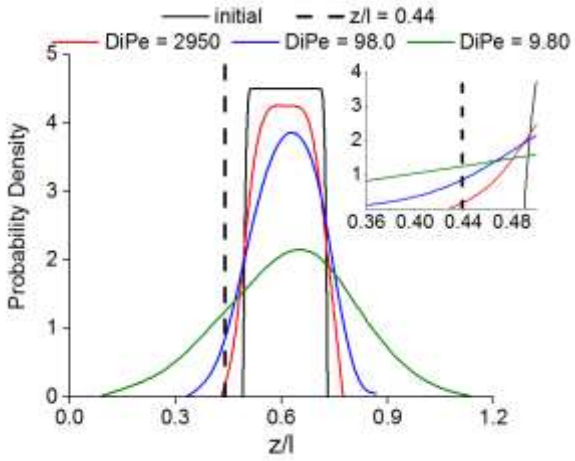

Figure 5.11: For a uniform distribution of particles released at $x = -2l$, the distribution at $x = -l$ is shown at three different values of *DiPe*.

At intermediate values of *DiPe*, decreasing *DiPe* aids capture because increasing diffusion distributes particles more broadly. Figure 5.11 shows how an initially uniform distribution of 100 particles all outside the capture zone evolves as they convect a distance equal to one particle length, at three values of *DiPe*. With decreasing *DiPe* increasing diffusion distributes particles more widely, as a result of which some particles move into the region where the electric field is able to capture them.

For $DiPe < 98$, the *Di* necessary to ensure capture increases rapidly because at this point diffusion is too strong for the dielectrophoretic force to capture the particle. For $DiPe > 98$, capture is limited by hydrodynamic drag; within this regime, increasing diffusion helps capture because it distributes particles more broadly while still allowing the electric field to capture them. For $DiPe < 98$, on the other hand, capture is limited by diffusion; increasing diffusion necessitates a stronger dielectrophoretic force for capture.

Pattern Density & Nanowire Conductivity

One of the features most critical to assessing the applicability of a nanowire deposition technique is the pattern densities it can achieve. Thus far, demonstrations of

dielectrophoretic assembly remain limited to nanowires tens of microns in length, whereas some of the most obvious potential applications such as field-effect transistors in which a single carbon nanotube constitutes the channel between source and drain necessitate assembly well below 100 nm.

Figure 5.12 shows capture curves corresponding to $\tilde{z}_{cap} = 0.44$ for various nanowire lengths. Gap length remains a fixed fraction of nanowire length ($l/d = 1.5$) as particle size is varied. Shorter wires are seen to be captured at lower voltages and higher flowrates. This is because for a given applied voltage, the electric field increases with decreasing gap length.

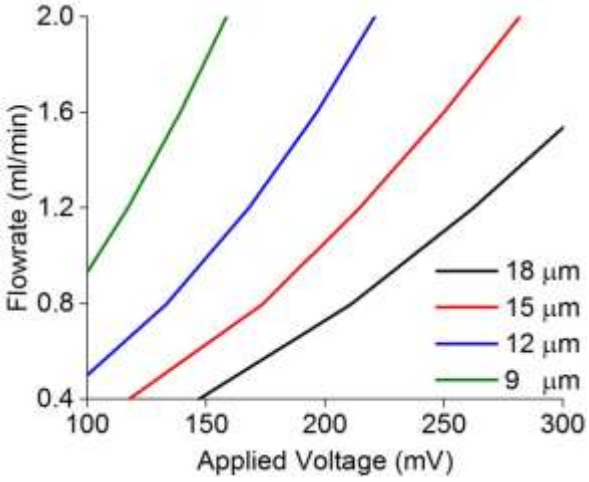

Figure 5.12: Comparison of dielectrophoretic force predictions based on our discretized effective dipole moment approximation and a rigorous Maxwell stress tensor calculation.[132] These are for 2 μm long nanowires 0.3 μm above parallel plate electrodes.

One of the advantages of flow-assisted dielectrophoretic assembly is that it can be applied to any semiconducting particle. Amongst the various relevant material properties, particle conductivity is most significant in determining the dielectrophoretic force it experiences. Both semi-conductor nanowires and carbon nanotubes can span a wide range of conductivities.

Figure 5.13(a) depicts the Clausius-Mossotti factor along the particle's major axis K_{long} as a function of the frequency of the applied field for three different particle conductivities. For high conductivities, K_{long} is unchanged over practical frequencies. At 2 S/m, K_{long} drops above 0.1 MH*z* but stays positive across the range of practical frequencies. For low conductivities, the Clausius-Mossotti factor is negative at large frequencies, meaning that particles are repelled from the electrodes.

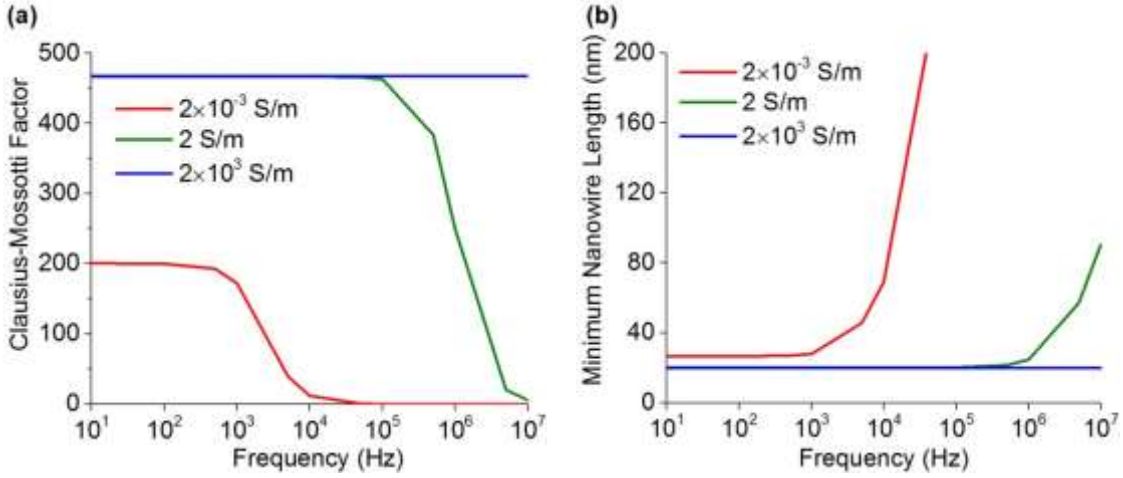

Figure 5.13: (a) The Clausius-Mossotti factor along the long axis as a function of field frequency for three different particle conductivities. (**b**) Minimum nanowire length for which flow-assisted dielectrophoretic assembly is feasible.

The transition from a diffusion-aiding-capture to a diffusion-inhibiting-capture regime occurs at $DiPe$ = 98. Below this value, diffusion rapidly becomes prohibitive; therefore, it is prudent to ensure that experimental parameters are chosen such that $DiPe$ ≥ 98. The maximum electric field ($\sim V_0/d$) is limited by dielectric breakdown of solvent molecules, which occurs at ~ 60 MV/m.[136] Since $DiPe \propto (V_0/d)^2 l^3$, this combination of a minimum *DiPe* and maximum electric field implies a minimum nanowire length for which successful assembly is achievable. Figure 5.13(b) shows this minimum length as a function of frequency for the three different particle conductivities. It is 20 nm for 2000

S/m nanowires, and increases in accordance with the Clausius-Mossotti factor with decreasing particle conductivity or increasing frequency.

CONCLUSIONS

Flow-assisted dielectrophoretic deposition exploits a precise balance of competing impulses on a nanowire; suspension flowrate and applied field strength are the most convenient ways to mediate its dynamics. Within a finite distance from the substrate, there exists a depletion layer largely void of nanowires (due to hydrodynamics, steric effects and nanowire anisotropy) and a capture zone (due to dielectrophoresis competing with hydrodynamics). Nanowires are captured when the capture width exceeds the depletion width; otherwise they are carried away with the flow. Successful assembly is aided by strong electric fields and low flowrates.

Apart from flowrate and voltage, nanowire assembly is affected by a myriad of factors, including field frequency, gap width, nanowire length and material properties. Scaling reveals two dimensionless groups as the fundamental variables governing the assembly process, simplifying our understanding of how various experimental systems compare in terms of ease of assembly. Capture results for various flowrates and applied voltages collapse onto a single curve when plotted non-dimensionally.

With decreasing nanowire length, increasing diffusion distributes particles more broadly, thereby aiding assembly by moving some particles into the region where the electric field is strong enough for capture. However, the strength of diffusion eventually becomes prohibitive, and in conjunction with an upper limit on the applied electric field due to dielectric breakdown of solvent molecules, imposes a minimum nanowire length for which flow-assisted dielectrophoretic assembly is feasible. This is 20 nm for 2000

S/m nanowires, and varies with field frequency and particle and solvent electrical properties in accordance with the Clausius-Mossotti factor.

These investigations yield a fuller understanding of the dynamics of the assembly process, its limits and how experiments may be designed for successful assembly for various applications. It is prudent to remember that the model herein ignores inter-particle interactions and hence applies only to the dilute suspensions that are commonly employed in dielectrophoretic assembly. Further, the focus here is on ensuring nanowire capture and avoiding escape with flow or diffusion; the *quality* of assembly (i.e. the extent of orientational misalignments or capture at undesired locations such as bus bars) has been studied elsewhere.[115, 137, 138]

NOMENCLATURE

Latin

a	nanowire radius
d	length of the gap between the biased and grounded electrodes
$\boldsymbol{e}$	electric field
$\boldsymbol{f}^{DEP}$	force on the nanowire from dielectrophoresis
$\boldsymbol{f}^{0,hyd}$	force on a nanowire held stationary from hydrodynamic drag
$\boldsymbol{f}^{Br}$	force on the nanowire from collisions with solvent molecules causing Brownian diffusion
k	Boltzmann constant
l	nanowire length
$\boldsymbol{p}$	*effective* dipole of the particle
$\boldsymbol{r}$	location of the particle's center
t	time
$\boldsymbol{t}^{DEP}$	torque on the nanowire from dielectrophoresis
$\boldsymbol{t}^{0,hyd}$	torque on a nanowire held stationary from hydrodynamic drag
$\boldsymbol{t}^{Br}$	torque on the nanowire from collisions with solvent molecules causing Brownian diffusion
w	width of the channel in the vorticity direction
H	height of the channel perpendicular to the substrate
K	Clausius-Mossotti factor, a measure of particle polarizability relative to the solvent
$\boldsymbol{R}^{rot}$	rotational resistance tensor

$\boldsymbol{R}^{trans}$	translational resistance tensor
T	temperature
Q	volumetric flowrate of suspension
V_0	applied root-mean square voltage

Greek

δ	Dirac delta function
ε_p	electrical permittivity of the particle
ε_s	electrical permittivity of the solvent
ε^*_p	complex permittivity of the particle
ε^*_s	complex permittivity of the solvent
θ	orientation of the particle
μ	viscosity of the solvent
ω	angular frequency of the AC electric field
σ_p	electrical conductivity of the particle
σ_s	electrical conductivity of the solvent

Chapter 6: Conclusions

Three early-stage techniques for the fabrication of metallic nanostructures, creation of controlled topography in polymer films and precise deposition of nanowires and nanotubes were studied. Mathematical models and computational simulations clarify how the interplay of multiple physical processes drives dynamics, identify limits of throughput and resolution for each technique and yield a rational approach to optimizing experimental parameters to target specific structures efficiently.

Evaporation of solvent through a topographically patterned membrane was shown to drive segregation of suspended nanoparticles. The drying time ranges from tens of seconds to several minutes and the resulting deposit can be sintered, constituting a potential route to single-step, roll-to-roll deposition of metallic nanostructures on flexible substrates. The Peclet number mediates the strength of evaporative convection relative to Brownian diffusion, with large values favoring particle segregation and higher features.

Analysis yields predictive expressions for deposit dimensions and drying time as a function of experimental parameters for idealized limits of $Pe = 0,1$ between which real experiments lie. Thick membranes result in higher features and thin residual layers at the cost of longer drying times. Monolayered residual layers can be ensured by employing dilute suspensions.

The analytical expressions can also be used to deduce optimal sets of experimental parameters to minimize the drying time while ensuring a certain feature and/or residual layer size. When only feature height is controlled and residual layer thickness is left unconstrained, the minimum drying time is 10 s. per 1 μm of feature height for 1 μm thick templates. When a monolayered residual layer is also desired, features up to 1 μm high can be deposited in less than 3 minutes.

The model and simulations neglect the possibility of imperfect wetting of the template and the presence of air pockets. Practical questions relating to the minimum thickness and maximum area achievable for a membrane template remain unanswered.

Polystyrene films exposed to UV radiation through a photomask possess a higher surface energy in the exposed regions relative to the unexposed due to a photo-initiated reaction. When the film is heated to above its glass transition temperature, surface tension drives convection from the unexposed to the exposed regions, resulting in the formation of topography. A theoretical model solved numerically reproduces experimental observations of topography evolution and an analytical solution based on linearization yields a rudimentary predictive ability. The dynamics of the film are driven by surface tension-induced flow, capillary stabilization and diffusive dissipation of gradients in concentration of the photo-generated species. At short times, secondary maxima and minima form adjacent to the transition between low and high surface energy regions, whereas at long times peaks and troughs coincide with the centers of these regions.

Increasing feature density (i.e. higher resolution) comes with a cost in the accessible height of the features. Thick films result in the greatest feature height above the residual layer, whereas thin ones minimize residual layer thickness. A higher surface tension differential between the exposed and unexposed regions yields higher features and thinner residual layers but does not significantly affect the heating time necessary. A 20°C increase in temperature, on the other hand, reduces heating time by over an order of magnitude while also increasing peak-to-valley height by ~ 50%. Feature formation is aided by low viscosity as well as low diffusivity of the photo-generated polymer, suggesting that a blend of a small amount of a high molecular weight photoactive polymer in a bulk low molecular weight polymer would help maximize the resolution achievable.

The theory employed utilizes lubrication theory based on the assumption that the characteristic width of the mask pattern is much larger than the thickness of the film, and is therefore expected to lose accuracy for patterns hundreds of nanometers in size.

Flow-assisted dielectrophoretic deposition exploits a precise balance of competing impulses on a nanowire; suspension flowrate and applied field strength are the most convenient ways to mediate its dynamics. Within a finite distance from the substrate, there exists a depletion layer largely void of nanowires (due to hydrodynamics, steric effects and nanowire anisotropy) and a capture zone (due to dielectrophoresis competing with hydrodynamics). Nanowires are captured when the capture width exceeds the depletion width; otherwise they are carried away with the flow. Successful assembly is aided by strong electric fields and low flowrates.

Apart from flowrate and voltage, nanowire assembly is affected by a myriad of factors, including field frequency, channel geometry, nanowire length and material properties. Scaling reveals two dimensionless groups *Di* and *DiPe* as the fundamental variables governing the assembly process, simplifying our understanding of how various experimental systems compare in terms of ease of assembly. Capture results for various flowrates and applied voltages collapse onto a single curve when plotted non-dimensionally.

With decreasing nanowire length, increasing diffusion distributes particles more broadly, thereby aiding assembly by moving some particles into the region where the electric field is strong enough for capture. However, the strength of diffusion eventually becomes prohibitive, and in conjunction with an upper limit on the applied electric field due to dielectric breakdown of solvent molecules, imposes a minimum nanowire length for which flow-assisted dielectrophoretic assembly is feasible. This is 20 nm for

nanowires with a conductivity of 2000 S/m, and varies with field frequency and particle and solvent electrical properties in accordance with the Clausius-Mossotti factor.

The model employed ignores inter-particle interactions as well as hydrodynamic interactions with the channel walls. Further, the investigation herein focuses on ensuring nanowire capture and avoiding escape with flow or diffusion; ensuring a certain *quality* of assembly (i.e. the extent of orientational misalignments or capture at undesired locations such as bus bars) may well pose more stringent requirements on experimental parameters and electrode design.

Each of the three problems suggest avenues for useful future work: experimental validation of templated evaporative lithography, relaxing the thin-film assumption to simulate higher resolutions for surface-tension driven patterning and incorporating inter-particle interactions as well as hydrodynamic interactions with the substrate into simulations of dielectrophoretic assembly of nanowires.

Appendix A: Experimental Validation of Templated Evaporative Lithography

The model and simulations detailed in Chapter 2 show that ambient evaporation can drive convection strong enough to segregate nanoparticles, making templated evaporative lithography a promising route for single-step deposition of nanopatterned films *in principle*. An experimental proof-of-concept remains to be demonstrated. Efforts were made towards this end but we were unable to fabricate a suitable template.

The process requires a topographically patterned template that promotes evaporation which is both spatially heterogeneous and fast. Heterogeneous evaporation drives transport of particles from slow to fast evaporation regions, resulting in high features and thin (or non-existent) residual layers. Fast evaporation ensures that nanoparticles segregate in spite of diffusion (which strengthens with decreasing particle size) and that the drying time is relevant to scalable, roll-to-roll patterning. Further, large area templates are preferable to maximize the area patterned in a single step..

These requirements necessitate a nanopatterned polymeric membrane (e.g. PDMS) with sub-micron thickness to ensure rapid evaporation. Fabrication of membranes becomes increasingly challenging with decreasing thickness and increasing area due to their fragility, and the need for topographical patterning only adds to the complexity of the task since the soft lithography methods commonly employed to pattern membranes are most suited to cases where membrane thickness is arbitrary.[139] These limits have been pushed the furthest by Thangawng and coworkers,[68, 69] demonstrating 492 nm thick PDMS films 491 μm in diameter with 3 μm wide lines.

Three methods were employed for the creation of PDMS templates: (i) spin-coating PDMS on a photo-lithographically patterned substrate (ii) thermal imprinting of a quartz master into a PDMS film at an elevated temperature and (iii) direct

photolithography of PDMS. In each case, separation of the patterned PDMS from the membrane resulted in breakage.

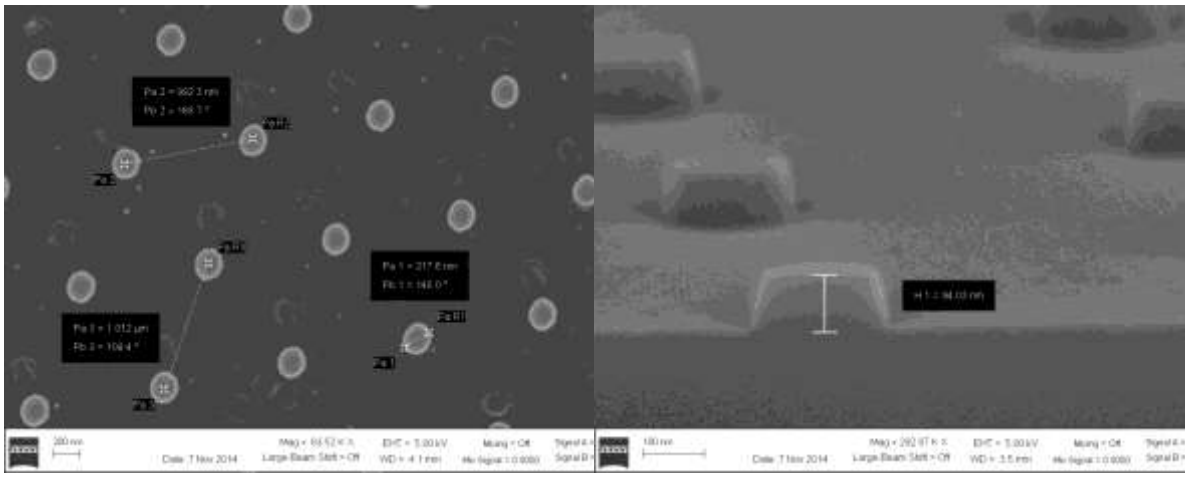

Figure A.1: SEM images of a quartz master used for thermal imprinting of a PDMS film. It consists of cylindrical pillars 218 nm in diameter, 94 nm in height and a 1 μm pitch.

A 10:1 ratio of Sylgard 184 PDMS base:curing agent was employed in each case, and SU-8 photoresist was used for (i). The substrate and master in (i) and (ii) respectively were treated with trichloro(1H,1H,2H,2H-perfluorooctyl)silane as an anti-adhesion coating.[140] For (iii), benzophenone,[141] which is sensitive to UV radiation 200 – 400 nm in wavelength, was used as the photoiniator. A 3:5 mixture of benzophenone:xylene was added to the PDMS solution to 3% by weight. A 200 – 700 nm broadband exposure was used with a dosage well above the 7.2 J/cm^2 recommended.[141]

An alternative approach was also attempted: photolithographic patterning of commercially available porous alumina membranes.[142] The membranes are rigid, 45 mm in diameter and have 50% porosity, allowing for fast evaporation; resist in the patterned areas would selectively block evaporation. However, the roughness on these is of the order of 1 micron, and resist seeps into the pores during spin-coating.

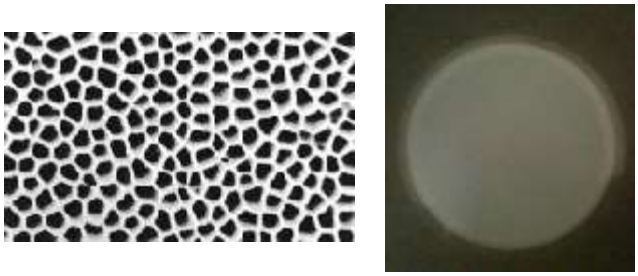

Figure A.2: A 47 mm diameter, 60 μm thick porous alumina membrane. Porosity is 50% with a 20 nm pore size.[142]

It is important to note that while these efforts demonstrate that the implementation of templated evaporative lithography is non-trivial, more work is needed to settle the question of its viability decisively. Since thick PDMS templates are relatively easily fabricated, they could be employed to demonstrate a proof-of-concept as a first step. Further, zeolites[143] are a possible template material not investigated here.

Appendix B: A Note on the Possibility of Wire Breakage During Dielectrophoretic Assembly

Dielectrophoretic assembly leverages a combination of forces and torques to assemble nanowires. Here we ascertain the extent to which these can result in breakage.

Nanowires close to the substrate undergo tumbling motion due to hydrodynamic torque. Envisaging a nanowire oriented vertically with its center at $z = 0.5l$ as a cantilevered beam with an equivalent point load that causes the same torque as hydrodynamic drag, the resulting bending can be estimated from beam theory.

$$Torque = \frac{1}{l}\int_0^l F_x^{hyd}\, z dz = \frac{1}{l}\int_0^l \bar{F}^{hyd}\frac{2z}{l} z dz = \frac{2l}{3}\bar{F}^{hyd} \tag{B.1}$$

Then the equivalent load P:

$$Pl = \frac{2l}{3}\bar{F}^{hyd} \Rightarrow P = \frac{2}{3}\bar{F}^{hyd} \tag{B.2}$$

A cylindrical wire of radius a has a moment of inertia $I = 0.25\pi a^4$, and for a modulus of elasticity E, beam theory gives

$$\theta_{deflection} = \frac{Pl^2}{2EI} \tag{B.3}$$

For silicon E = 140 GPa,[144] giving $\theta_{deflection} \sim 10^{-4^\circ}$. Further, the stress on the particle ($\bar{F}^{DEP}/\pi a^2$) is of the order 10^2 Pa, whereas the yield stress of silicon[144] is ~ 10^8 Pa. The forces and torques are therefore insufficient to cause any discernible wire deformation.

References

1. Feynman, R. P. There's plenty of room at the bottom. *Engineering and science* **1960,** *23*, 22-36.
2. Unser, S.; Bruzas, I.; He, J.; Sagle, L. Localized Surface Plasmon Resonance Biosensing: Current Challenges and Approaches. *Sensors* **2015,** *15*, 15684.
3. Anker, J. N.; Hall, W. P.; Lyandres, O.; Shah, N. C.; Zhao, J.; Van Duyne, R. P. Biosensing with plasmonic nanosensors. *Nat Mater* **2008,** *7*, 442-453.
4. Palacios, T. Applied physics: Nanowire electronics comes of age. *Nature* **2012,** *481*, 152-153.
5. De Volder, M. F. L.; Tawfick, S. H.; Baughman, R. H.; Hart, A. J. Carbon Nanotubes: Present and Future Commercial Applications. *Science* **2013,** *339*, 535-539.
6. Atwater, H. A.; Polman, A. Plasmonics for improved photovoltaic devices. *Nat Mater* **2010,** *9*, 205-213.
7. Monti, A.; Alù, A.; Toscano, A.; Bilotti, F. Optical invisibility through metasurfaces made of plasmonic nanoparticles. *Journal of Applied Physics* **2015,** *117*, 123103.
8. Im, M.; Im, H.; Lee, J.-H.; Yoon, J.-B.; Choi, Y.-K. A robust superhydrophobic and superoleophobic surface with inverse-trapezoidal microstructures on a large transparent flexible substrate. *Soft Matter* **2010,** *6*, 1401-1404.
9. Biswas, A.; Bayer, I. S.; Biris, A. S.; Wang, T.; Dervishi, E.; Faupel, F. Advances in top–down and bottom–up surface nanofabrication: Techniques, applications & future prospects. *Advances in Colloid and Interface Science* **2012,** *170*, 2-27.
10. Rajagopalan, T.; Venumadhav, K.; Arkasubhra, G.; Nripen, C.; Keshab, G.; Shubhra, G. Nanomaterial processing using self-assembly-bottom-up chemical and biological approaches. *Reports on Progress in Physics* **2013,** *76*, 066501.
11. Liddle, J. A.; Gallatin, G. M. Lithography, metrology and nanomanufacturing. *Nanoscale* **2011,** *3*, 2679-2688.
12. Mazzola, L. Commercializing nanotechnology. *Nat Biotech* **2003,** *21*, 1137-1143.
13. Hu, H.; Gopinadhan, M.; Osuji, C. O. Directed self-assembly of block copolymers: a tutorial review of strategies for enabling nanotechnology with soft matter. *Soft Matter* **2014,** *10*, 3867-3889.
14. Arshad, T. A.; Bonnecaze, R. T. Templated evaporative lithography for high throughput fabrication of nanopatterned films. *Nanoscale* **2013,** *5*, 624-633.
15. Linic, S.; Christopher, P.; Ingram, D. B. Plasmonic-metal nanostructures for efficient conversion of solar to chemical energy. *Nat. Mater.* **2011,** *10*, 911-921.
16. Schuller, J. A.; Barnard, E. S.; Cai, W.; Jun, Y. C.; White, J. S.; Brongersma, M. L. Plasmonics for extreme light concentration and manipulation. *Nat Mater* **2010,** *9*, 193-204.
17. Himpsel, F. J.; Ortega, J. E.; Mankey, G. J.; Willis, R. F. Magnetic nanostructures. *Advances in Physics* **1998,** *47*, 511-597.
18. Chou, S. Y. Patterned magnetic nanostructures and quantized magnetic disks. *Proceedings of the IEEE* **1997,** *85*, 652-671.

19. Lin, S. Y.; Chow, E.; Hietala, V.; Villeneuve, P. R.; Joannopoulos, J. D. Experimental demonstration of guiding and bending of electromagnetic waves in a photonic crystal. *Science* **1998,** *282*, 274-276.
20. Painter, O.; Lee, R. K.; Scherer, A.; Yariv, A.; O'Brien, J. D.; Dapkus, P. D.; Kim, I. Two-dimensional photonic band-gap defect mode laser. *Science* **1999,** *284*, 1819-1821.
21. Masuda, Y.; Koumura, T.; Okawa, T.; Koumoto, K. Micropatterning of Ni particles on a BaTiO3 green sheet using a self-assembled monolayer. *J Colloid Interf Sci* **2003,** *263*, 190-195.
22. Gau, H.; Herminghaus, S.; Lenz, P.; Lipowsky, R. Liquid morphologies on structured surfaces: From microchannels to microchips. *Science* **1999,** *283*, 46-49.
23. Hartl, A.; Schmich, E.; Garrido, J. A.; Hernando, J.; Catharino, S. C. R.; Walter, S.; Feulner, P.; Kromka, A.; Steinmuller, D.; Stutzmann, M. Protein-modified nanocrystalline diamond thin films for biosensor applications. *Nat Mater* **2004,** *3*, 736-742.
24. Yang, W.; Auciello, O.; Butler, J. E.; Cai, W.; Carlisle, J. A.; Gerbi, J. E.; Gruen, D. M.; Knickerbocker, T.; Lasseter, T. L.; Russell, J. N.; Smith, L. M.; Hamers, R. J. DNA-modified nanocrystalline diamond thin-films as stable, biologically active substrates. *Nat Mater* **2002,** *1*, 253-257.
25. Haynes, C. L.; Van Duyne, R. P. Nanosphere Lithography: A Versatile Nanofabrication Tool for Studies of Size-Dependent Nanoparticle Optics. *The Journal of Physical Chemistry B* **2001,** *105*, 5599-5611.
26. Yang, B.; Zhang, J. H.; Li, Y. F.; Zhang, X. M. Colloidal Self-Assembly Meets Nanofabrication: From Two-Dimensional Colloidal Crystals to Nanostructure Arrays. *Advanced Materials* **2010,** *22*, 4249-4269.
27. Dziomkina, N. V.; Vancso, G. J. Colloidal crystal assembly on topologically patterned templates. *Soft Matter* **2005,** *1*, 265-279.
28. Velev, O. D.; Kaler, E. W. In situ assembly of colloidal particles into miniaturized biosensors. *Langmuir* **1999,** *15*, 3693-3698.
29. Liu, S. T.; Zhu, T.; Hu, R. S.; Liu, Z. F. Evaporation-induced self-assembly of gold nanoparticles into a highly organized two-dimensional array. *Phys Chem Chem Phys* **2002,** *4*, 6059-6062.
30. Hayward, R. C.; Saville, D. A.; Aksay, I. A. Electrophoretic assembly of colloidal crystals with optically tunable micropatterns. *Nature* **2000,** *404*, 56-59.
31. Zhang, J. H.; Zhang, X.; Zhu, D. F.; Li, X. A.; Zhang, X. M.; Wang, T. Q.; Yang, B. A Universal Approach To Fabricate Ordered Colloidal Crystals Arrays Based on Electrostatic Self-Assembly. *Langmuir* **2010,** *26*, 17936-17942.
32. Deegan, R. D.; Bakajin, O.; Dupont, T. F.; Huber, G.; Nagel, S. R.; Witten, T. A. Contact line deposits in an evaporating drop. *Phys Rev E* **2000,** *62*, 756-765.
33. Hu, H.; Larson, R. G. Evaporation of a Sessile Droplet on a Substrate. *The Journal of Physical Chemistry B* **2002,** *106*, 1334-1344.
34. Deegan, R. D.; Bakajin, O.; Dupont, T. F.; Huber, G.; Nagel, S. R.; Witten, T. A. Capillary flow as the cause of ring stains from dried liquid drops. *Nature* **1997,** *389*, 827-829.

35. Yunker, P. J.; Still, T.; Lohr, M. A.; Yodh, A. G. Suppression of the coffee-ring effect by shape-dependent capillary interactions. *Nature* **2011,** *476*, 308-311.
36. Popov, Y. O. Evaporative deposition patterns: Spatial dimensions of the deposit. *Phys Rev E* **2005,** *71*.
37. Rabani, E.; Reichman, D. R.; Geissler, P. L.; Brus, L. E. Drying-mediated self-assembly of nanoparticles. *Nature* **2003,** *426*, 271-274.
38. Yiantsios, S. G.; Higgins, B. G. Marangoni flows during drying of colloidal films. *Phys Fluids* **2006,** *18*.
39. Routh, A. F.; Zimmerman, W. B. Distribution of particles during solvent evaporation from films. *Chem Eng Sci* **2004,** *59*, 2961-2968.
40. Routh, A. F.; Russel, W. B. Horizontal drying fronts during solvent evaporation from latex films. *Aiche J* **1998,** *44*, 2088-2098.
41. Thiele, U.; Vancea, I.; Archer, A. J.; Robbins, M. J.; Frastia, L.; Stannard, A.; Pauliac-Vaujour, E.; Martin, C. P.; Blunt, M. O.; Moriarty, P. J. Modelling approaches to the dewetting of evaporating thin films of nanoparticle suspensions. *Journal of Physics: Condensed Matter* **2009,** *21*, 264016.
42. Jarai-Szabo, F.; Astilean, S.; Neda, Z. Understanding self-assembled nanosphere patterns. *Chem Phys Lett* **2005,** *408*, 241-246.
43. Fujita, M.; Yamaguchi, Y. Simulation of 3D crystallization of colloidal nanoparticles on a substrate during drying. *Int Polym Proc* **2007,** *22*, 16-21.
44. Xu, J.; Xia, J.; Hong, S. W.; Lin, Z.; Qiu, F.; Yang, Y. Self-Assembly of Gradient Concentric Rings via Solvent Evaporation from a Capillary Bridge. *Physical Review Letters* **2006,** *96*, 066104.
45. Xu, J.; Xia, J.; Lin, Z. Evaporation-Induced Self-Assembly of Nanoparticles from a Sphere-on-Flat Geometry. *Angewandte Chemie International Edition* **2007,** *46*, 1860-1863.
46. Kim, H. S.; Lee, C. H.; Sudeep, P. K.; Emrick, T.; Crosby, A. J. Nanoparticle Stripes, Grids, and Ribbons Produced by Flow Coating. *Advanced Materials* **2010,** *22*, 4600-4604.
47. Stannard, A. Dewetting-mediated pattern formation in nanoparticle assemblies. *Journal of physics. Condensed matter : an Institute of Physics journal* **2011,** *23*, 083001.
48. Han, W.; Lin, Z. Learning from "Coffee Rings": Ordered Structures Enabled by Controlled Evaporative Self-Assembly. *Angewandte Chemie International Edition* **2012,** *51*, 1534-1546.
49. Larson, R. G. Re-shaping the coffee ring. *Angew Chem Int Ed Engl* **2012,** *51*, 2546-8.
50. Choi, S.; Jamshidi, A.; Seok, T. J.; Wu, M. C.; Zohdi, T. I.; Pisano, A. P. Fast, High-Throughput Creation of Size-Tunable Micro/Nanoparticle Clusters via Evaporative Self-Assembly in Picoliter-Scale Droplets of Particle Suspension. *Langmuir* **2012,** *28*, 3102-3111.
51. Tang, X.; O'Shea, S. J.; Vakarelski, I. U. Photoresist Templates for Wafer-Scale Defect-Free Evaporative Lithography. *Advanced Materials* **2010,** *22*, 5150-5153.

52. Georgiadis, A.; Routh, A. F.; Murray, M. W.; Keddie, J. L. Bespoke periodic topography in hard polymer films by infrared radiation-assisted evaporative lithography. *Soft Matter* **2011,** *7*, 11098-11102.
53. Han, W.; Byun, M.; Lin, Z. Assembling and positioning latex nanoparticles via controlled evaporative self-assembly. *J Mater Chem* **2011,** *21*.
54. Kumnorkaew, P.; Ee, Y. K.; Tansu, N.; Gilchrist, J. F. Investigation of the Deposition of Microsphere Monolayers for Fabrication of Microlens Arrays. *Langmuir* **2008,** *24*, 12150-12157.
55. Wang, Z. L.; Bao, R. R.; Zhang, X. J.; Ou, X. M.; Lee, C. S.; Chang, J. C.; Zhang, X. H. One-Step Self-Assembly, Alignment, and Patterning of Organic Semiconductor Nanowires by Controlled Evaporation of Confined Microfluids. *Angew Chem Int Edit* **2011,** *50*, 2811-2815.
56. Lewis, J. A.; Harris, D. J.; Conrad, J. C. Evaporative lithographic patterning of binary colloidal films. *Philos T R Soc A* **2009,** *367*, 5157-5165.
57. Lewis, J. A.; Harris, D. J. Marangoni effects on evaporative lithographic patterning of colloidal films. *Langmuir* **2008,** *24*, 3681-3685.
58. Harris, D. J.; Hu, H.; Conrad, J. C.; Lewis, J. A. Patterning colloidal films via evaporative lithography. *Physical Review Letters* **2007,** *98*.
59. Lin, Z. Q.; Hong, S. W.; Byun, M. Robust Self-Assembly of Highly Ordered Complex Structures by Controlled Evaporation of Confined Microfluids. *Angew Chem Int Edit* **2009,** *48*, 512-516.
60. Brinker, C. J.; Lu, Y. F.; Sellinger, A.; Fan, H. Y. Evaporation-induced self-assembly: Nanostructures made easy. *Advanced Materials* **1999,** *11*, 579-+.
61. Maenosono, S.; Okubo, T.; Yamaguchi, Y. Overview of Nanoparticle Array Formation by Wet Coating. *Journal of Nanoparticle Research* **2003,** *5*, 5-15.
62. Wang, L.; Ding, Y.; Lu, B.; Qiu, Z. In *Novel nano-scale overlay alignment method for room-temperature imprint lithography*, 2006; Yang, L.; Wen, S.; Chen, Y.; Kley, E.-B., Eds. SPIE: 2006; pp 61491V-6.
63. Li, N.; Wu, W.; Chou, S. Y. Sub-20-nm Alignment in Nanoimprint Lithography Using Moiré Fringe. *Nano Letters* **2006,** *6*, 2626-2629.
64. Zhang, X.; Wang, X.; Kong, W.; Yi, G.; Jia, J. Tribological behavior of micro/nano-patterned surfaces in contact with AFM colloidal probe. *Applied Surface Science* **2011,** *258*, 113-119.
65. Li, J.; Wang, M.; Shen, Y. Chemical modification on top of nanotopography to enhance surface properties of PDMS. *Surface and Coatings Technology* **2012,** *206*, 2161-2167.
66. Yim, E. K. F.; Reano, R. M.; Pang, S. W.; Yee, A. F.; Chen, C. S.; Leong, K. W. Nanopattern-induced changes in morphology and motility of smooth muscle cells. *Biomaterials* **2005,** *26*, 5405-5413.
67. Nam, H. J.; Kim, J.-H.; Jung, D.-Y.; Park, J. B.; Lee, H. S. Two-dimensional nanopatterning by PDMS relief structures of polymeric colloidal crystals. *Applied Surface Science* **2008,** *254*, 5134-5140.

68. Thangawng, A. L.; Swartz, M. A.; Glucksberg, M. R.; Ruoff, R. S. Bond–Detach Lithography: A Method for Micro/Nanolithography by Precision PDMS Patterning. *Small* **2007,** *3*, 132-138.
69. Thangawng, A. L.; Ruoff, R. S.; Swartz, M. A.; Glucksberg, M. R. An ultra-thin PDMS membrane as a bio/micro–nano interface: fabrication and characterization. *Biomed Microdevices* **2007,** *9*, 587-595.
70. Mark, J. E., *Polymer Data Handbook*. Oxford University Press: Oxford, 1999.
71. Kim, H. J.; Nah, S. S.; Min, B. R. A new technique for preparation of PDMS pervaporation membrane for VOC removal. *Advances in Environmental Research* **2002,** *6*, 255-264.
72. Peng, P.; Shi, B.; Lan, Y. Preparation of PDMS—Silica Nanocomposite Membranes with Silane Coupling for Recovering Ethanol by Pervaporation. *Separation Science and Technology* **2011,** *46*, 420-427.
73. Zhan, X.; Li, J.-d.; Huang, J.-q.; Chen, C.-x. Pervaporation properties of PDMS membranes cured with different cross-linking reagents for ethanol concentration from aqueous solutions. *Chin. J. Polym. Sci.* **2009,** *27*, 533-542.
74. Russel, W. B. S., D.A.; Schowater, W.R.;, *Colloidal Dispersions*. Cambridge University Press: Cambridge, 1989.
75. Haynes, C. L.; Van Duyne, R. P. Nanosphere lithography: A versatile nanofabrication tool for studies of size-dependent nanoparticle optics. *J Phys Chem B* **2001,** *105*, 5599-5611.
76. Xiangli, F.; Chen, Y.; Jin, W.; Xu, N. Polydimethylsiloxane (PDMS)/Ceramic Composite Membrane with High Flux for Pervaporation of Ethanol−Water Mixtures. *Industrial & Engineering Chemistry Research* **2007,** *46*, 2224-2230.
77. Wu, H.; Liu, L.; Pan, F.; Hu, C.; Jiang, Z. Pervaporative removal of benzene from aqueous solution through supramolecule calixarene filled PDMS composite membranes. *Separation and Purification Technology* **2006,** *51*, 352-358.
78. Satyanarayana, S. V.; Sharma, A.; Bhattacharya, P. K. Composite membranes for hydrophobic pervaporation: study with the toluene–water system. *Chemical Engineering Journal* **2004,** *102*, 171-184.
79. Arshad, T. A.; Kim, C. B.; Prisco, N. A.; Katzenstein, J. M.; Janes, D. W.; Bonnecaze, R. T.; Ellison, C. J. Precision Marangoni-driven patterning. *Soft Matter* **2014,** *10*, 8043-8050.
80. Dey, R.; Raj M, K.; Bhandaru, N.; Mukherjee, R.; Chakraborty, S. Tunable hydrodynamic characteristics in microchannels with biomimetic superhydrophobic (lotus leaf replica) walls. *Soft Matter* **2014,** *10*, 3451-3462.
81. Puthoff, J. B.; Holbrook, M.; Wilkinson, M. J.; Jin, K.; Pesika, N. S.; Autumn, K. Dynamic friction in natural and synthetic gecko setal arrays. *Soft Matter* **2013,** *9*, 4855-4863.
82. Schumacher, J. F.; Carman, M. L.; Estes, T. G.; Feinberg, A. W.; Wilson, L. H.; Callow, M. E.; Callow, J. A.; Finlay, J. A.; Brennan, A. B. Engineered antifouling microtopographies - effect of feature size, geometry, and roughness on settlement of zoospores of the green alga Ulva. *Biofouling* **2007,** *23*, 55-62.

83. Aubin, H.; Nichol, J. W.; Hutson, C. B.; Bae, H.; Sieminski, A. L.; Cropek, D. M.; Akhyari, P.; Khademhosseini, A. Directed 3D cell alignment and elongation in microengineered hydrogels. *Biomaterials* **2010,** *31*, 6941-6951.
84. Kim, J. B.; Kim, P.; Pegard, N. C.; Oh, S. J.; Kagan, C. R.; Fleischer, J. W.; Stone, H. A.; Loo, Y.-L. Wrinkles and deep folds as photonic structures in photovoltaics. *Nat. Photon.* **2012,** *6*, 327-332.
85. Koo, W. H.; Jeong, S. M.; Araoka, F.; Ishikawa, K.; Nishimura, S.; Toyooka, T.; Takezoe, H. Light extraction from organic light-emitting diodes enhanced by spontaneously formed buckles. *Nat. Photon.* **2010,** *4*, 222-226.
86. Scriven, L. E.; Sternling, C. V. The Marangoni Effects. *Nature* **1960,** *187*, 186-188.
87. Thomson, J. On certain curious motions observable at the surfaces of wine and other alcoholic liquors. *Lond. Edinb. Dublin Philos. Mag.* **1855,** *10*, 330-333.
88. Haas, D. E.; Birnie, D. P., III. Evaluation of thermocapillary driving forces in the development of striations during the spin coating process. *J. Mater. Sci.* **2002,** *37*, 2109-2116.
89. Burton, L. J.; Cheng, N.; Vega, C.; Andrés, J.; Bush, J. W. M. Biomimicry and the culinary arts. *Bioinspir. Biomim.* **2013,** *8*, 044003.
90. Okawa, D.; Pastine, S. J.; Zettl, A.; Fréchet, J. M. J. Surface Tension Mediated Conversion of Light to Work. *J. Am. Chem. Soc.* **2009,** *131*, 5396-5398.
91. Katzenstein, J. M.; Janes, D. W.; Cushen, J. D.; Hira, N. B.; McGuffin, D. L.; Prisco, N. A.; Ellison, C. J. Patterning by Photochemically Directing the Marangoni Effect. *ACS Macro Lett.* **2012,** *1*, 1150-1154.
92. Jensen, O. E.; Grotberg, J. B. Insoluble surfactant spreading on a thin viscous film: shock evolution and film rupture. *J. Fluid Mech.* **1992,** *240*, 259-288.
93. Gaver, D. P.; Grotberg, J. B. The dynamics of a localized surfactant on a thin film. *J. Fluid Mech.* **1990,** *213*, 127-148.
94. Janes, D. W.; Katzenstein, J. M.; Shanmuganathan, K.; Ellison, C. J. Directing convection to pattern thin polymer films. *J. Polym. Sci., Part B: Polym. Phys.* **2013,** *51*, 535-545.
95. Williams, M. L. Free Volume Approach to Polystyrene Melt Viscosity. *J. Appl. Phys.* **1958,** *29*, 1395-1398.
96. Brandrup, J.; Immergut, E. H.; Grulke, E. A.; Abe, A.; Bloch, D. R., *Polymer Handbook*. 4th ed.; John Wiley & Sons: Hoboken, 2005.
97. Bicerano, J., *Prediction of Polymer Properties*. 3rd ed.; Marcel Dekker, Inc.: New York, 2002.
98. Fleischer, G. Temperature dependence of self diffusion of polystyrene and polyethylene in the melt an interpretation in terms of the free volume theory. *Polym. Bull.* **1984,** *11*, 75-80.
99. Fleischer, G. Temperature dependence of self diffusion of polystyrene and polyethylene in the melt an interpretation in terms of the free volume theory. *Polymer Bulletin 11*, 75-80.

100. Urakawa, O.; Swallen, S. F.; Ediger, M. D.; von Meerwall, E. D. Self-Diffusion and Viscosity of Low Molecular Weight Polystyrene over a Wide Temperature Range. *Macromolecules* **2004,** *37*, 1558-1564.
101. Rouse, P. E. A Theory of the Linear Viscoelastic Properties of Dilute Solutions of Coiling Polymers. *J. Chem. Phys.* **1953,** *21*, 1272-1280.
102. Katzenstein, J. M.; Janes, D. W.; Cushen, J. D.; Hira, N. B.; McGuffin, D. L.; Prisco, N. A.; Ellison, C. J. Patterning by Photochemically Directing the Marangoni Effect. *ACS Macro Letters* **2012,** *1*, 1150-1154.
103. Wei, L.; Ping, X.; Lieber, C. M. Nanowire Transistor Performance Limits and Applications. *Electron Devices, IEEE Transactions on* **2008,** *55*, 2859-2876.
104. Haselman, M.; Hauck, S. The Future of Integrated Circuits: A Survey of Nanoelectronics. *Proceedings of the IEEE* **2010,** *98*, 11-38.
105. Yan, R.; Gargas, D.; Yang, P. Nanowire photonics. *Nat Photon* **2009,** *3*, 569-576.
106. Garnett, E. C.; Brongersma, M. L.; Cui, Y.; McGehee, M. D. Nanowire Solar Cells. *Annual Review of Materials Research* **2011,** *41*, 269-295.
107. Peng, K.-Q.; Lee, S.-T. Silicon Nanowires for Photovoltaic Solar Energy Conversion. *Advanced Materials* **2011,** *23*, 198-215.
108. Peng, K.; Jie, J.; Zhang, W.; Lee, S.-T. Silicon nanowires for rechargeable lithium-ion battery anodes. *Applied Physics Letters* **2008,** *93*, 033105.
109. Boukai, A. I.; Bunimovich, Y.; Tahir-Kheli, J.; Yu, J.-K.; Goddard Iii, W. A.; Heath, J. R. Silicon nanowires as efficient thermoelectric materials. *Nature* **2008,** *451*, 168-171.
110. Balasubramanian, K. Challenges in the use of 1D nanostructures for on-chip biosensing and diagnostics: A review. *Biosensors and Bioelectronics* **2010,** *26*, 1195-1204.
111. Long, Y.-Z.; Yu, M.; Sun, B.; Gu, C.-Z.; Fan, Z. Recent advances in large-scale assembly of semiconducting inorganic nanowires and nanofibers for electronics, sensors and photovoltaics. *Chemical Society Reviews* **2012,** *41*, 4560-4580.
112. Hobbs, R. G.; Petkov, N.; Holmes, J. D. Semiconductor Nanowire Fabrication by Bottom-Up and Top-Down Paradigms. *Chem Mater* **2012,** *24*, 1975-1991.
113. Liu, J.-W.; Liang, H.-W.; Yu, S.-H. Macroscopic-Scale Assembled Nanowire Thin Films and Their Functionalities. *Chemical Reviews* **2012,** *112*, 4770-4799.
114. Gates, B. D. Self-assembly: Nanowires find their place. *Nat Nano* **2010,** *5*, 484-485.
115. Oh, K.; Chung, J.-H.; Riley, J. J.; Liu, Y.; Liu, W. K. Fluid Flow-Assisted Dielectrophoretic Assembly of Nanowires. *Langmuir* **2007,** *23*, 11932-11940.
116. Freer, E. M.; Grachev, O.; Duan, X.; Martin, S.; Stumbo, D. P. High-yield self-limiting single-nanowire assembly with dielectrophoresis. *Nat Nano* **2010,** *5*, 525-530.
117. Castellanos, A.; Ramos, A.; González, A.; Green, N. G.; Morgan, H. Electrohydrodynamics and dielectrophoresis in microsystems: scaling laws. *Journal of Physics D: Applied Physics* **2003,** *36*, 2584.
118. Satoh, A., *Introduction to Molecular-Microsimulation for Colloidal Dispersions*. Elsevier Science: 2003.

119. Grassia, P. S.; Hinch, E. J.; Nitsche, L. C. Computer simulations of Brownian motion of complex systems. *Journal of Fluid Mechanics* **1995,** *282*, 373-403.
120. Zhang, H.; Ahmadi, G.; Fan, F.-G.; McLaughlin, J. B. Ellipsoidal particles transport and deposition in turbulent channel flows. *International Journal of Multiphase Flow* **2001,** *27*, 971-1009.
121. Raychaudhuri, S.; Dayeh, S. A.; Wang, D.; Yu, E. T. Precise Semiconductor Nanowire Placement Through Dielectrophoresis. *Nano Letters* **2009,** *9*, 2260-2266.
122. Florent, S.; Sven, S.; Maéva, C.; Samuel, G.; Liviu, N.; Guilhem, L.; Emmanuel, F.; Christophe, V. A combination of capillary and dielectrophoresis-driven assembly methods for wafer scale integration of carbon-nanotube-based nanocarpets. *Nanotechnology* **2012,** *23*, 095303.
123. Morgan, H.; Green, N. G., *AC Electrokinetics: Colloids and Nanoparticles*. Research Studies Press: 2003.
124. Jones, T. B., *Electromechanics of Particles*. Cambridge University Press: 2005.
125. Brown, D. A.; Kim, J.-H.; Lee, H.-B.; Fotouhi, G.; Lee, K.-H.; Liu, W. K.; Chung, J.-H. Electric Field Guided Assembly of One-Dimensional Nanostructures for High Performance Sensors. *Sensors (Basel, Switzerland)* **2012,** *12*, 5725-5751.
126. Rosales, C.; Lim, K. M. Numerical comparison between Maxwell stress method and equivalent multipole approach for calculation of the dielectrophoretic force in single-cell traps. *Electrophoresis* **2005,** *26*, 2057-2065.
127. Batchelor, G. K. Slender-body theory for particles of arbitrary cross-section in Stokes flow. *Journal of Fluid Mechanics* **1970,** *44*, 419-440.
128. Happel, J.; Brenner, H., *Low Reynolds number hydrodynamics: with special applications to particulate media*. Springer Netherlands: 2012.
129. Gavze, E.; Shapiro, M. Particles in a shear flow near a solid wall: Effect of nonsphericity on forces and velocities. *International Journal of Multiphase Flow* **1997,** *23*, 155-182.
130. Satoh, A., *Introduction to Practice of Molecular Simulation: Molecular Dynamics, Monte Carlo, Brownian Dynamics, Lattice Boltzmann and Dissipative Particle Dynamics*. Elsevier Science: 2010.
131. Jackson, J. D., *Classical Electrodynamics*. Wiley: 1998.
132. Liu, Y.; Chung, J.-H.; Liu, W. K.; Ruoff, R. S. Dielectrophoretic Assembly of Nanowires. *The Journal of Physical Chemistry B* **2006,** *110*, 14098-14106.
133. Park, J.; Bricker, J. M.; Butler, J. E. Cross-stream migration in dilute solutions of rigid polymers undergoing rectilinear flow near a wall. *Phys Rev E* **2007,** *76*, 040801.
134. Park, J.; Mittal, A. An Improved Model for the Steric-Entropic Effect on the Retention of Rod-like Particles in Field-Flow Fractionation: Discussion of Aspect Ratio-Based Separation. *Chromatography* **2015,** *2*, 472.
135. Park, J.; Butler, J. E. Inhomogeneous distribution of a rigid fibre undergoing rectilinear flow between parallel walls at high Péclet numbers. *Journal of Fluid Mechanics* **2009,** *630*, 267-298.
136. Toriyama, Y.; Shinohara, U. Electric Breakdown Field Intensity of Water and Aqueous Solutions. *Physical Review* **1937,** *51*, 680-680.

137. Quan, T.; Minlin, J.; Guangyong, L. Simulation and Experimental Study of Nanowire Assembly by Dielectrophoresis. *Nanotechnology, IEEE Transactions on* **2014,** *13*, 517-526.
138. Papadakis, S. J.; Hoffmann, J. A.; Deglau, D.; Chen, A.; Tyagi, P.; Gracias, D. H. Quantitative analysis of parallel nanowire array assembly by dielectrophoresis. *Nanoscale* **2011,** *3*, 1059-1065.
139. Qin, D.; Xia, Y.; Whitesides, G. M. Soft lithography for micro- and nanoscale patterning. *Nat. Protocols* **2010,** *5*, 491-502.
140. Koo, N.; Bender, M.; Plachetka, U.; Fuchs, A.; Wahlbrink, T.; Bolten, J.; Kurz, H. Improved mold fabrication for the definition of high quality nanopatterns by Soft UV-Nanoimprint lithography using diluted PDMS material. *Microelectronic Engineering* **2007,** *84*, 904-908.
141. Preetha, J.; Andrew, C.; Ali Asgar, S. B.; Gui, L.; James, E. M.; Ian, P. Photodefinable PDMS thin films for microfabrication applications. *Journal of Micromechanics and Microengineering* **2009,** *19*, 045024.
142. SPI supplies. http://www.2spi.com/item/a0247-fa/anopore_002/ (May 2, 2016),
143. Rangnekar, N.; Mittal, N.; Elyassi, B.; Caro, J.; Tsapatsis, M. Zeolite membranes - a review and comparison with MOFs. *Chemical Society Reviews* **2015,** *44*, 7128-7154.
144. Ashby, M. F.; Jones, D. R. H., *Engineering Materials 1: An Introduction to Properties, Applications and Design*. Butterworth-Heinemann: 2011.